3D Printing of Functional Anthropomorphic Phantoms Using Soft Materials for Applications in Cardiology

Wang, Shu

Awarding institution:
King's College London

3D Printing of Functional Anthropomorphic Phantoms Using Soft Materials for Applications in Cardiology

Shu Wang

First Supervisor: Prof Kawal Rhode

Second Supervisor：Prof Ronak Rajani

School of Biomedical Engineering & Imaging Sciences

Department of Surgical & Interventional Engineering

Faculty of Life Science & Medicine

King's College London

This dissertation is submitted for the degree of Doctor of Philosophy

March 2023

I dedicate this thesis to my parents, Miss Meilan Wu and Mr Weidong Wang, who offered unconditional love and support during my Ph.D. The completion of this thesis is a dream come true, but the exploration of research never ends.

DECLARATION

This dissertation is the result of my own work and includes nothing which is the outcome of work done in collaboration except where specifically indicated in the text. It has not been previously submitted, in part or whole, to any university or institution for any degree, diploma, or other qualification.

Signed: SHU WANG 王姝

Date: 13/02/2023

Shu Wang

King's College London

ABSTRACT

Three-dimensional (3D) printing has been widely used and grown rapidly through the last decades, it addresses the challenges of traditional moulding and subtractive manufacturing. In the context of cardiovascular disease (CVD), patient-specific cardiac phantoms can play an important role for interventional cardiology procedures. The emergence of 3D printing and 3D printable soft materials provide the opportunity to produce anthropomorphic phantoms with complex geometries and realistic properties for applications in cardiology. This thesis presents novel work in this field of research, focusing on the use of two soft materials: Layfomm40 and silicone. Both materials complement each other based on their strengths and weaknesses for different cardiac phantom fabrication. Several different phantoms were designed and constructed, and the functionality was demonstrated and analysed.

Chapter 1 introduces 3D printing and soft materials, as well as how 3D printing contributes to the healthcare field. Chapter 2 summarizes the state-of-art literature about 3D printed cardiac phantoms, atrial models, and various valve or aorta model manufacturing. Chapter 3 elaborates the material preparation and characterisation. The characterisation involved: 1) mechanical property testing; 2) ultrasound acoustic property testing; 3) optical microscopy; 4) thermal & electrical conductivity testing; and 5) rheological characterisation. Chapter 4 to 6 present three different cardiac models for applications in simulations. The key material used in chapters 4 & 5 was Layfomm40, while silicone was mainly utilised in chapter 6.

Chapter 4 describes the production and evaluation of a patient-specific multi-modal imaging compatible whole heart phantom using Layfomm40. The material and imaging properties of the Layfomm40 phantom were evaluated and compared to commonly used Tango Plus. The results showed that the Layfomm40 phantom had favourable tissue-mimicking material properties and was compatible with multiple imaging modalities.

Layfomm40 phantoms have great potential for cardiac interventional procedure simulation and testing of novel technologies. This work was published in the *Journal of 3D Printing & Additive Manufacturing*.

Cardiac ablation therapy is a common technique used for the treatment of arrythmias. In Chapter 5, a novel bi-atrial phantom was constructed and evaluated for simulation of atrial radiofrequency ablation (RFA). Based on the microscopy and conductivity characterisation results in chapter 3, Layfomm40 was evaluated as a suitable material for compatibility with RFA and electroanatomic mapping systems (EAMSs), which are used for guidance during cardiac RFA procedures. The irreversible thermochromic paint was also investigated to allow visualisation of ablation points. The printed Layfomm40 atrial model was coated with this thermochromic paint, placed in a custom enclosure and evaluated for simulation of cardiac ablation procedures in the cardiac catheterisation laboratory using fluoroscopy and the CARTO3 EAMS. The thermochromic paint allowed realistic visualisation of the ablated areas and the bi-atrial phantom performed well as an interventional procedure simulator. This work was published in *Applied Sciences: Emerging Techniques in Imaging, Modelling and Visualization for Cardiovascular Diagnosis and Therapy.*

Aortic stenosis is one of the most common cardiac pathologies and there are many open questions regarding its optimal management. There is an emerging demand for aorta and valve phantoms to study aortic stenosis. Although Layfomm40 has been proved to be suitable for creating static cardiac phantoms, it is prone to delamination and therefore it would be challenging to construct dynamic phantoms that can withstand physiological flow conditions or have functional components, such as valves. However, silicone is a resilient soft tissue-mimicking material used commonly to make anthropomorphic phantoms. In Chapter 6, silicone aorta and aortic valve phantoms were constructed and evaluated. Initially, 3D-printed two-part moulds were used to make the phantoms, with the internal mould printed in water-soluble material. Different

diseased valves were manufactured with Ecoflex silicone and then attached to a durable aorta model fabricated using Dragonskin silicone. The phantoms were evaluated using a physiological flow circuit and imaged using ultrasound and magnetic resonance imaging (MRI), showing realistic anatomical appearance and physiologically plausible function. Then, for comparison, another aortic valve model was fabricated using direct silicone printing with modified silicone inks. The printed silicone valve also survived in the flow test, demonstrating an alternative and viable new solution for silicone model manufacturing. The valve manufacturing work using the two-part mould technique was published in the *MICCAI-STACOM Conference*, and the physiological pressure analysis of the silicone valves was accepted in the *Journal of Cardiovascular Translational Research*.

In conclusion, the work presented in this thesis expands the knowledge and understanding in the domain of using soft materials for construction of cardiac anthropomorphic phantoms. This will have a significant impact for the training of healthcare professionals, testing of novel devices and imaging technologies, and the progression of research for the treatment of CVD.

ACKNOWLEDGEMENTS

I am overwhelmed in all humbleness and gratefulness to acknowledge my debt to all those who have helped me during my PhD to put these ideas well above the level of simplicity and into something concrete. I would like to express special thanks and gratitude to my principal supervisor, Prof Kawal Rhode, who offered me the golden opportunity to complete this wonderful project on the topic of 3D printing and soft materials, and organised collaborations with clinicians to help 3D printing contribute to real healthcare. I would like to also thank my second supervisor, Prof Ronak Rajani, who helped me in collecting ultrasound data and interventional skills, as well as the guidance in thesis organisation and paper writing.

Besides, I would like to thank all the colleagues and friends who gave me different ideas in making my PhD project unique, especially Dr Richard Housden, Dr Shuangyi Wang, Dr Yohan Noh, Dr Xianqiang Bao, Dr Harminder Gill, and many others. Despite their busy schedules, they offered selfless help in my experiments, thesis and even daily life. All the members from my Thesis Progression Committee, including Dr Pablo Lamata, Dr Martin Bishop and Dr Steven Williams are very well appreciated for their valuable advice for my research.

I also gratefully acknowledge the scholarship received for my PhD study from the KCL-CSC scheme and the funding for the project from the National Institute for Health Research (NIHR) Biomedical Research Centre at Guy's and St. Thomas' NHS Foundation Trust and King's College London.

Finally, I would like to thank my parents. Any attempt at any level can’t be satisfactorily completed without their continuous support and understanding when undertaking my research. Their prayers for me were what sustained me this far.

Covid Impact Statement

The impact of the coronavirus disease 2019 (COVID-19) pandemic on all aspects of our lives is well known. The outbreak of COVID-19 has created a global health crisis that has had a deep impact on the way we perceive our world and our everyday lives.

My lab in St Thomas' Hospital was closed from March to May 2020 due to Covid-19, when typically, I would have been running experiments. During lockdown, I could only work remotely on my thesis while the manufacturing of the ablation simulator and development of silicone printer had to be postponed for nearly six months. Meanwhile, out of the consideration of health and safety, I had to come back to China for the PhD thesis writing-up. The remote working delayed my progress, especially when I got infected. Thus, the thesis submission date was deferred as well as the final online viva. The chapters affected the most were the chapter about radiofrequency ablation (RFA) simulator and the chapter about valve manufacturing using silicone printing. The impact will be described in detail at the beginning of related chapters.

CONTENTS

LIST OF FIGURES

LIST OF TABLES

1. INTRODUCTION & BACKGROUND

1.1 Thesis Motivation, Aims, Objectives and Structure

1.1.1 Thesis Motivation & Aims

Three-dimensional (3D) printing has been widely used and grown rapidly through the last decades, it addresses the challenges of traditional moulding and subtractive manufacturing [1]. In the context of cardiovascular disease (CVD) [2], patient-specific cardiac phantoms can play an important role for interventional cardiology procedures [3]. The emergence of 3D printing with soft materials provides the opportunity to produce anthropomorphic phantoms with complex geometries and realistic properties for applications in cardiology. However, the materials used in previous research either have inappropriate properties for medical imaging or are not suitable for 3D printing, while most 3D printable soft materials available in the market like thermoplastic polyurethane (TPU) [4] or elastic resin [5] are not flexible/ultrasound compatible enough to mimic cardiac tissue, let alone their functional limitations in certain interventional procedures. Some patient-specific phantoms [6,7] are known to be useful in clinical applications, but they are either difficult to manufacture or incomplete without fine geometries, which limits their applications in high-fidelity scenarios.

Motivated by solving the problem of making anatomically realistic cardiac phantoms which can be applied in various interventional simulations, and deepening the investigation of more 3D printable soft material choices, this thesis presents novel work in this field of research.

The aim of the PhD work begins with the need to seek a solution for the production of

a complete, ultrasound compatible cardiac phantom for multimodal medical imaging and interventional procedures, using the techniques of 3D printing. The phantom needs to be easy to manufacture and at the same time, customisable and inexpensive. When a phantom is to be imaged, it is necessary to use a material with appropriate properties for the imaging modality. Ultrasound imaging, in particular, requires good soft tissue-mimicking properties, such as low acoustic attenuation and low surface reflection [8]. Material's flexibility should, therefore, be a key factor when choosing a material for an ultrasound phantom. Then, the aims were expanded to make other types of cardiac models for specific uses in electrophysiological and dynamic experiments. Other than being compatible to different medical imaging modalities, they have to demonstrate corresponding properties such as thermochromism [9], conductivity [10], durability [11], etc. Functions should be validated using multiple clinical systems, while comparisons should be made between the used materials and biological tissue.

1.1.2 Thesis Objectives

The overall thesis mainly uses two soft materials—Layfomm40 from Poro-Lay series (Kai Parthy, Germany) & silicone elastomer from Smooth-on silicone (Smooth-on Inc, the USA). Table 1.1 lists the key materials and corresponding characterisations before using them to make specific cardiac phantoms:

Table 1.1. Characterisations of key materials used in the thesis.

Key Materials	Charaterisations
3D printable materials: Layfomm40, modified silicone inks; Unprintable materials: Commercial RTV-silicones	1. Mechanical tests; 2. Ultrasound acoustic property tests; 3. Optical microscope observations; 4. Conductivity tests; 5. Rheological tests.

While Layfomm40 is a novel 3D printable material, silicone needs to be modified for the use in direct silicone printing [12], otherwise the moulding technique [13] should be applied instead. Before using them to manufacture functional anthropomorphic phantoms for applications in cardiology, the two materials were characterised from the following aspects listed in table 1.1, with some comparisons to the other 3D printable soft materials such as Tango Plus [14]. Major findings could be summarized from the material characterizations:

From mechanical tests, as a 3D printable material, Layfomm40 has the closest Young's modulus [15] value (128.5 kPa) to real myocardium (180-280 kPa [16]) with a difference of 28.6%–54% when compared to other 3D printable materials in Poro-Lay series & Tango Plus. While Dragonskin 10 silicone has a close Shore A hardness [15] value (9.5 HA) to arcus aorta's (13.4±1.9 HA [17]) with a difference of 29.10%, and Ecoflex 0030 has a Young's modulus value of 55 kPa, with a minor difference of 11.29% when compared to the value of real valvular leaflets' tissue (62 kPa [18]).

From ultrasound acoustic property tests, excluding the unprintable silicone materials, among the 3D printable soft materials compared in terms of ultrasound acoustic properties [19], all the Poro-Lay series materials after rinsing have significantly less difference to myocardium [19] than Tango Plus, for example, Gel-Lay has the smallest impedance difference of 2.99% and Layfomm40 has the smallest velocity difference of 32 m/s, while Tango Plus's impedance difference to tissue is 34.13% and 809 m/s respectively. However, the ultrasound properties' difference between the materials within Poro-Lay series are quite small, which means the Poro-Lay materials are good ultrasound materials.

While from the optical microscope [20] observations, the images from microscale of rinsed Layfomm40 are consistent with its formula description: micro holes could be generated in its polymer structures and water/saline/thermochromic solutions could be

absorbed inside with the dissolving of its PVA component.

The electrical conductivity tests prove that small electrical conductivity (3.0×10^{-6} S/m) could be obtained in saline water rinsed Layfomm40, which is higher than the value of silicone rubber (5.16×10^{-12} S/m [21]), this property makes Layfomm40 compatible to the radiofrequency ablation (RFA) and electroanatomic mapping systems (EAMS) [22] in functional testing described in chapter 5. Meanwhile, the thermal conductivity of rinsed Layfomm40 is 0.4 W/m/K, which is comparable to the value of cardiac tissue (0.56 W/m/K [23]), with a minor difference of 28.57%. And the rheological [24] tests show both high temperature and suitable amount of fumed silica are necessary to make the silicone ink printable, as high temperature could accelerate its curing process while fumed silica addition could increase its viscosity.

Based on these characteristics of Layfomm40 and silicone, they were then chosen to make different cardiac models: ultrasound compatible whole cardiac model for multi-modal medical imaging in chapter 4, thermochromic bi-atrial model for ablation simulation and CARTO3 mapping [25] in chapter 5, durable aorta and valve models with different pathologies for pressure analysis under ultrasound/MRI imaging in chapter 6. Corresponding functional experiments and success metrics are summarized in table 1.2-1, 1.2-2 & 1.2-3.

Table 1.2-1. Developed whole cardiac models and success metrics (Chapter 4)

Manufacturing Techniques	Objectives	Experiments	Success metrics
3D printing (FDM)	Ultrasound compatible whole cardiac models (Layfomm40 & Tango Plus)	1. Visual inspection 2. Ultrasound imaging 3. X-ray & CT imaging 4. MRI imaging	1. Anatomical similarity to patient heart; 2. Clear ultrasound, X-ray, CT & MRI images collected on both phantoms

Table 1.2-2. Developed thermochromic bi-atrial model and success metrics (Chapter 5)

Manufacturing Techniques	Objectives	Experiments	Success metrics
3D printing (FDM)	Thermochromic bi-atrial model (Layfomm 40)	1. Visual inspection 2. RF ablation 3. CARTO3 mapping 4. Ultrasound	1. Anatomical similarity to patient atrium; 2. Permanent and reproducible marks after ablation; 3. Successful CARTO3 mapping results; 4. Clear ultrasound image from bicaval view

Table 1.2-3. Developed aorta & valve models and success metrics (Chapter 6)

Manufacturing Techniques	Objectives	Experiments	Success metrics
Two-part moulding (Moulds printed using FDM printer separately)	Aorta model One normal valve & three pathological valve models	Ultrasound imaging 1.Visual inspection 2. Ultrasound & MRI-Imaging 3. Flow test	Ultrasound compatibility 1. Anatomical similarity to biological valves; 2. Ultrasound & MRI-Compatibility; 3. Durability; 4. Close transvalvular pressure gradient to natural & commercial prosthetic valves
Silicone printing	3D printed normal valve	Ultrasound imaging& flow test	Similarity to moulded valve

1.1.3 Thesis Structures

The whole thesis includes 7 chapters, with main contents are chapter 3 ~ 6:

Chapter 1 introduces the overall contents of the thesis and gives the introduction to 3D printing technologies and soft materials, and chapter 2 summarizes the state-of-art literatures about various 3D printed cardiac phantoms, including whole cardiac models, bi-atrial models and valve models, which correspond to the work presented in the following “results” chapters from chapter 4 to chapter 6. During the finding and using of new 3D printable soft materials, the soft material candidates were chosen based on their characterisation results, the relevant material preparation and characterisation are illustrated in chapter 3.

Chapter 4 describes the production and evaluation of a patient-specific multi-modal imaging compatible whole heart phantom using a novel 3D-printable material called Layfomm40. The material and imaging properties of the Layfomm40 phantom were evaluated and compared to commonly used Tango Plus phantoms. The results showed that the Layfomm40 phantom had favourable tissue-mimicking material properties and was compatible with multiple imaging modalities. Layfomm40 phantoms have great potential for cardiac interventional procedure simulation and testing of novel technologies. This work was published in the following journal paper*:* Wang, S., Noh, Y., Brown, J., Roujol, S., Li, Y., Wang, S., Housden, R., Ester, M. C., Al-Hamadani, M., Rajani, R., & Rhode, K. (2020, December). Development and testing of an ultrasound-compatible cardiac phantom for interventional procedure simulation using direct three-dimensional printing. *3D Printing and Additive Manufacturing*, 269–278. https://doi.org/10.1089/3dp.2019.0097

Cardiac ablation therapy is a common technique used for the treatment of arrythmias. In chapter 5, a novel phantom was constructed and evaluated for simulation of atrial

radiofrequency ablation. Layfomm40 was evaluated as a suitable material for compatibility with RFA and EAMS, which are used for guidance during cardiac RFA procedures. An irreversible thermochromic paint was investigated to allow visualisation of ablation lesions. A Layfomm40 atrial model was constructed and coated with the thermochromic paint. This was placed in a custom enclosure and evaluated for simulation of cardiac ablation procedures in the cardiac catheterisation laboratory using fluoroscopy and CARTO3 mapping. It was found that Layfomm40 was compatible with RFA and CARTO3 mapping system. The thermochromic paint allowed realistic visualisation of ablation lesions and the atrial phantom performed well as a procedure simulator. This work is published in this journal paper:
Wang S, Saija C, Choo J, Ou Z, Birsoan M, Germanos S, Rothwell J, Vakili B, Kotadia I, Xu Z, Rolet A, Namour A, Yang WS, Williams SE, Rhode K. (2022, June). Cardiac radiofrequency ablation simulation using a 3D-printed bi-atrial thermochromic model. *Applied Sciences*. https://doi.org/10.3390/app12136553

Although Layfomm40 proved to be suitable for creating cardiac phantoms, it is prone to delamination and therefore it would be challenging to construct phantoms that can withstand physiological flow conditions or have functional components, such as valves. In chapter 6, silicone phantoms of the aorta and aortic valve were constructed and evaluated. 3D printed two-part moulds were used to make the silicone phantoms, with the internal mould printed in water-soluble material. Different diseased valves were manufactured with Ecoflex 0030 silicone and then attached to a durable aorta model which was fabricated using Dragonskin silicone. The phantoms were evaluated using a physiological flow circuit and imaged using ultrasound and magnetic resonance imaging (MRI), showing realistic anatomical appearance and physiologically plausible function. Additionally, in Chapter 6, the possibility of directly 3D printing phantoms using silicone is explored. The silicone material properties were modified using fumed silica to increase compatibility with the silicone printer. Another aortic valve model was designed and constructed using silicone printing and evaluated using a

physiological flow circuit and ultrasound imaging. Results demonstrated that the directly printed valve was comparable to that made by two-part moulding. Relevant work about the two-part moulding manufacturing technique was published in the *MICCAI-STACOM Conference*: Wang, S., Gill, H., Wan, W., Tricker, H., Fernandes, J. F., Noh, Y., ... & Rhode, K. (2019, October). Manufacturing of ultrasound-and MRI-compatible aortic valves using 3D printing for analysis and simulation. *In International Workshop on Statistical Atlases and Computational Models of the Heart* (pp. 12-21). Springer, Cham. While the haemodynamic findings were presented in the publication of our collaborator: Gill, H., Fernandes, J. F., Nio, A., Dockerill, C., Shah, N., Ahmed, N., Raymond, J., Wang, S., Sotelo, J., Urbina, J., Uribe, S., Rajani, R., Rhode, K., & Lamata, P. (2023). Aortic Stenosis: Haemodynamic Benchmark and Metric Reliability Study. *Journal of Cardiovascular Translational Research*. https://doi.org/10.1007/s12265-022-10350-w

Chapter 7 presents the summary of the finding, conclusions, and some directions for future work. The work presented in this thesis expands the knowledge and understanding in the domain of using soft materials for construction of cardiac anthropomorphic phantoms. This will have a significant impact for the training of healthcare professionals, testing of novel devices and imaging technologies, and the progression of research for the treatment of CVD.

1.2 Types of 3D Printing Techniques and Printable Materials

3D printing/additive manufacturing is an additive process to turn a digital file into a 3D solid model. It is the opposite to a subtractive method that involves material removal. Instead, it creates the object layer by layer with the use of a 3D printer [26]. Today, this technology has spread into the fields of the military industry, education, architecture, automotive engineering, civil engineering, healthcare, and many others [26]. Based on

the printing procedure, it can be classified into the following types: fused deposition modelling (FDM), vat polymerisation like digital light processing (DLP) and stereolithography (SLA), selective laser sintering (SLS), inkjet printing, extrusion-based printing, and many others.

The general principles of 3D printing involve 3D modelling, material and printer type selection, printing and finishing, which are illustrated in figure 1.1. The 3D models can be generated via computer-aided design (CAD), 3D scanning, 2D photography with 3D reconstruction using photogrammetry software, 3D animation software or medical segmentation software. After fixing any errors in the 3D files, they can be processed by slicing software that converts the model into printing paths called g-code. With the resultant g-code, the printer can construct the model layer by layer. The printing procedure can last from several minutes to days. Because the layered structure will cause inevitable staircasing effects on the surface of prints, a chemical vapour process using alcohol and other solvents can be used to polish the printing results and achieve a smoother surface.

Figure 1.1 General principles of 3D printing

3D printing/Additive manufacturing is a term encompasses various materials. The material choices include synthetic plastics, resins, metals, rubbers with different flexibility, surface finishing, durability, printing speed, melting temperature and cost [27]. Selecting the correct materials and 3D printing techniques based on the application needs is the first step of product development as different technologies have their own strengths and weaknesses.

Figure 1.2 [28] demonstrates the main mechanism of four main streams 3D printing techniques, even though they all build models layer by layer, they still have significant differences in terms of raw material forms, curing and extrusion processes.

FDM, also named fused filament fabrication or filament freeform fabrication (FFF) [29], is the most used 3D printing technique with the use of continuous thermoplastic filament. FDM printer uses a heated extrusion nozzle to melt the polymer in a filament form and the material will then be cured on the print bed, meanwhile, the motor drives the spool to feed the new filament inside the extruder. The speed of a FDM printer can reach 90mm/s which surpass other printer types. Figure 1.2 (a) shows the mechanism of a typical dual extruder FDM printer, which can print two different materials at the same time.

Inkjet-based 3D printing is also known as binder jet printing or drop-on-demand (DOD) printing. It is a type of additive manufacturing technology to recreate colourful models with high fidelity and printing resolution [30]. As shown in figure 1.2 (b), inkjet printing uses similar print head to move across a bed of liquid materials/solid suspensions of photopolymers and selectively depositing liquid binding materials. Unlike FDM, it is a low-temperature and low-pressure process. When the model is completed, unbound materials will be automatically removed and reused for next time [30].

SLA, also known as resin printing, is a 3D printing technique that uses UV-light curable resin materials to create prototypes. The printable resin is usually made of monomers and a photo initiator, which can be crosslinked from a liquid form to a solid model under light with certain wavelengths [31]. In figure 1.2 (c), SLA uses a laser source with a scanning system instead of a print head to cure liquid photopolymer on the fabrication platform. The whole process will be carried out inside a light-proof environment. Compared to other technologies, it can achieve the highest resolution of $10\mu m$ with the sharpest details, while the printed parts are relatively brittle [32].

SLS is a 3D printing technique using laser source to sinter or melt powdered materials like metal and nylon. The laser can bind the material together to make the solid 3D model [33]. This technique is commonly used to manufacture metal parts. As shown in figure 1.2 (d), SLS uses a laser and scanning system, unused powder can be recycled, and printed parts should be further post-processed by media blasting for better quality.

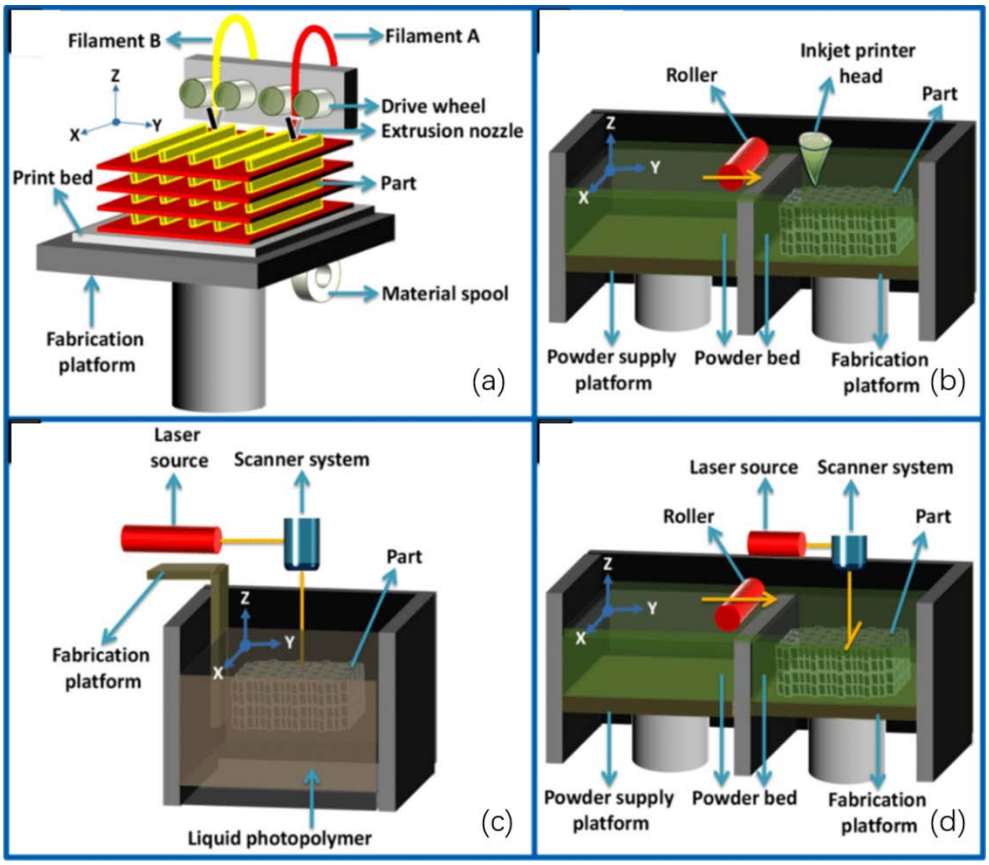

Figure 1.2. Main mechanisms of key 3D printing techniques: (a) fused deposition modelling (FDM), used materials: thermoplastic filaments; (b) inkjet printing, used materials: liquid materials/solid suspensions of photopolymers; (c) stereolithography (SLA), used materials: photo crosslinked resins; and (d) selective laser sintering (SLS), used materials: metal/plastic powder [28]

1.3 Introduction to Soft Materials and Relevant Uses in 3D Printing

In terms of materials' level of flexibility, they can be classified as soft materials or rigid materials. The definition of soft material in this thesis refers to materials with the following features: (a) can be bent, twisted and deformed without losing properties, and (b) are easy to fracture, stretch, deform and burn during processing [34]. These properties bring about difficulties in manufacturing using soft materials, as well as motivate the development of related tools, equipment and technologies. Advanced manufacturing with soft materials has been investigated for 60 years [35], and 3D printing was regarded as one of the cutting-edge technologies in manufacturing using soft materials [36].

TPU is a well-known 3D printable material used to make flexible parts with both plastic and rubber properties [37]. It belongs to the thermoplastic elastomers (TPE) family and can be stretched, compressed or bent without being easily broken under external force. However, this flexibility makes it more challenging for direct printing compared to normal PLA or ABS materials. Additionally, its thermal stability and chemical resistance make this material more difficult to be post-processed than other TPE materials. Currently, TPU rubbers are widely used in sports goods, automotive bushings and protective products as shown in figure 1.3 (a) [37], with a range of Shore A hardness between 40-90 HA, and elongation break between 130-300%.

Two other noted commercial soft material series in the 3D printing market are produced by one of the leading companies, Stratasys, using the PolyJet technique. One series is the Tango series, including Tango and Tango Plus; the other is the digital anatomy series, including tissue-matrix and gel-matrix. Compared to the previously mentioned TPU composites, Tango materials can build up flexible prototypes and simulate rubber-

like properties with a much lower Shore A hardness of 26-28 HA and elongation break of 170-220 %. These are ideal for making shock absorption footwear, gaskets and surgical models as shown in figure 1.3 (b) [38]. While the other one--tissue-matrix is the softest commercially available printable material which behaves very closely to real human tissue. When mixing it with different amounts of another PolyJet material, Agilus, tissue-matrix can be extended to simulate fat, muscle and tumours, and used to make more types of tissues that mimic soft organs, for example, the full cardiac model shown in figure 1.3 (c) [39], but this new series has not been widely used due to the high cost.

Ultraviolet (UV) light-curable soft materials are also being rapidly developed to work with SLA printers. Some elastic resin materials can achieve a minimum Shore A hardness of 38 HA, for example, the Flex100 resin demonstrated in figure 1.3 (d) (Monocure, Australia) [40]. In combination with shape memory polymers, a new type of photosensitive 4D hydrogel has been invented, as shown in figure 1.3 (e) [41]. The printed lotus can gradually blossom under UV light with a 365-405nm wavelength, and it has great potential in healthcare applications, such as self-expanding cardiac stents.

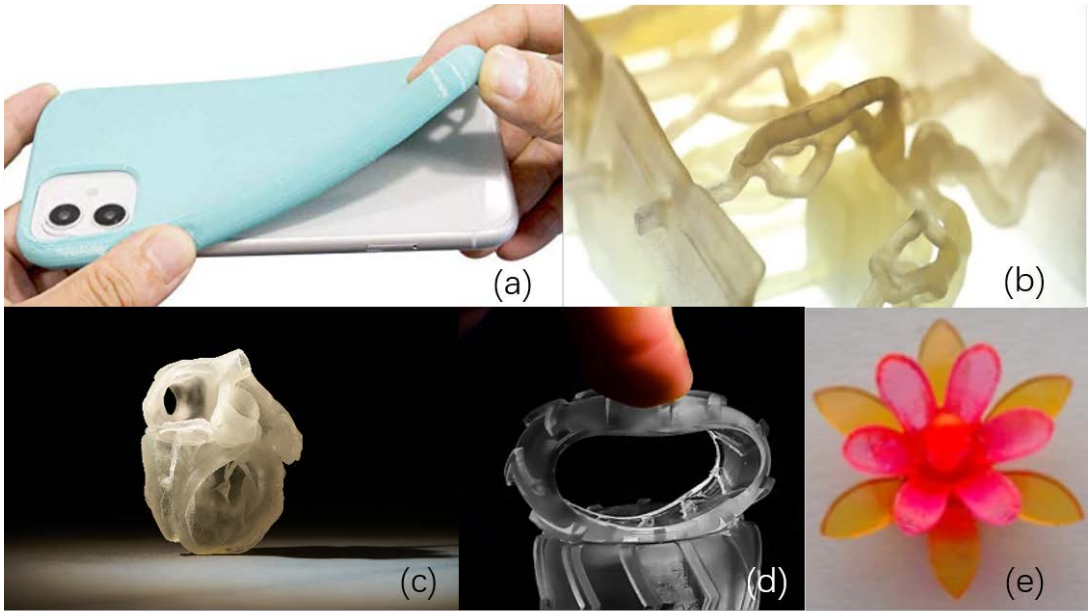

Figure 1.3. Soft material products made by additive manufacturing platforms (a) TPU cell phone cover [37]; (b) Tango Plus vascular model [38]; (c) tissue matrix cardiac

model [39]; (d) elastic resin tire model [40]; (e) 4D hydrogel lotus model with self-expanding effects [41]

However, the primary limitation of current 3D printing with soft materials is the low manufacturing speed, as it is more difficult to push the right amount of extrusion through the nozzle, rapid movement of the extruder can cause uneven surface finishing, and most soft materials take more time to cure on the printer bed [42]. The second limitation is that the current printable models developed with rigid materials are not suitable for soft and active materials, as some sophisticated designs need strong supports which soft materials cannot provide. The third limitation is the 3D printable soft material choices and their hardness, so far, the most known elastic commercial FDM-printable filament has a hardness of 60 HA [43], while the most elastic UV-curable resin has a hardness of 50 HA [44], and Tango series from Stratasys has a hardness of 26 HA [38].

The soft materials explored in this thesis, for example, Layfomm40 from the Poro-Lay series and modified silicone inks, expand the variety of 3D printable soft materials with detailed analysis of their strengths and disadvantages. The potential combination with other material components such as smart materials and the improvement of the techniques' accuracy and functions provide the opportunity to fabricate more functional phantoms, devices and systems.

1.4 3D Printing in Healthcare

The development of 3D printing and its products help advance several fields, including the automotive, education, military and even fashion industries. This section will focus on the state-of-the-art applications in healthcare, which have gone through several levels. At the first level, the printed products are mainly medical models and devices used in vitro, which have no requirements for material biocompatibility and special

mechanical properties. Secondly, the materials used have good biocompatibility, but the product cannot be degraded and will become a permanent implant after being placed inside the human body. Thirdly, the materials used have good biocompatibility and degradability. After implantation, the product can interact with human tissues to promote tissue regeneration. At the final level, the used materials contain living cells, proteins and other extracellular matrices with biological activities to make real tissues and organs. Currently, the first three application levels are relatively mature and have entered into real clinical scenarios. The following sub-sections will illustrate some classic applications from different levels.

The rise of 3D printing has started to contribute to surgical departments, from visual-tactile aids in preoperative planning to patient-specific implants. The relevant applications focus on the following categories: surgical models/phantoms, simulation guides/platforms and implants. Though the models and guides can easily be printed using plastics or resins with FDM or SLA techniques, the implants are generally printed with metal or high-performance materials with SLS, SLM or inkjet printing because they require good biocompatibility and strength. Phantoms and simulators can be used to improve the surgical outcome prediction, and the real surgery operation time and risks can both be reduced. 3D printed models have already been demonstrated as superior to 3D medical images [45].

Patient-specific implants are another recent and popular 3D printing application. The implants are segmented from accurate 3D medical imaging slices to best fit the patient anatomy and restore the proper function. For example, surgery for bone reconstruction caused by tumour and neurosurgery for skull defect reconstruction also utilise patient-specific implants [46,47], as does chest wall reconstruction in thoracic surgery.

Tissue engineering is an interdisciplinary subject with a combination of cell culture, material and biomedical engineering that focuses on biological tissue restoration, maintenance, improvement and replacement [48]. 3D bioprinting is a promising technique to fabricate tissues and organs using hydrogels loaded with living cells. It can

be realised via inkjet, extrusion-based and laser-assisted printing and has the potential to produce different transplantable soft tissues like skin and cartilage [49]. It is a useful tool for creating biomimetic scaffolds with well-controlled chemistry and architecture using thin material layers that other manufacturing methods cannot achieve. Various biomaterials can be used in 3D bioprinting to form the desired organ shapes with different mechanical properties. Polymeric materials are preferred because of the good biocompatibility, biodegradability, low cost, and preparation as bio-inks. For example, hydrogel is the most commonly used bio-ink type because cells can live inside this material. They can be obtained naturally or by manual synthesis [49]. With microscopic pores left within the structure, these pores provide the essential nutrients for stem cells.

2 LITERATURE REVIEW

The following subsections summarise the state-of-art literatures about various cardiac model fabrications, which correspond to the content described in each “results” chapter:

2.1 State-of-art 3D Cardiac Phantoms Used in Clinical Applications

The literature review in section 2.1 corresponds to the content in chapter 4: the development of ultrasound compatible whole cardiac models, and their uses in cardiac interventional procedures/multimodal medical imaging.

2.1.1 Clinical background of cardiac interventional procedures and multimodal imaging techniques

A cardiac interventional procedure, also known as an interventional cardiology procedure, is an important type of minimally invasive surgery that deals with the catheter-based treatment of cardiovascular diseases, such as coronary artery disease, arrythmias, peripheral arterial diseases and aortic diseases [50]. The main advantages of using the interventional cardiology approach are the avoidance of scars, pain and long post-operative recovery compared with traditional open-heart surgery.

Generally, cardiac interventions can be classified into seven categories: cardiac catheterisation, percutaneous coronary intervention, stents, embolic protection, percutaneous valve repair, balloon valvuloplasty and atherectomy. Catheters are medical devices that can be inserted in the body to perform several cardiac intervention procedures. As an example of these procedures, a right heart catheterisation for tissue ablation to treat atrial fibrillation is shown in figure 2.1 [51]. The catheter will be

inserted into the groin and threaded through the femoral vein and inferior vena cava to the right atrium, then reaches the left atrium through transseptal puncture using a kit including a pre-shaped sheath, an introducer and a needle.

Figure 2.1. Cardiac catheterisation for tissue ablation under X-ray imaging guidance [51]

A catheter-based interventional procedures can be performed under multiple imaging modalities for guidance, particularly where the anatomy is complex or soft tissue visualisation is crucial. Since direct line of sight is inhibited, the imaging provides the position of intervention instruments in respect to the patient´s anatomy. These imaging modalities include real-time cardiac magnetic resonance (CMR)[52], radiology[53], echocardiography/cardiac ultrasound [54], etc. Each modality has its advantages and disadvantages, so two or more modalities are sometimes combined to monitor cardiac catheterisation.

Cardiovascular magnetic resonance imaging (CMR) can provide high-resolution, real-time 3D cardiac information without ionising radiation; however, it is not commonly used for cardiac interventions, but for diagnosis. It demonstrates excellent tissue-device contrast and dynamic cardiac function, especially the enhancement of the chamber/vessel wall and lumen [52].

Interventional radiology was invented as an efficient, invasive diagnostic imaging specialty [53] and encompasses a wide range of rooms, such as catheterisation laboratories and angiography and electrophysiology suites. The fluoroscopy-guided interventional procedure can be regarded as the gold standard of cardiovascular disease diagnosis and treatment since X-Ray have high temporal and spatial resolution. Additionally, interventional cardiologists also embrace cardiac CT (CCT) as a helpful tool during minimally invasive surgery to improve tissue discrimination. It is now often used in pre- and post- evaluation for coronary intervention [55]. and in the future, non-invasive coronary CT angiography (CTA) could be widely used instead of invasive diagnosis [56]. However, the use of CT scanning is a major healthcare advancement, especially when analysing coronary anatomical details, and sometimes supplants traditional invasive angiography, but the lower frame rate, compared with X-Ray imaging, limits its real-time functionality. Therefore, CT scanning is used mainly as an evaluation procedure, while X-Rays are used mainly for real-time device guidance in cardiac interventions [57].

Even though traditional X-Ray imaging dominates percutaneous cardiovascular interventions, it is limited when interventions involve the myocardium, pericardium and cardiac valves, because it has very limited soft tissue contrast. Cardiac ultrasound (echocardiography) can overcome these problems. Compared to the other imaging modalities, echocardiography [54] is especially useful for transcatheter treatments, percutaneous mitral valve procedures and left atrial appendage closures, because it simultaneously provides real-time imaging of the device and the cardiac inner structures. There are three types of echocardiography that might be used during intervention: transthoracic echocardiography (TTE), intracardiac echocardiography (ICE) and transoesophageal echocardiography (TOE/TEE). TTE is widely available and portable as a non-invasive imaging procedure [54,] although it has a limited ability to visualise the back of the heart and is difficult to use during interventional procedures

since the ultrasound probe needs to be held manually for a long time. ICE has also demonstrated great potential for device monitoring during interventions, with a probe insertion that is comfortable for the patient, but several limitations currently exist: the phased array probe is expensive and single use only, and no standard views for ICE have been defined [58]. As a trade-off between image quality and imaging cost, TOE imaging is commonly chosen before and during catheter-based interventions.

2.1.2 Ultrasound compatible materials and phantom fabrication

Tissue-mimicking materials [59] with ultrasound compatibility have been widely used in anatomical model fabrication and related biomedical research. They have played an important role in modelling soft tissue to evaluate clinical procedures with multimodal imaging techniques and therapeutic device performance without risk to real patients. Since physical phantoms are used in application-specific acquisition and protocols varying across manufacturing environments, the materials chosen to make the phantoms become critical to the success of their functionality.

The soft tissue-mimicking materials generally used for ultrasound phantoms can be classified into 14 different categories: agarose-based, gelatin based, magnesium silicate based, oil based, water based, open cell foam based, polyacrylamide gel based, polyurethane, polyvinyl alcohol based, tofu, condensed milk based, urethane rubber, Zerdine and Polyvinyl Chloride Plastisol (PVCP) [60-64].

Previous research in [65] has demonstrated that ultrasound compatible materials that mimic soft tissue can be controlled by different mixtures of gelatine, silica powder and an Intralipid solution, where the silica or Intralipid particles generate realistic optical scattering, and the gelatin can maintain good stability and slow bacterial growth. In [66], a precise and thorough method to design a polyvinyl alcohol cryogel (PVA-C) phantom that can be used for both medical microwave and ultrasound is presented. The

final demonstration that its acoustic property is soft tissue mimicking is shown in figure 2.2 [66], the increase of cellulose helps to make the phantom material more compatible to ultrasound imaging (figure 2.2 (panel A)), on the contrary, with the addition of sucrose increases the ultrasound attenuation (figure 2.2 (panel B)). While when focusing on cardiac phantoms used for ultrasound imaging purposes, a partial cardiac phantom, including cardiac atrial structures made with a metal mould, was recently developed. The phantom was mainly designed for surgical applications with an ultrasound-compatible material (gel-wax) and proved to have low acoustic attenuation and reflection [67].

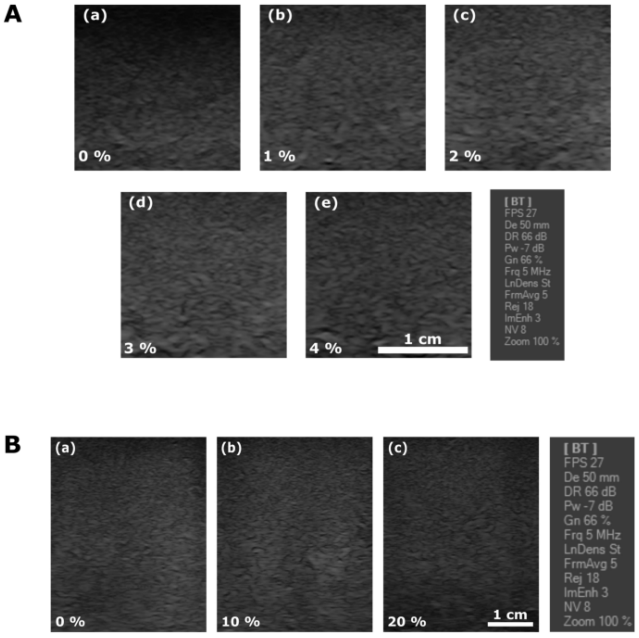

Figure 2.2. Ultrasound images acquired at varying cellulose concentrations without added sucrose (panel A); and at varying sucrose concentrations for a fixed 1% cellulose (panel B) [66]

All these materials have been tested to have similar or lower attenuation and reflection values compared with cardiac tissue, but none can be directly 3D printed, so developing phantoms with complex geometries is still challenging with conventional shaping methods, such as hard negative moulds or liquid perfusion, because they involve

significant work to remove the moulds. This is a particular problem for making cardiac phantoms.

With the development of 3D printing technologies in recent years, production of soft phantoms with complex geometries, using direct 3D printing, has become feasible and could potentially be easier and cheaper for phantom fabrication compared with conventional manufacturing methods. Recently, a complete review was carried out on the use of 3D printing technology for making cardiac phantoms [68]. However, the cardiac phantoms demonstrated in [68] are either sub-parts, such as parts of the aorta only, or are made of clear rigid materials. Other cardiac phantoms, such as the anthropomorphic phantom used to measure surface radiation exposure [69], the foetal cardiac ventricular phantom in 4D sonography [70] and the multipurpose ultrasound phantom used for fast cardiac imaging [71] can produce good images of the heart itself, but they are usually expensive, non-customisable and lack several functionalities when used for specific imaging purposes.

In summary, the ultrasound materials used in previous research are not suitable for 3D printing. The currently available patient-specific ultrasound phantoms are known to be useful in clinical applications, but they are either difficult to manufacture or incomplete without fine geometries, which limits their applications in high-fidelity scenarios.

2.1.3 Current medical applications of cardiac phantoms

Thanks to the advancement of 3D printing, cardiac phantoms can be constructed with multiple colours and materials, like the multi-colour whole cardiac model, the multi-material left heart model and the mitral annulus model with calcium shown in figure 2.3[68], where the original model can be readily generated from a high-spatial resolution cardiac CT, an MRI or through CAD software. These models can help people

to better understand normal and abnormal heart structures compared to 2D images, satisfying the demonstration and education needs [68].

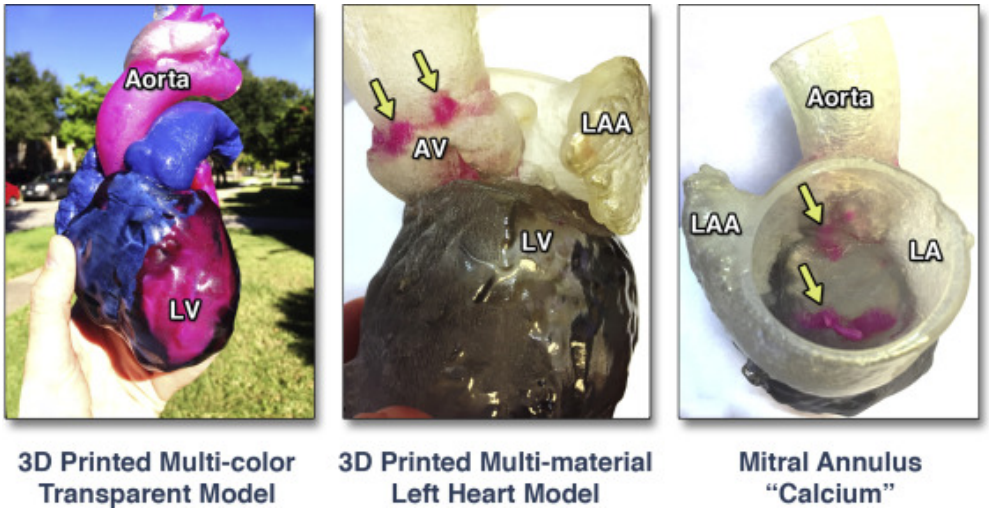

Figure 2.3. Multimaterial and multicoloured patient specific 3D printed heart for educational purposes and communication with patients: multi-colour transparent whole cardiac model, multi-material left heart model, and mitral annulus model with calcium [68]

Except for basic educational functions, cardiac models with various pathologies are also widely used in minimally invasive surgery simulations and for pre-operative planning. Examples include a mitral clip simulation for a mitral valve repair procedure [72] and transvalvular flow volume quantification based on the functional valve model in [68]. As shown in figure 2.4, the mitral clip procedure was carried out on an ultrasound imaging-compatible cardiac phantom with movable mitral valve. This phantom was manufactured using mould assembly with transparent silicone elastomer, and the phantom accuracy was evaluated by calculating the absolute distance between the original patient data and the segmentation's point-cloud dataset. Finally, this phantom was validated by a mitral clip device under ultrasound guidance, which determined its ability to display realistic anatomical and instrumental features [72].

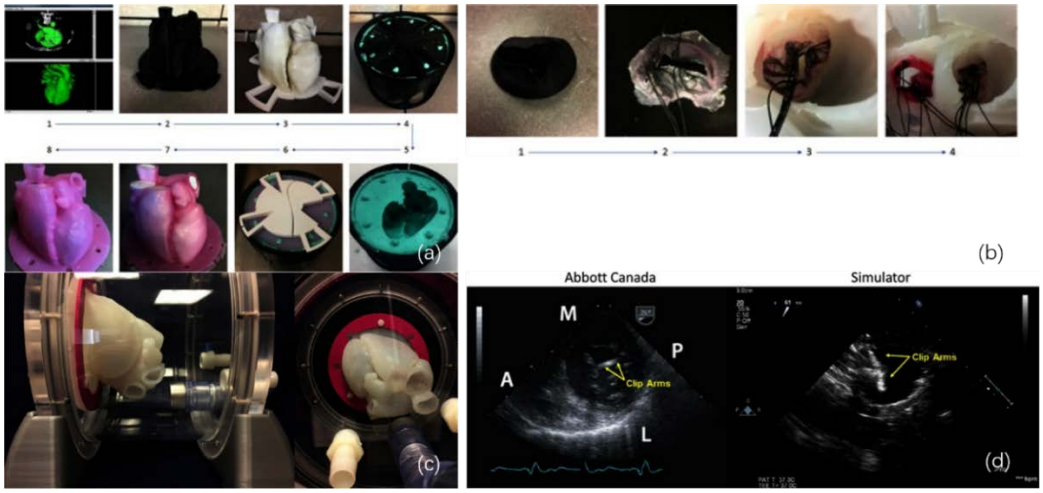

Figure 2.4. Fabrication of silicone cardiac model with valvular structure and its mitral clip simulation under ultrasound [72]

These functional cardiac phantoms give the possibilities of various in-vitro interventional simulation, however, the complicated moulding procedures using silicone or other non-3D printable soft materials result in low-efficiency and difficulty of replication, to simply the fabrication procedure, direct 3D printed functional cardiac phantoms are needed for further research while 3D printable soft materials have to be included as well without losing their multi-modal imaging compatibilities.

2.2 3D Printed Atrial Models and Simulation Applications

The literature review in section 2.2 corresponds to the content in chapter 5: a bi-atrial model made for RF ablation simulation and CARTO3 mapping, with description of atrial anatomies and previous research about atrial model fabrication.

2.2.1 Backgrounds of atrial anatomies and treatment to atrial fibrillation

Catheter ablation is an effective treatment for patients with atrial fibrillation [73] and has become popular choice. During the procedure, catheters will be inserted into the right atrium (RA) first, then the left atrium (LA) is accessed by a transseptal puncture. X-ray imaging/fluoroscopy is used to guide the positioning of devices, which can be challenging [74], while ultrasound imaging is often used to guide the transeptal puncture. However, using fluoroscopy alone is difficult and time-consuming during the creation of lines of the conduction block in the 3D geometry of LA, which encourages the development of new non-fluoroscopic mapping techniques to increase the success rate as well as reduce the X-ray exposure. Electroanatomic mapping systems, such as CARTO3, allow monitoring of device position, creation of 3D chamber geometry and measurement of electrical signals, which significantly improves the clinical outcome [75].

Figure 2.5 [76] shows an example of a left atrium model constructed from contrast enhanced magnetic resonance angiography (CE-MRA) images using semi-automatic segmentation, it contains left atrial (LA) body (light blue), LA appendage (dark blue), left superior pulmonary vein (pink), left inferior pulmonary vein (orange), right superior pulmonary vein (yellow), and right inferior pulmonary vein (green). The fibrotic tissue distribution is incorporated into the segmented model from late gadolinium enhancement magnetic resonance imaging (LGE-MRI), which can help to guide the ablation procedure. While figure 2.6 [77] depicts a more complete model that includes both the left and right atria (LA and RA), pulmonary veins (PV), superior and inferior venae cavae (SVC and IVC), left and right atrial myocardium (LAM and RAM), coronary sinus (CS) and intercaval bundles, as well as the inclination and transverse angles of an atrium’s cross section.

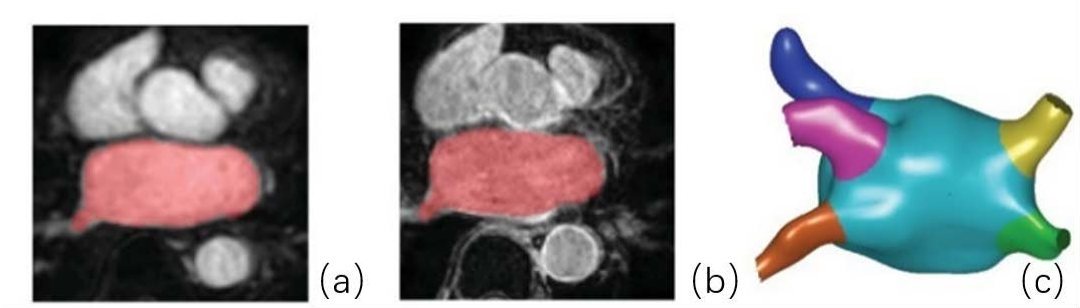

Figure 2.5. Left atrium model construction for atrial fibrillation (AF) simulation (a) Semi-automatic segmentation of contrast enhanced magnetic resonance angiogram (CE-MRA) imaging; (b) late-gadolinium enhancement (LGE) imaging with registered segmentation overlaid in red; (c) 3D left atrium model with labelled regions: left atrial (LA) body (light blue), LA appendage (dark blue), left superior pulmonary vein (pink), left inferior pulmonary vein (orange), right superior pulmonary vein (yellow), and right inferior pulmonary vein (green) [76]

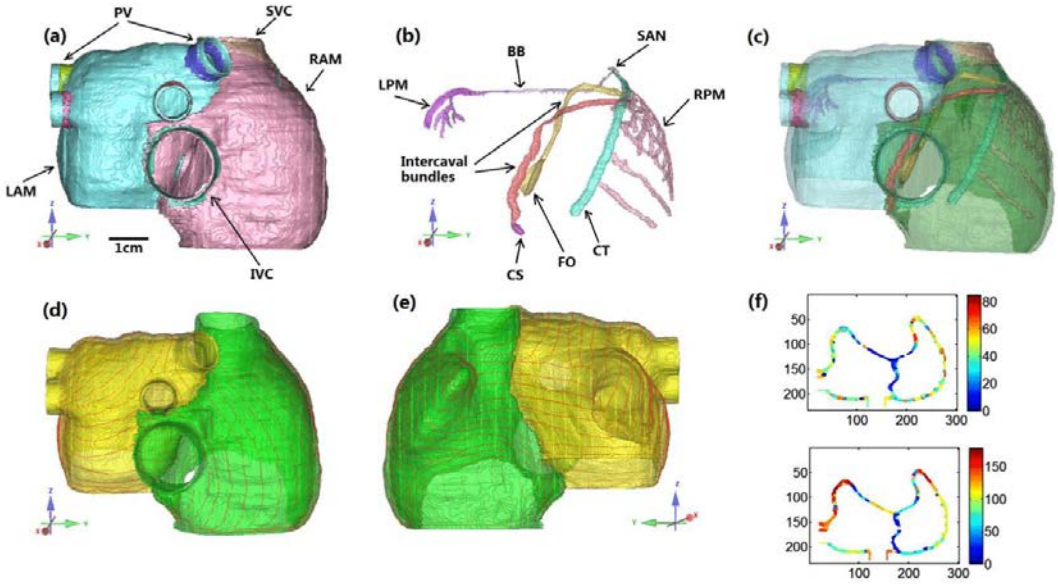

Figure 2.6. Anatomical illustration of bi-atrial models (including both right atrium & left atrium) of patients with fibre orientation and representation of the inclination and transverse angles of an atrium's cross section[77]

2.2.2 Literature review about atrium phantom fabrication

As 3D printing assists cardiologists and cardiac surgeons immensely during intervention and surgical planning [78], it is predicted that this technology will play a revolutionary role in the medical field in recent years [79]. However, to make the fabricated model applicable in specific simulation environments, printed materials must be carefully chosen.

Previously, [80] used 3D printed moulds designed from CT LAA images to manufacture flexible balloon-like devices which could adopt the morphology of LAA after cardiac implantation. However, this study only provides a proof of concept of the feasibility and efficacy of using 3D printed endocardial implants while the printed models cannot be generalised to interventional procedures such as radiofrequency ablation (RFA), as illustrated in figure 2.7 [81], the catheter needs to be inserted into the heart chambers through a vein to create the lesion, and this requires the phantom material has similar response to ablation heat like cardiac tissue. Figure 2.8 [82] gives a more comprehensive description of two cases of LAA models with multimodal imaging, and the corresponding printed atrium model, while figure 2.9 [83] demonstrates how a deformable atrium model can help clinicians in simulating the transcatheter LAA closure procedure using the rubber-like material, Tango Plus. They all show the principle of 3D printed left atrium models in clinical applications, but mainly for demonstrations, while no further functional validation performed on these models.

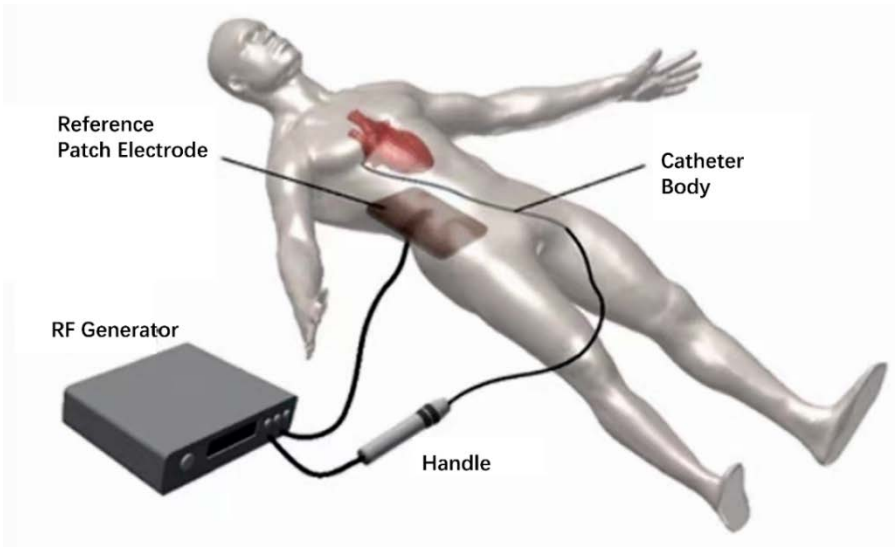

Figure 2.7. Radiofrequency ablation (RFA) setup: a catheter is inserted into a vein (typically in the groin or the neck) and its tip is wire steered within the heart chamber. [81]

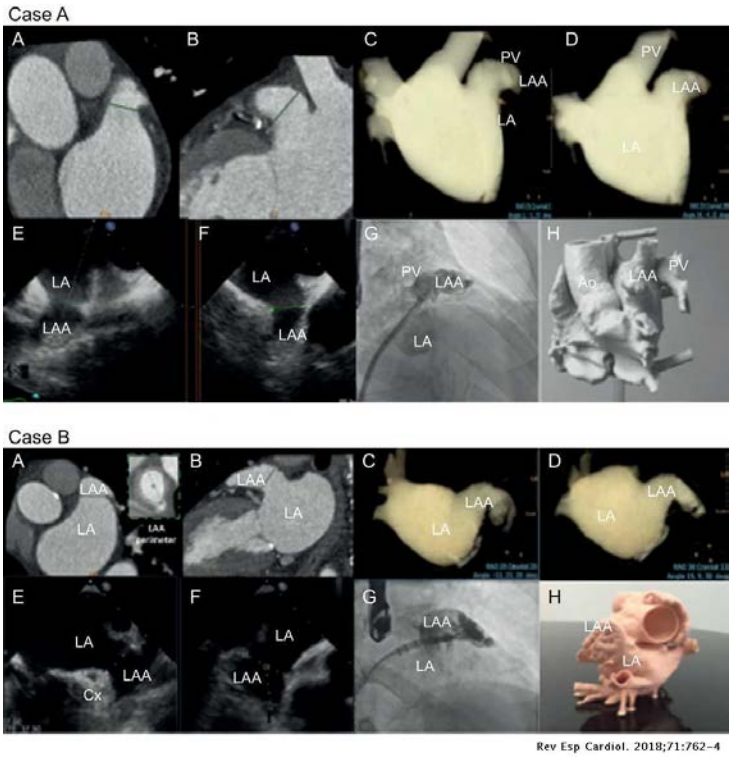

Figure 2.8. Multimodal imaging of LAA in cases A and B. A, B: cardiac measurements via computed tomography. C, D: computed tomography rendering of left atrial volume in working projections. E, F: transoesophageal echocardiographic views (45° and 135°)

showing landing zone. G: right anterior oblique cranial fluoroscopic projections. H: 3D printed model [82]

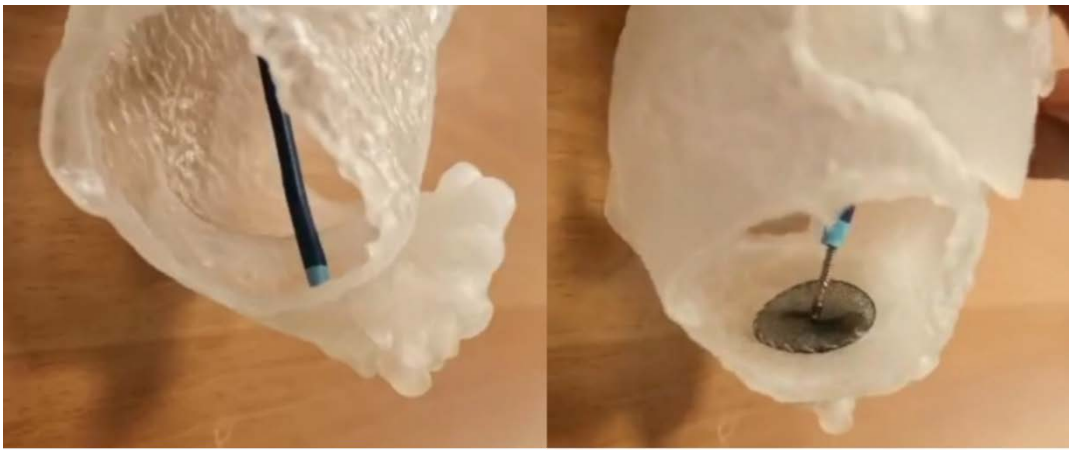

Figure 2.9. 3D printed model of the left atrium to plan atrial appendage closure in challenging anatomy using the rubber-like material, Tango Plus [83]

2.3 3D Printing in Aorta & Valve Model Manufacturing

The literature review in section 2.3 corresponds to the content in chapter 6: manufacturing of anthropomorphic aorta and aortic valves, with illustration about the need of these models and recent research about how 3D printing contributes in their fabrications.

2.3.1 The need of 3D printed aorta & aortic valve models

The aortic valve allows the blood to flow from the left ventricle to the aorta, disease of either the aorta or aortic valve may cause serious morbidity [84]. Disorders of the aorta can cause atherosclerosis (hardening of aorta), hypertension (high blood pressure) and connective tissue disorders [84]. Valvular disease means that one or more heart valves cannot function correctly, and three basic problems occur: stenosis, regurgitation/backflow and atresia.

Patient-specific valve and aorta models can be used during the preparation of minimal invasive surgeries [85]. With the help of these 3D printed models, clinicians are able to better understand patients' valvular structure and mechanical properties and can plan and test the valve-related surgical procedure's efficiency and risks [85]. Additionally, the tactile and three-dimensional feedback provided by the 3D printed valve models helps clinicians to visualise and identify corresponding valvular diseases and associated anatomical changes, such as calcification on the leaflets [86].

Except for being used in surgical simulation, 3D printed prosthetic valves can also be used as implants. Conventional replacement valves are usually made of rigid polymers or animal tissues combined with circular metal frames, which can hardly match real patients' aorta shape. Manufacturing these metallic valves is also expensive and time-consuming, many patients after transplantation have to suffer life-long complications of immune response and take anticoagulants [87]. 3D printed silicone aortic valve models can solve the problem of manufacturing difficulty and replicate the actual valves' shape to the utmost extent. The lead time of production can be reduced from several working days to a few hours, while the cost is reduced to only several dollars with a bio-printer [87]. The manufacturing process of a silicone replacement valve is demonstrated in figure 2.10 (a-j) [87]. The reinforcement patterns were sprayed on the customised aortic root and leaflet mandrels using a custom-built non-planar 3D printer, the valve section was combined with the negative mould of the root-shape mandrel, and the complete replacement valve was produced.

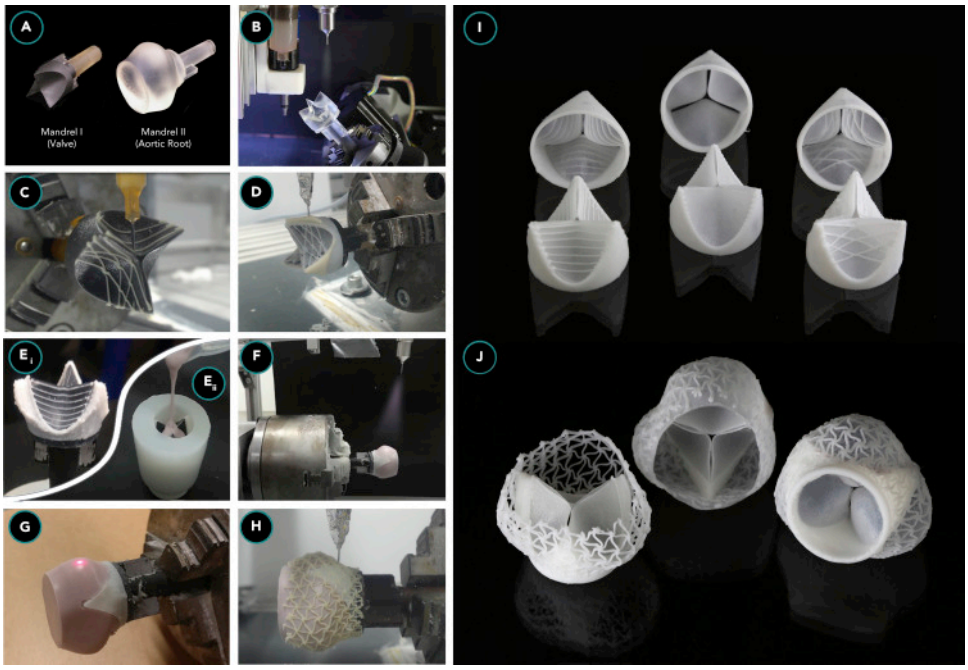

Figure 2.10. Multi-material additive manufacturing process used for the fabrication of customised silicone heart valves: (a) mandrel supports of aortic root; (b) valve-shaped mandrel; (c-e) customised inter-leaflets; (f) valve with soft silicone membrane; (g) auxetic valve outer surface; (j) complete silicone replacement valve [87]

Apart from the valve model, 3D printed aorta models can also benefit surgeons as a supportive tool. Standard interventional procedures for this include implantation of stent-grafts through the femoral artery, or custom aortic prostheses. Stent-grafts are not patient-specific but patient-specific aortic prostheses manufacturing is expensive and time-consuming [88]. The emergence of 3D printed aortic prostheses and customised stent-grafts improve the implanted model accuracy as well as reduce the manufacturing time frame from several weeks to only several hours, as shown in figure 2.11 [88], the customised stent-graft was designed based on a patient-specific 3D printed aorta model, physicians now are able to optimize the surgical procedure and limit the complication after aortic aneurysm treatment.

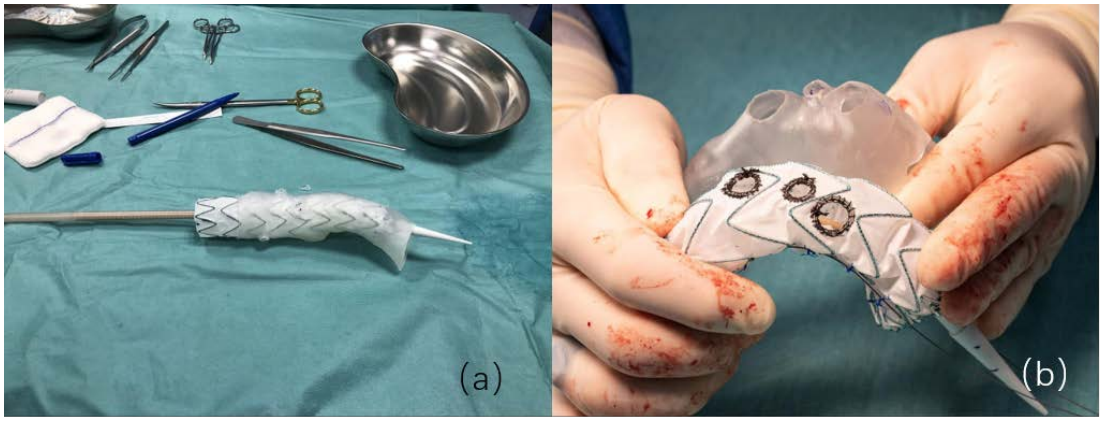

Figure 2.11. Using 3D printed aorta models that are based on the patient's anatomy to create custom stent-grafts [88]

With the prevalence of aortic-valve implantation and repair, medical imaging assessment has become increasingly important for preoperative interventional or surgical planning. Echocardiography is the key tool in the primary diagnosis of AS, as it provides information of essential areas of valve pathologies, as shown in figure 2.12 (b), in which the calcification of the valve leaflets is highlighted together with a wider left ventricle outflow tract than the same area in figure 2.12(a) [89]. The combination of short- and long-axis echo images can describe the thickness, calcification level and number of cusps of the aortic valve. Additionally, the combination of imaging and Doppler determines the level of valvular obstruction. Continuous-wave (CW) Doppler through the aortic and mitral valves produces filled waveforms, enabling this mode to measure blood-flow velocity higher than 2 m/sec, while pulsed-wave (PW) Doppler, which produces unfilled waveforms, can only measure blood velocities lower than 2 m/sec [90]. Measured peak velocity can be used to calculate the maximum pressure gradient, $\boldsymbol{P_{max}}$, and the whole systolic wave area can be used to calculate the mean pressure, $\boldsymbol{P_{mm}}$.

Figure 2.12. Ultrasound imaging of the aortic root: (a) Left ventricular outflow tract diameter measured in zoomed parasternal long-axis view; (b) example of a patient with calcification [89]

2.3.2 Current 3D printing in aorta and valve model manufacturing

Previously, [91] summarised a systematic review of commonly used 3D-printing materials to create various valve models, such as ABS, Tango Plus and FullCure 930. Customised silicone and hydrogel printers have also been developed to directly print some non-mouldable models.

Figure 2.13 [92] demonstrates the workflow for creating an aortic valve model. The first step of is to acquire high-resolution volumetric cardiac medical images such as CT or MRI in a DICOM (digital imaging and communication in medicine) format. The second step is segmentation focusing on the area near the aortic valve to create patient-specific valve models with part of the aorta and aortic root. This is a multi-step process, which includes the pre-processing of image slices and postprocessing of segmented meshes. The segmented digital models are then exported as 3D-printable files, typically as an STL file. The main adjustments of an STL file include error repairing, surface smoothing, mirroring and the elimination of extra meshes. The final step is to load the valve model into slicing software and start printing. The material is chosen based on simulation requirements, and sometimes multiple materials are used to represent

different anatomical elements [91], for example, the calcification area will use more rigid materials than the normal valve tissue, and the material of the aorta needs to be more durable than the leaflets.

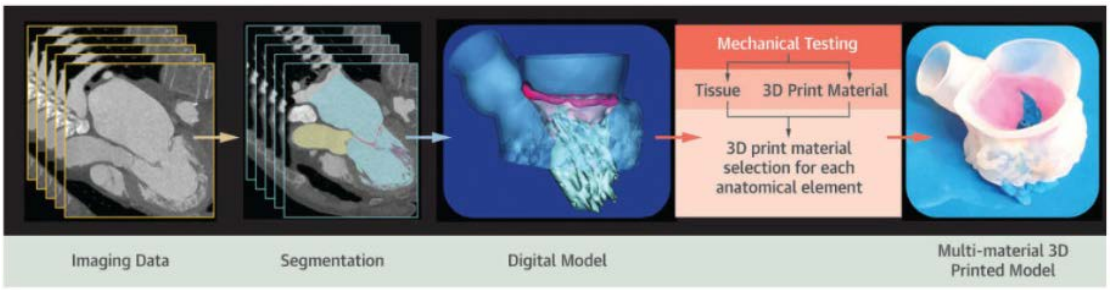

Figure 2.13. Cardiovascular 3D-printing workflow of an aortic valve, including the acquisition of imaging data, segmentation and actual 3D printing [92].

Figure 2.14 [93] demonstrates a multi-material aortic-root model with an embedded internal sensor array. It is comprised of three different materials to represent the main aorta, the leaflets and calcifications. The sensor array inside can facilitate the contact pressure measurement and locations in the valve's region of interest. The use of this model helps inform the implantation size and risks of post-TAVR disturbance [93].

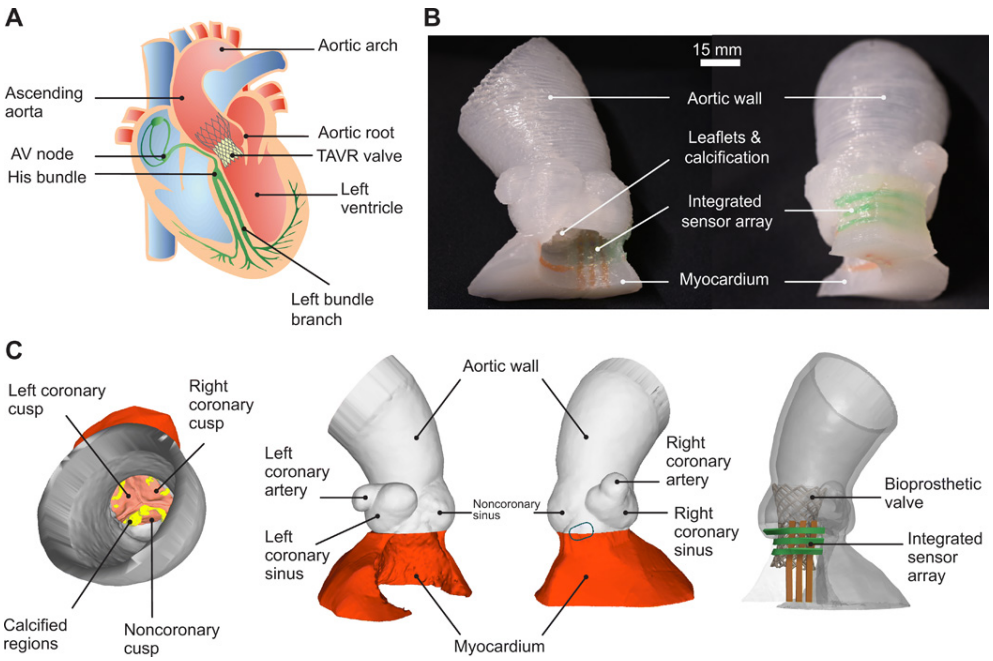

Figure 2.14. Overview of a patient-specific 3D-printed aortic-root model concept and components for the TAVR procedure [93].

A typical tissue-mimicking valve or aorta model manufacturing technique is printing casts and moulds and then dipping or coating with materials such as silicone. Figure 2.15 [94] provides examples of a mould for mitral, tricuspid and complete atrioventricular canal (CAVC) valves. To reduce the manufacturing difficulty, these valve models are only composed of essential leaflets, while the aortic root is eliminated so the mould can be flat and smooth. Surgeons involved in relevant experiments consider silicone valve models to be useful in cardiac surgical and interventional cases. However, deeper analysis is still required to meet the needs of more complicated designs of valve moulds. To be more explicit, the moulds designed can only produce 2D or shallow 3D valvular structures with silicone materials. If clinical cases require using more complete 3D silicone models with structures like those shown in figure 2.13, these type of surface moulds printed only using PLA are not suitable. Thus, a more separable mould design is desired, and other printing materials need to be investigated to solve the problem of mould removal.

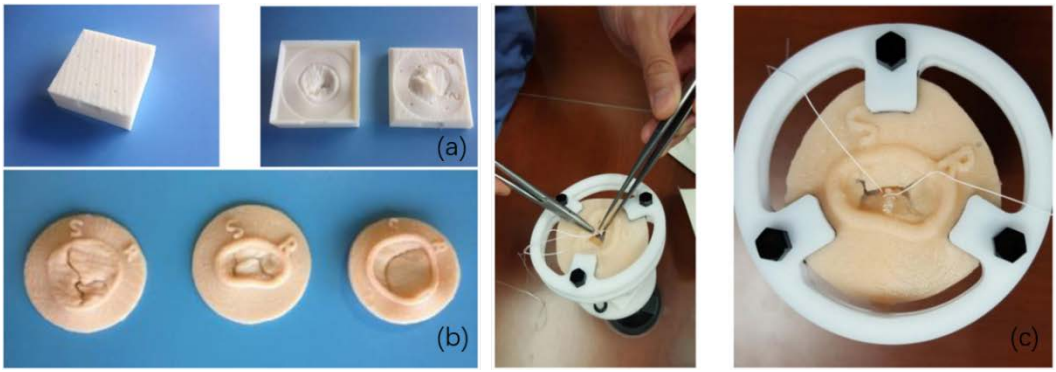

Figure 2.15. (a) Moulds and (b) silicone valves in order from left to right: tricuspid, CAVC, mitral; (c) surgical practice of suturing techniques on a CAVC valve model [94].

Apart from the moulding method, silicone valve phantoms can also be directly 3D printed thanks to the advances of silicone printing technique. [12] has combined a mixing chamber and controlled heating system based on an open-source FDM printer to print a specific type of commercial silicone – Dragonskin VF10 (Smooth-on, the USA), but the commercial silicone materials are too limited in both flexibility and

viscosity to be applied to broader healthcare cases. Further modifications of the silicone inks are thus required for using the silicone printing technique in valve model manufacturing.

2.4 Conclusions and Relation to Following Chapters

From the different cardiac models presented in the current literatures, it can be concluded that most of 3D printed models are mainly for demonstration purposes without further validations using medical devices, or expensive and non-customizable. While most soft tissue-mimicking materials lack 3D printability, the conventional moulding techniques limit their uses in creating complicated geometries. Advances in 3D printing bring more 3D printable soft materials like TPU and flexible resin materials, however, their flexibility could be hardly compared to biological tissue's, thus, not suitable for making functional anthropomorphic cardiac models directly.

The research in this thesis explores a novel 3D printable soft material—Layfomm40 and new manufacturing techniques using another soft tissue-mimicking material—silicone as supplement. The key materials were first characterised in chapter 3 with detailed analysis of their strengths/weaknesses, and relevant physical property comparisons to tissue's. The various cardiovascular phantoms produced using the selected materials in the following "results" chapters 4-6 could demonstrate high anatomical fidelities to patients' ones from both visual inspection and multi-modal medical imaging. The combination with other components such as smart materials also endows these cardiac models with more functionalities. Meanwhile, the inexpensive and easy fabrication procedures using Layfomm40 and silicone promote their wider uses in the future.

3. MATERIAL CHARACTERISATIONS

3.1 Introduction to Material Characterisation

As stated in the list of objectives in section 1.1.2 of the thesis introduction, the main soft materials used in the thesis were Layfomm40 & silicone rubbers, before using these materials to fabricate various cardiac models described in chapter 4-6, they were characterised and compared using the following methods:1. mechanical property tests, including Young's modulus & hardness tests of Layfomm40 & commercial silicones, three-point bending test for the selection of proper moulding materials when two-part moulding technique was applied; 2. ultrasound acoustic property test, which was mainly for the selection and validation of ultrasound compatible 3D printing materials to make the whole cardiac phantom; 3. optical microscope observation of Layfomm40 material after rinsed with water, saline and thermochromic solution, which was mainly for the demonstration of its structure change from microcosmic level; 4. thermal & electrical conductivity tests and comparisons between Layfomm40 & other conductive 3D printing materials, which was for the validation of Layfomm40's compatibility of the radiofrequency ablation system; 5. rheological characterisation of modified silicone inks with fumed silica powder addition, for the fabrication of valve model using direct silicone printing technique.

Mechanical testing was the main characterisation method used throughout the whole thesis, it can be not only used to determine the similarities/differences between the phantom materials and cardiac tissue, but also used to select the most suitable moulding material in case moulding technique was applied for silicone model fabrication. Thus, Layfomm40, silicones and another 3D printable soft material—Tango Plus were characterised in terms of Young's modulus and hardness, the characterisation results were used for the whole cardiac model fabrication in chapter 4, and the aorta & valve

model fabrication in chapter 6; while different dissolvable moulding materials were compared in terms of flexural modulus in addition to their water solubility, the relevant results were used for the two-part moulds fabrication in chapter 6. It is worth mentioning that, even though printed silicone specimens have different mechanical performances with moulded silicone specimens, as the focus of the mechanical characterisation was the effect of fumed silica powder addition instead of the manufacturing technique, to simplify the specimens' fabrication procedure, the mechanical characterisation of the new silicone inks used in silicone printing section of chapter 6 was based on moulded silicone specimens.

Ultrasound acoustic property testing was mainly used to determine the materials' ultrasound compatibility quantitively, the testing results can be regarded as complementary data for the qualitative ultrasound imaging results demonstrated in chapter 4.

The optical microscope observation and conductivity testing of Layfomm40 were the main characterisations for the fabrication of bi-atrial ablation phantom in chapter 5, the microscope characterisation proved Layfomm40's capability of saline water or thermochromic solution absorption, and the conductivity characterisation proved its compatibility to the radiofrequency ablation system.

Even though the original silicone materials' viscosities were provided from open-source instructions, the effect of fumed silica powder addition in the modified silicone inks for silicone printing in chapter 6 remained unknown from previous literatures. The finale rheological characterisation focused on the new silicone inks' viscosity changes along different fumed silica power amount and temperature; the relevant results were then used to help determine the parameter settings of the silicone printer to make valve model comparable to moulded counterparts in chapter 6.

3.2 Mechanical Property Testing

3.2.1 Comparison Between 3D Printable & Unprintable Soft Materials

3.2.1.1 Young's modulus & hardness tests of novel 3D printable materials and commercial silicones

Before fabricating the phantom, it is necessary to choose materials suitable for the representation of soft tissue. In order to reduce the 3D printing difficulties, the selected material needs to be easily 3D printable. A key selection criterion is flexibility. This was evaluated for both elasticity in tension and resistivity to indentation, by measuring Young's modulus and Shore A hardness respectively [15]. And the flexibility results of new 3D printable soft materials were compared to the results of three types of room temperature vulcanising (RTV) silicones, the RTV silicones were chosen for comparison as they were regarded as common tissue-mimicking materials. The 3D printable soft materials tested were the Poro-Lay series including Layfomm40, Layfomm60 and Gel-Lay; Tango Plus; silicones including Jehbco silicone, RTV silicone Ecoflex-0020 (silicone 0020) and RTV silicone Ecoflex-0050 (silicone 0050).

The hardness could be measured with a durometer [15], it measures the depth of an indentation in the material created by a given force on a standardised presser foot. While Young's Modulus [15] describes the elastic properties of a solid undergoing tension in one direction only. Figure 3.1 shows an example of the load-extension curve, and Young's modulus is the slope of this curve. It can be calculated with the equation $E = \frac{FL_0}{A\Delta L}$, where E is the Young's modulus, which should be a constant, F is the force exerted on the object under tension, A is the cross-sectional area perpendicular to the applied

force, ΔL is the length by which the object changes when the force is applied and L_0 is the original length of the object [95].

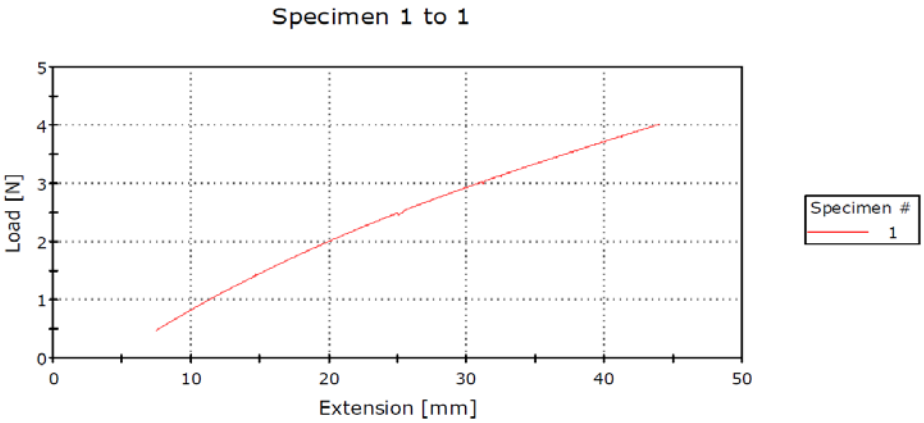

Figure 3.1. Load-extension curve example of silicone 0050. samples recorded by Instron 3343 tensile machine and Bluehills software.

In the following experiments shown in figure 3.2 (a), the durometer measurement was performed with a Shore A durometer tester on prepared 5 cm thick samples according to the user manual, and all the results were read directly from the tester's digital screen. And in figure 3.2 (b), the Young's modulus was measured using a tension test machine (Instron 3343) with a 4 mm thick and 10 mm wide ISO 527 Type 1B specimen. During testing, the machine's clipping hands stretched the specimen until manually stopped. For each material, the test was repeated 20 times in order to reduce random errors, and the full dataset was recorded and exported using Bluehills, the built-in software, and further analysed in MATLAB 2017. The Instron sample holding arms move slowly when the motor is activated; the Young's modulus can then be calculated from the recorded extended distance and loading force.

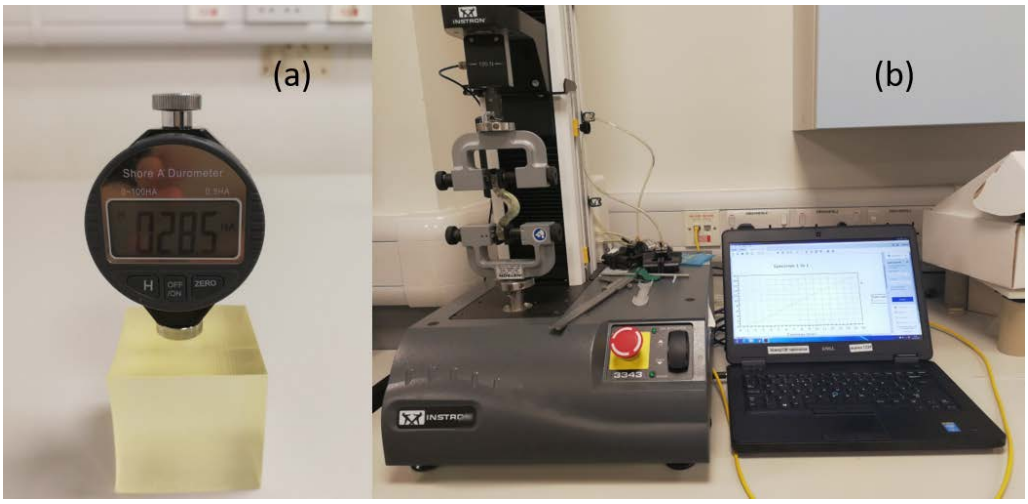

Figure 3.2. Stiffness testing experimental setup: durometer testing (a) and Young's modulus testing (b)

Tables 3.1-1 and 3.1-2 summarise the flexibility (hardness and Young's modulus) comparison results between different 3D printable unprintable materials, respectively. *PolyJet Materials Data Sheet* published in 2016 reported that the Young's modulus of Tango Plus is between 0.1 and 1 MPa (equivalent to 100-1000 kPa), while RTV silicone has a smaller Young's modulus of 0.01 to 0.2 MPa (equivalent to 10-200 kPa). Except for Jehbco silicone, the stiffness testing results for these materials agree with the results in the above literature. As for the Shore A hardness, Tango Plus demonstrated a durometer measurement between 26 and 29 HA in [16], which is also consistent with the tests presented here.

Table 3.1-1. Flexibility comparison between different 3D printable materials

Samples	Layfomm40	Layfomm60	Gel-lay	Tango Plus
Durometer (HA)	4 (min)	16.5	17	29 (max)
Young's Modulus (kPa)	128.5 (min)	584.8	1493.7 (max)	609.5

Table 3.1-2. Flexibility comparison between different unprintable materials

Samples	Silicone 0050	Silicone 0020	Jehbco Silicone
Durometer (HA)	5	2.5 (min)	39 (max)
Young's Modulus (kPa)	96.5	17.8 (min)	2350.0 (max)

Table 3.2. Advantages & disadvantages of 3D printable and unprintable soft material

Type	Materials	Advantages	Disadvantages
3D Printable Materials	Poro-Lay Series	Porous, flexible and conductive after immersion in water	Delaminated and dried out easily, low printing quality, low durability
	Tango Plus/Agilus Series	High printing quality and good durability	Low flexibility and unclear ultrasound imaging performance
	TPU/TPE Series	Good durability, low cost	Very low flexibility and very bad medical imaging performance, low printing quality
Unprintable Materials	Silicone	Very high flexibility, durability and multi-modal imaging performance	Slow curing process
	PVA-C	Low viscosity, very high flexibility and very low ultrasound attenuation	Complicated freeze–thaw cycle so not water soluble, low durability, high frangibility
	Paraffin/Agarose	Low viscosity, very high flexibility and very low ultrasound attenuation, recyclability	High melting point, low durability, high frangibility

Even though the 3D printable material--Layfomm40's flexibility could satisfy the requirements to make an ultrasound compatible cardiac phantom for static simulations, its low durability compared to silicones limits its applications in dynamic experiments. Table 3.2 summarises the advantages and disadvantages of these 3D printable and unprintable materials. From the table, it can be concluded that all the current 3D printable materials are limited by their low flexibility or poor printing quality, and among the unprintable materials, Ecoflex and Dragonskin perform better than PVA-C, agarose and hydrogel in terms of their durability and ease of use. Thus, typical silicone materials were considered to make the aorta/valve phantom for the flow test in chapter 6. Using the same setup in figure 3.2, the silicone material candidates were also characterised in terms of flexibility, and the results were presented in table 3.3, together with the flexibility of aorta and valve leaflets [17,18, 96].

Table 3.3. Flexibility comparison between potential aorta and valve phantom materials: 3D printable soft materials and traditional silicone rubbers

	Shore A Hardness	Young's Modulus (kPa)
Aorta	13.4±1.9 [17]	701-983 [96]
Valve leaflets	N/A	62 [18]
Agilus30	30	431
Agilus40	40	476
Agilus50	50	571
Agilus60	60	784
Tango Plus	26–28	609.5
Flex100 Resin	38	1,365
Dragonskin 10	9.5	109
Dragonskin 20	20.5	427
Ecoflex 0010	0.5	16
Ecoflex 0030	3	55
Ecoflex 0050	5	97

3.2.1.2 Young's modulus & hardness tests of modified silicones

The previous commercial silicone materials used to make the aorta & valve listed in table 3.3 were not viscose enough to be printable, by adding certain amount of fumed silica powder, the modified silicone inks could form the filament shape and be used as printable materials. However, the powder addition will affect the printouts' mechanical properties, which could further affect the printouts' functionality. Thus, the Young's modulus and hardness of cured silicone specimens with different amount of fumed silica were also analysed and compared. As the focus of the modified silicone inks' mechanical characterisation was the effect of fumed silica powder addition instead of the manufacturing technique, to simplify the specimens' fabrication procedure, the mechanical characterisation of the new inks used in silicone printing section of chapter 6 was based on moulded silicone specimens.

The tested modified silicone inks involve four types of Smooth-on silicone materials as they have obvious viscosity and flexibility differences: Dragonskin 10, Dragonskin 20, Ecoflex 0010 and Rebound 25. The amount of added fumed silica to make a printable ink varies according to the type of silicone base. For Dragonskin 10 and 20, the range is 20–50%, for Rebound 25, the range is 20–40% and for Ecoflex 0010, the range is 40–60%, these values were determined from experimental printing performances based on their original mixed viscosities, and the amount of added fumed silica powder was measured in a glass Pyrex beaker by volume percentage.

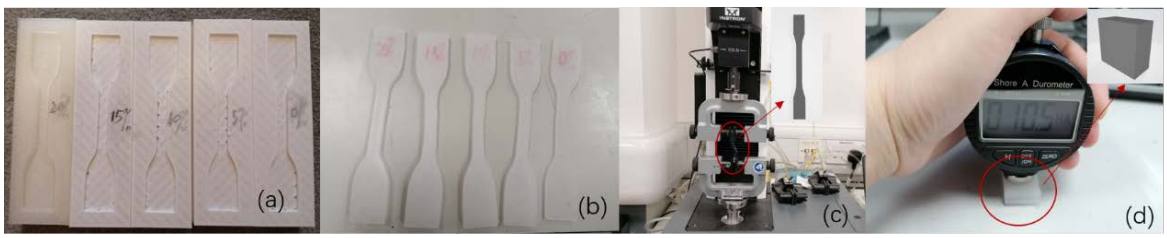

Figure 3.3 Silicone specimens (ASTM type II) for testing flexibility: (a) specimen moulds; (b) specimens with different amounts of fumed silica; (c) Young's modulus test with Instron 3343 tensile machine; (d) hardness test with Shore A durometer

Figure 3.3 (a, b) shows the modified silicone specimens' preparation with different amounts of added fumed silica, and the flexibility characterisation setups shown in figure 3.3 (c, d) are the same as previous setup in figure 3.2. All corresponding flexibility results are listed in tables 3.4-1 and 3.4-2, which demonstrate that the use of fumed silica powder could increases the silicone materials' flexibility (both hardness and Young's modulus), but in a small range.

Table 3.4-1 Shore A hardness of various silicone inks (HA)

Fumed Silica Addition (v/v)	Dragonskin 10	Dragonskin 20	Ecoflex 0010	Rebound 25
0%	10.0	22.0	0.5	21.5
10%	12.0	23.5	0.5	22.5
20%	13.0	24.5	0.5	24.0
30%	14.5	26.0	1.0	26.0
40%	15.0	27.5	2.0	27.5
50%	16.0	28.5	2.5	/
60%	/	/	2.5	/

Table 3.4-2 Young's modulus of various silicone inks (kPa)

Fumed Silica Addition (v/v)	Dragonskin 10	Dragonskin 20	Ecoflex 0010	Rebound 25
0%	151.62	386.55	15.76	372.17
10%	169.54	390.47	20.68	417.34
20%	202.94	443.00	24.74	446.08
30%	217.96	466.13	32.57	513.90
40%	224.03	470.65	41.01	535.96
50%	273.46	559.30	47.92	/
60%	/	/	54.2	/

3.2.2 Moulding Material Comparison

As silicone rubber was considered to be the best material type to make the aorta and valve phantoms, before the mould-based technique was applied, the suitable moulding material should be selected based on the following requirements: it must dissolve easily with simple solvents and be stable when external force is applied.

3.2.2.1 Water solubility of different moulding materials

Separate water solubility test was performed before mechanically characterising different moulding materials using three-point-bending test [97].

There are several water-soluble 3D-printing materials available on the market, including PVA (Technologyoutlet, Amazon, UK), High-T-Lay (Kai Parthy, Germany) and Lay-PVA (Kai Parthy, Germany), which fulfil these criteria. From the initial experiments, a full infill density of 100% and room-temperature water environment were chosen, and the dissolving process took several days, which was longer than expected. Thus, it was necessary to compare the three selected moulding materials in terms of different infills and their solubility at different water temperatures, finding the optimal dissolving parameters will speed up the manufacturing process and avoid wasting time on unnecessary printing.

The specimen used for the infill density experiment was a 3 x 3 x 3 cm^3 cube with a discrete infill density range of 0% to 100%, and the dissolving water temperature was controlled at 25℃. The specimen used for the water-temperature experiment was a 1 x 1 x 1 cm^3 cube with 0% infill, and the water temperature was controlled from 25℃ to 100℃. The dissolving procedure was monitored by a surveillance camera (YI Dome Camera) and manually recorded from the starting point to the fully dissolved point.

The water solubility results are presented in tables 3.5-1 and 3.5-2: the printed PVA cube with 0% density can be fully dissolved within just 1.62 hours, the Lay-PVA cube needs 4.75 hours, which is around 3 times that of PVA, while the High-T-Lay cube needs 36.08 hours, which is more than 22 times that of PVA. Meanwhile, the dissolving time increases exponentially with specimen infill density; for example, the 100% PVA specimen needs 377.83 hours to fully dissolve, which is around 233 times that of the 0% PVA specimen.

Table 3.5-1. Moulding material dissolving time comparison with different infill densities (@ room temperature of 25℃).

Infill Density (%)	Time Taken to Dissolve (Hours)		
	PVA	High-T-Lay	Lay-PVA
0	1.62	36.08	4.75
20	10.43	163.08	58.38
40	24.43	367.50	173.42
60	116.42	656.42	284.73
80	263.33	858.25	397.57
100	377.83	1,028.17	494.28
Average Time	132.34	518.25	235.52

Table 3.5-2 shows that PVA is the best water-soluble material at various water temperatures, while with a higher temperature, all the tested materials dissolve more rapidly; for example, the time needed for 0% PVA to dissolve at 25℃ is 93 minutes, which is nearly 3 times of the time at 100℃.

Table 3.5-2. Moulding material dissolving time comparison at different temperatures (@ 0% infill density).

Temperature (℃)	Time Taken to Dissolve (Minutes)		
	PVA	High-T-Lay	Lay-PVA
25	93	2,124	311
40	72	1,324	314
60	50	1,293	309
80	42	1,290	310
100	33	1,285	306
Average Time	58	1,463	310

3.2.2.2 Bending tests of different moulding materials

In addition to the dissolving time, the performance of the moulding material when external force is applied also needed to be considered, as the moulds would be fixed with clamps before the silicone was poured in. Thus, a three-point bending test [97] was performed to compare the material's flexural modulus [98]. The three-point bending test is used to analyse a solid material's static behaviour under certain axial- and lateral-loading forces [99]. The results can be plotted via force-extension curves, and parameters such as flexural modulus and failure force can then be calculated from this curve.

The specimens for this test were prepared as 10 x 2 x 1 cm^3 cuboids with infill density ranging from 20% to 100%, and a Zwick Roell Z010 tensile-testing system was used. The experimental setup is shown in figure 3.4. Before activating the tensile machine, the specimen was placed in the middle of the fixture, and the bottom pivots on both sides were the same to guarantee data precision. During testing, the punch was carefully lowered at a pre-defined speed until the specimen was crushed, then the relevant curve

was generated using testXpert II software (Zwick Roell, Germany). Following the experiments, the recorded data were analysed in Matlab 2019. The failure force when the specimen cracks is simply the maximum loading force, and the flexural modulus that represents the material's strength could be calculated using the equation $E_f = (L^3 m)/(4bd^3)$ in [97], where E_f is the flexural modulus, L is the support span, b is the width of the specimen, d is its depth and m is the gradient of the initial straight-line portion of the load-extension curve:

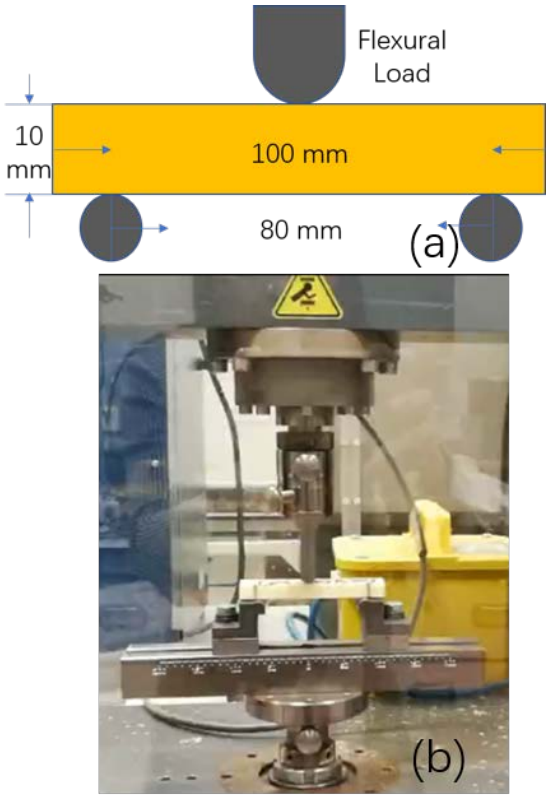

Figure 3.4. (a) Illustration and (b) experiment of the three-point bending test.

Tables 3.6-1 and 3.6-2 present the failure-force and flexural-modulus results of the materials, from which we can see that Lay-PVA can withstand the highest external force and PVA can withstand the lowest; the average load force of Lay-PVA is 630 N, which is 2.57 times that of PVA; Lay-PVA also has the highest flexural modulus with an average value of 1412 MPa, and PVA has the lowest value of 242 MPa. Meanwhile,

with higher infill density, the failure force of all the specimens increases with increments between 20% and 100% ranging from 301 N (PVA) to 936 N (Lay-PVA).

Table 3.6-1. Moulding material failure force comparison

Infill Density (%)	Maximum Load Force (N)		
	PVA	High-T-Lay	Lay-PVA
20	134	111	216
40	163	157	497
60	165	297	546
80	326	429	737
100	435	522	1,152
Average Force	245	303	630

Table 3.6-2. Moulding material flexural modulus comparison

Infill Density (%)	Flexural Modulus (MPa)		
	PVA	High-T-Lay	Lay-PVA
20	137	489	612
40	144	705	906
60	148	972	1,276
80	276	1,244	1,815
100	506	1,656	2,454
Average Modulus	242	1,013	1,412

3.3 Ultrasound Acoustic Property Testing

In addition to the stiffness and hardness measurements, the material's ultrasound acoustic properties were measured and used as a reference for the selection of the ultrasound phantom material. The following experiment examined pixel intensity in the ultrasound image (under a consistent gain setting), attenuation, speed of sound, acoustic impedance and reflection coefficients/backscattering.

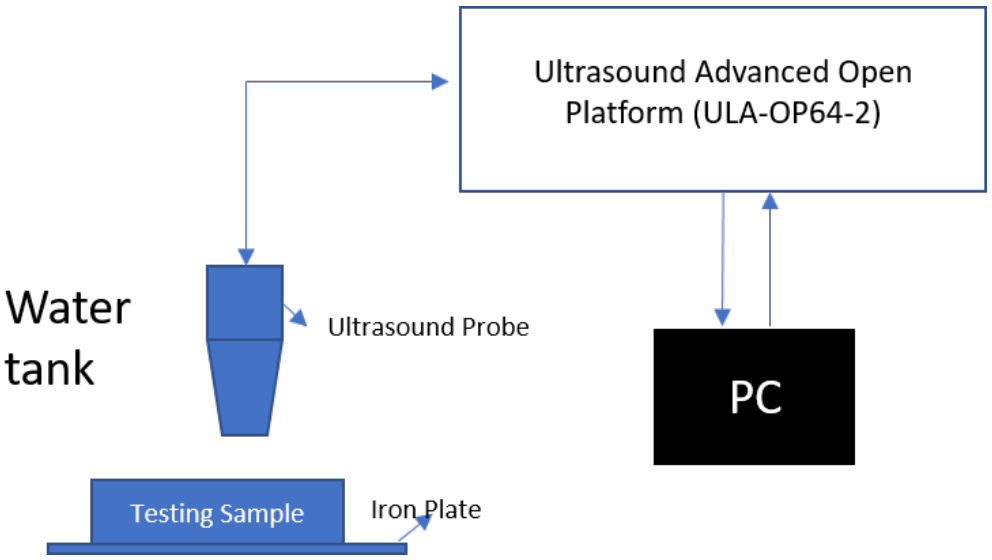

Figure 3.5. Ultrasound experimental setup with ULA-OP-64-2

The samples for the pixel intensity test were 5x5x5 cm cubes for the materials previously mentioned, and the 2D ultrasound images were acquired using the x3-1 transducer on the iE33 ultrasound machine (Philips, The Netherlands). Because different materials have different attenuations for ultrasound waves, they were prepared at different thicknesses with flat surfaces for the other acoustic parameter tests in order to ensure each sample's attenuation could be calculated. The pulse-echo method [60] was used for acoustic testing with a single-sided broadband linear LA332E-2 probe (Esaote, Italy) operating at 1.5 MHz, as higher frequencies could not penetrate through the materials. The detailed experimental setup is illustrated in

figure 3.5, where the iron plate is placed on the bottom as the reflection reference, using non-contact ultrasound imaging. All acquired data was then processed by the Ultrasound Advanced Open Platform (ULA-OP64-2) [19] and analysed using MATLAB 2017.

Figure 3.6 [100] shows the ultrasound wave signal acquired during pulse-echo testing. From the signal's travel time, the velocity can be calculated using equation (3.1), and from the amplitude difference, the attenuation can be calculated using equation (3.2). To reduce random errors, for one sample the signal acquisition was repeated for 100 cycles, and all the post processing was averaged. In the velocity calculation, c_s is the acoustic velocity in the sample, c_w is the acoustic velocity in degassed water (1.48 × 106 kg/m^2/s), d is the sample thickness, measured separately, and ΔT is the time shift upon displacement of water with the sample in place. The attenuation and backscattering coefficients can be calculated from the log difference between the two acquired spectra in equation (3.2), where α is the attenuation coefficient, u is the backscattering coefficient, $A\,(x, y, f)$ is the magnitude of the spectrum with the sample in place and $A_0(x, y, f)$ is the magnitude of the spectrum with no sample in place.

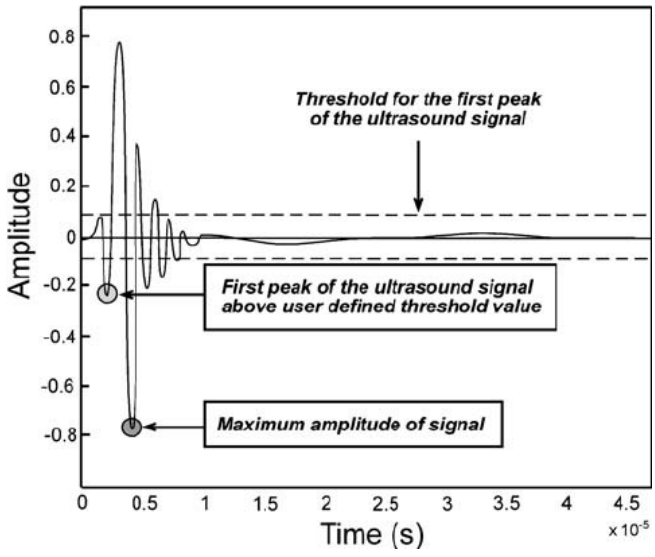

Figure 3.6. Ultrasound signal for attenuation and velocity calculation [100]

Besides velocity and attenuation, some other derived acoustic values can be calculated using equation (3.3), as stated in [101]. The pressure amplitude reflection coefficient r, the pressure amplitude transmission coefficient t, the intensity reflection coefficient R and the intensity transmission coefficient T can be calculated using equation (3.3), where water is taken as the reference impedance Z_1 with a value of 1.48× $10^6 kg/m^2/s$. The acoustic impedance can be calculated from Z = cρ, where c is the velocity transmitted in the sample, ρ is the material's density. The ultrasound images of different materials under the same ultrasound machine settings are depicted in figure 3.7 together with their pixel values. It can be seen that Poro-Lay materials, including Layfomm40, Layfomm60 and Gel-Lay, have similar pixel intensities varying from 152 to157 (the highest), silicone materials have similar pixel intensities (the medial) from 124-127, and Tango Plus has the lowest pixel intensity of 58.88.

$$\frac{1}{c_s} = \frac{1}{c_w} - \frac{\Delta T}{2d} \qquad (3.1)$$

$$\alpha = -\frac{20}{2d} log_{10} \frac{A(x,y,f)}{A_0(x,y,f)} \left[\frac{dB}{cm}\right], u = -20log_{10} \frac{A(f)}{A_0(f)} \text{ [dB]} \qquad (3.2)$$

$$r = \frac{Z_2 - Z_1}{Z_1 + Z_2}, t = \frac{2Z_2}{Z_1 + Z_2}, R = (\frac{Z_1 - Z_2}{Z_1 + Z_2})^2, T = \frac{4Z_1 Z_2}{(Z_1 + Z_2)^2} \qquad (3.3)$$

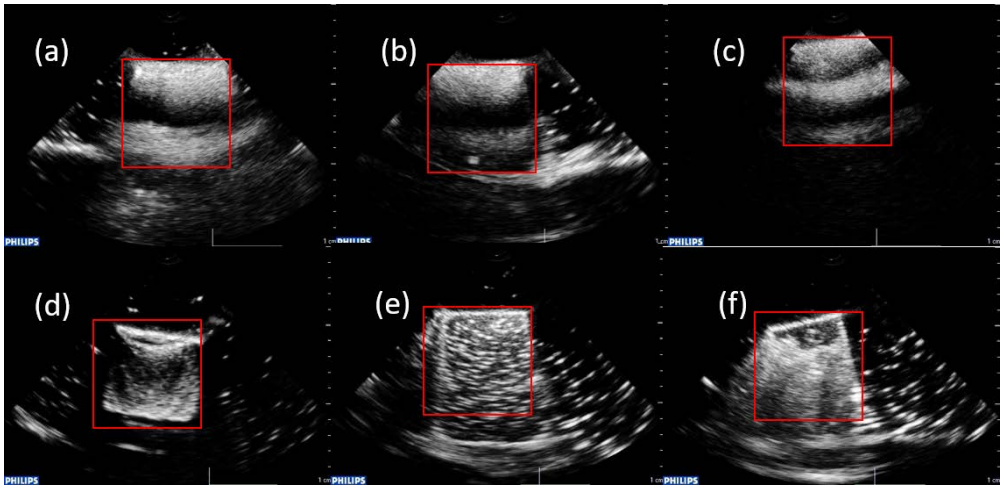

Figure 3.7. Ultrasound pixel intensity for (a) Layfomm40: 152.78 ±34.21; (b) Layfomm60: 157.33 ±36.15; (c) Gel-lay: 154.54 ±34.74; (d) Tango Plus: 58.88 ±62.29 (min); (e) silicone 0050: 124.00 ±55.03 and (f) silicone 0020: 127.05±57.7

Table 3.7-1. Ultrasound acoustic properties of different 3D printable materials

Samples	Layfomm40	Layfomm60	Gel-lay	Tango Plus
Density (kg/m^3)	1,082	1,041	1,023 (min)	1,100
Attenuation (dB/cm@1.5MHz)	6.57	5.95	6.24	29.31 (max)
Velocity (m/s@1.5MHz)	1,468	1,544	1,581	2,039 (max)
Impedance ($10^6 kg/m^2/s$)	1.59	1.61	1.62	2.24 (max)
Backscattering Coefficients (dB at 1.5 MHz)	-22.50	-20.41	-17.86	-32.60 (min)

The ultrasound acoustic values, including the velocity, attenuation and backscattering of different materials, are summarised in tables 3.7-1 and 3.7-2. For each property, the minimum and the maximum are highlighted for all the tested materials. Because Jehbco silicone has a much larger Young's modulus than other materials and soft tissue, its ultrasound properties were not tested further. It can be seen that silicone 0020, which is the most flexible material, also has the lowest attenuation of 3.52 dB/cm at 1.5 MHz, the largest mean backscattering coefficient of -15.26 dB relative to steel plate and the

lowest velocity of 1,038 m/s at 1.5 MHz. In literature, it is reported that the classic tissue-mimicking material, RTV silicone, has a velocity between 959 and 1,113 m/s and attenuation between 0.1 and 5.6 dB/cm measured in the frequency range of 500 kHz–1 MHz [102]; our results agree with these reference results. Further comparisons between these materials and real tissue were discussed in section 3.7.

Table 3.7-2. Ultrasound acoustic properties of different unprintable materials

Samples	Silicone 0050	Silicone 0020
Density (kg/m^3)	1,363 (max)	1,202
Attenuation (dB/cm at 1.5 MHz)	4.62	3.52 (min)
Velocity (m/s at1.5 MHz)	1,063	1,038 (min)
Impedance ($10^6 kg/m^2/s$)	1.45	1.25 (min)
Backscattering Coefficients (dB @ 1.5 MHz)	-18.22	-15.26 (max)

3.4 Optical Microscope Observation

The Layfomm40 material's ability to absorb other liquids makes it easily combined with other materials, which enables its compatibility to the radiofrequency ablation system—the conductivity & colour-changing effects, the corresponding functional results were presented in chapter 5 with a bi-atrial model. The aim of the optical microscope characterization is to demonstrate Layfomm40's porous structures rinsed in different liquids. The observation of its material change from microscale was carried out using Leica optical microscope (Leica Microsystems GmbH, Germany), while the

used liquids included water, saline & thermochromic solutions. The type of the thermochromic material was determined from the visual inspection and microscope observation first as shown from figure 3.8-3.10.

Thermochromic material is a type of smart material with a colour-changing effect triggered by heating or cooling. It is usually composed of a colour developer, former and co-solvent, as shown in figure 5.7. The colour developer can produce the colour-changing effect and colour intensity, while the former determines the base colour [103]. In terms of whether the original colour can be recovered, thermochromic materials can be classified as reversible and irreversible ones. The two material types employ different principles to produce the colour-changing effect, and both thermochromic pigments were purchased from Special FX Creative (SFXC, UK). As shown in figure 3.8 (a), the colour former and colour developer inside reversible thermochromic microcapsules are only reorganised under heat, making the colour-changing effect temporary. On the other hand, the volatile dye inside irreversible thermochromic microcapsules evaporated when heated to the phase transition temperature, resulting in a permanent colourless state. Figure 3.9 shows their different colour-changing effects using two 3D printed cuboid specimens and a hot lamp as the external heat source. The blue specimen in figure 3.9 (a-1 and b-1) was directly printed by a type of colour-changing PLA material, it went colourless when heated above 40℃ but once placed in cold water, it gradually recovered its original blue colour. Compared to the reversible colour-changing specimen, the irreversible specimen was printed using regular white PLA filament and coated with grey irreversible paint. The effect lasts permanently once the original colour has vanished. The colour changing procedure was also monitored under an optical microscope, with the results shown in figure 3.10; the results were consistent with those in figure 3.9. However, it could be observed that the recovered colour of the reversible thermochromic PLA specimen was lighter than the original colour, with its grid structure made crystal-like. Moreover, the irreversible specimen did not have any holes on its surface.

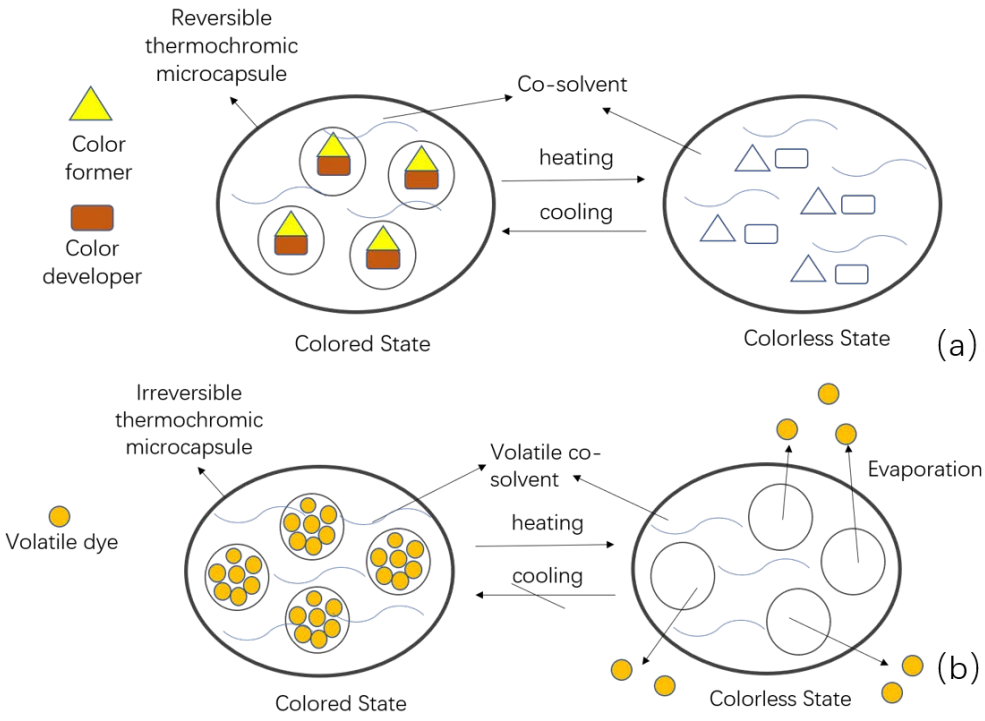

Figure 3.8. Composite changing procedures of (a) reversible and (b) irreversible thermochromic materials during heating and cooling: (a) in reversible thermochromic microcapsules, the colour former and colour developer are reorganised under heat; (b) in irreversible thermochromic microcapsules, the volatile dye is evaporated during heating

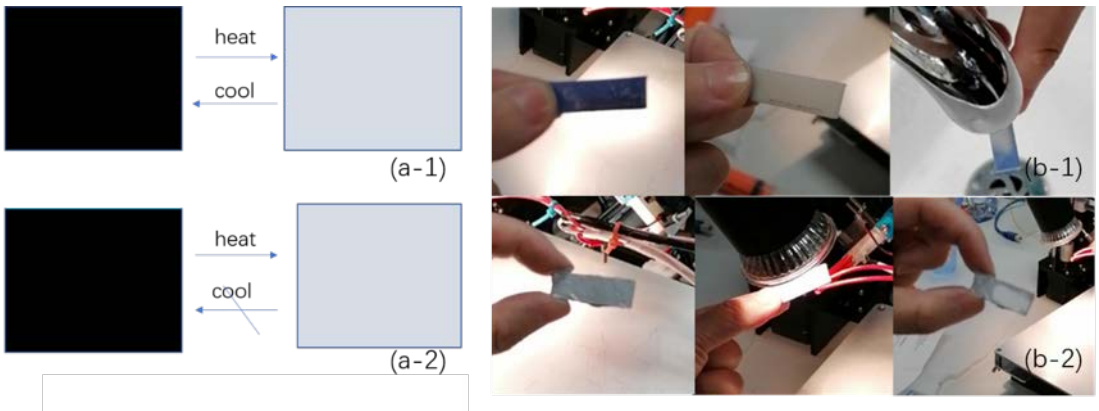

Figure 3.9. Comparison of (a-1 and b-1) reversible and (a-2 and b-2) irreversible thermochromic paintings; (b) demonstration on 3D printed PLA cuboid specimens: the reversible blue PLA specimen's colour recovers after rinsing in cold water, while the irreversible grey PLA specimen remains colourless even without heat source

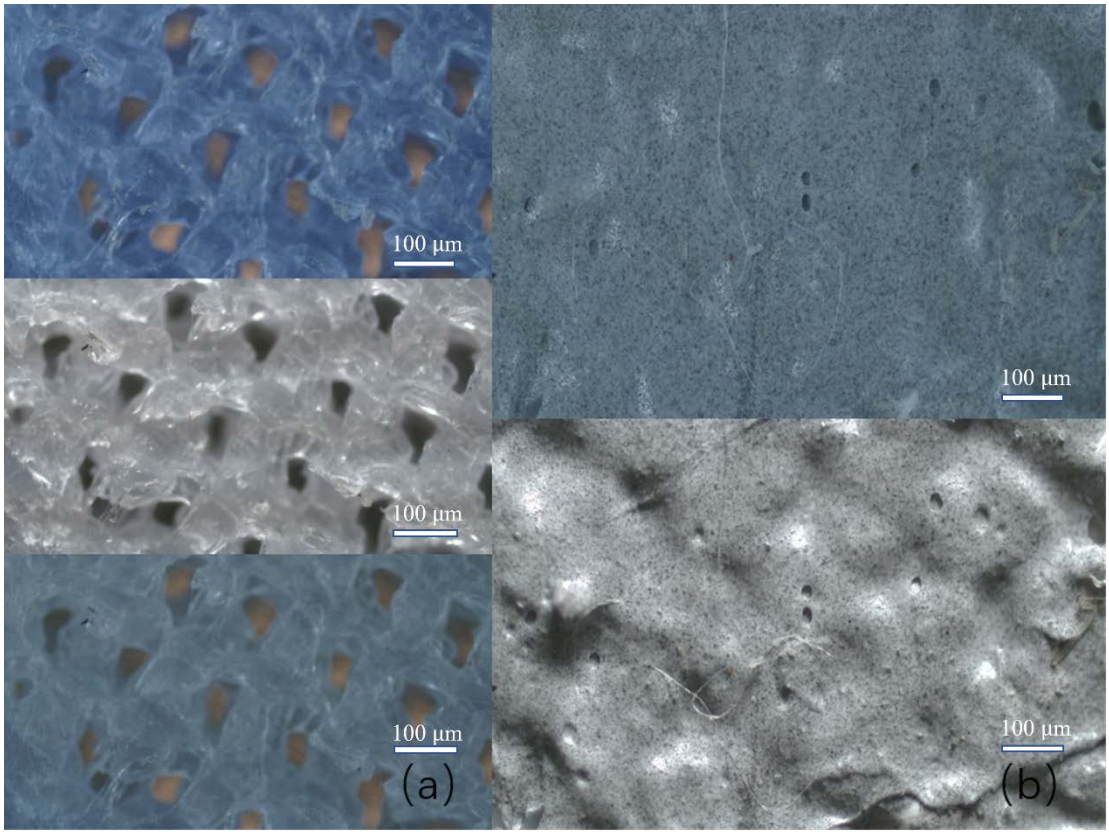

Figure 3.10. Optical microscope comparison of (a) reversible and (b) irreversible thermochromic PLA specimens: the recovered colour of (a) is lighter than its original colour, while (b) remains colourless state after heating.

Based on the requirements of the ablation experiments in chapter 5, the ablated mark should last permanently for postoperative visualization, thus, the irreversible thermochromic pigment was chosen as the bi-atrial model's coating, and the absorption of the thermochromic solution of Layfomm40 material was compared to the absorption of water and saline solution at the same time using Leica optical microscope (Leica Microsystems, Germany) in figure 3.11 (a).

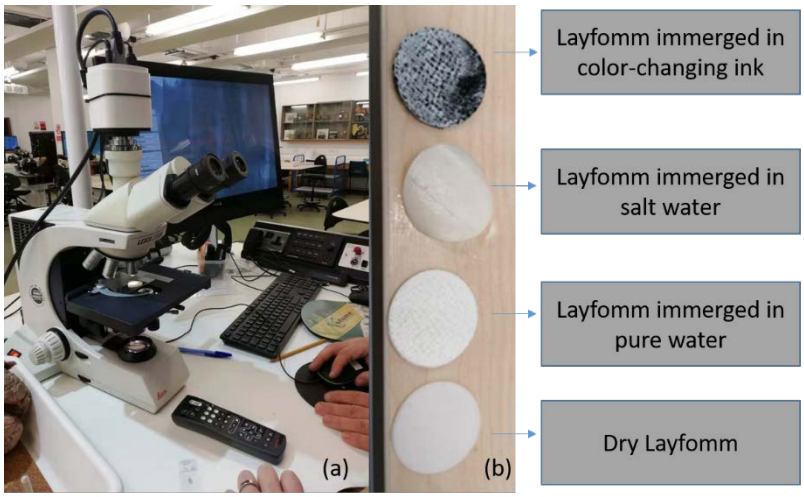

Figure 3.11. (a) Leica optical microscope (Leica Microsystems, Germany); (b) four printed Layfomm40 samples: samples immersed in colour-changing ink, saline water and water, and dry Layfomm40

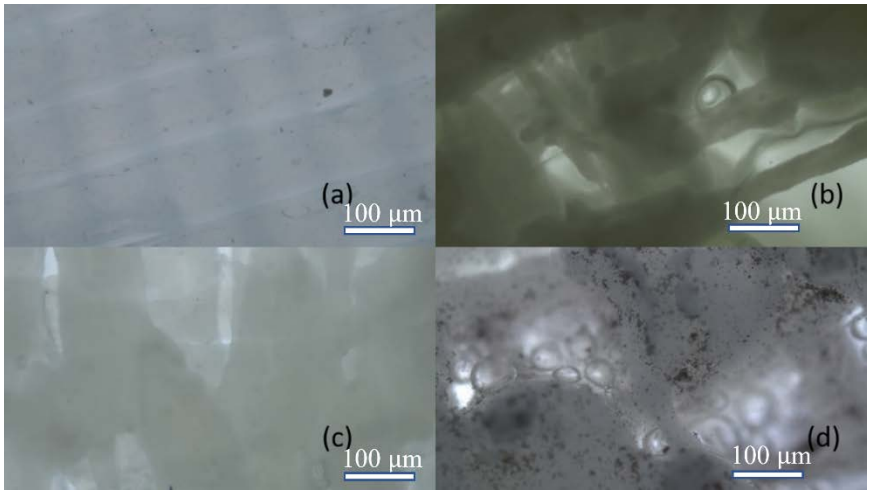

Figure 3.12. Optical microscope images of (a) dry Layfomm40, (b) Layfomm40 immersed in pure water, (c) Layfomm40 immersed in saturated salt water and (d) Layfomm40 immersed in thermochromic ink

As shown in figure 3.11 (b), the Layfomm40 specimens were prepared as circular discs (2 cm diameter) in dry condition, or immersed in water, saline and irreversible thermochromic solution. Figure 3.12 shows the corresponding microscope images of the four samples. The dry Layfomm40 initially appeared as a fibrous material with a flat surface. After absorbing water (figure 3.12 (b)), the porous structure appeared,

allowing water to flow inside. Aside from resembling figure 3.12 (b), the saline water-immersed sample in figure 3.12 (c) became conductive, and the quantitative conductivity shall be characterised in the next section 3.5. Figure 3.12 (d) demonstrates that the irreversible thermochromic pigments could float inside Layfomm40 along with the air bubbles and water.

3.5 Thermal & Electrical Conductivity Testing

In addition to being irreversibly thermochromic and flexible, the material must be both thermally and electrically conductive to make the atrial ablation simulator compatible with the RFA system. The previous microscope images have proven the Layfomm40's ability of absorbing saline water, and the quantitative conductivity characterisations were performed using the following setup in figure 3.13 in terms of both electrical & thermal conductivity.

Electrical conductivity is a concept used to quantify a material's ability to transfer electric current, a high value of electrical conductivity indicates a high ability of current conduction and low impedance [10]. The electrical conductivity testing was completed using a multimeter, as shown in figure 3.13 (a). The prepared specimens were 3D printed 10mm*10mm*10mm cubes using the chosen four printable materials in table 3.8. The result could be calculated via equation: $\rho = \frac{R \times A}{L}$; $\sigma = \frac{1}{\rho}$, where ρ denotes electrical volume resistivity, R denotes resistance, A denotes the specimen area, L denotes the specimen length and σ is the calculated electrical conductivity. As listed in table 3.8, the conductive PLA from Proto-Pasta, Amelon and Graphene have an electrical conductivity of 0.058, 0.007, and 0.017 Siemens/metre (S/m) respectively, while saline water-immersed Layfomm40 has a comparatively small electrical

conductivity of 3.0×10^{-6} S/m, but the rigidity of these conductive PLA filaments limits their ability to mimic cardiac tissue.

Thermal conductivity is used to measure a material's heat-conducting ability. Materials with high thermal conductivity have a strong ability to transfer heat [10]. The thermal conductivity experiment was conducted using the KD2 Pro thermal analyser (ICT International, Australia), as shown in figure 3.13 (c), which was specifically used to test the thermal conductivity of rubber-like materials. The samples were 100 mm long, measured 15 mm around the needle probe and had a 2.4 mm inner hole. The tests were performed using samples of varying densities immersed in saturated saline water; however, these did not yield different results. The thermal conductivity could then be calculated using equation: $q = -\kappa \cdot \frac{T_2 - T_1}{L}$, where q denotes the heat flow, κ denotes the thermal conductivity, $T_2 - T_1$ is the temperature difference and L is the heat flow's travel distance. The thermal conductivity of the rigid plastic materials could not be tested using this thermal property analyser.

Table 3.8. Electrical and thermal conductivity comparison of different conductive 3D printable materials & cardiac tissue

Material	Conductive PLA – Proto-Pasta	Conductive PLA – Amelon	Graphene	Lay-fomm40	Cardiac Tissue
Electrical Conductivity σ (S/m)	0.058	0.007	0.017	3×10^{-6}	0.16[104]
Thermal Conductivity κ(W/m/K)	-	-	-	0.40	0.56[23]

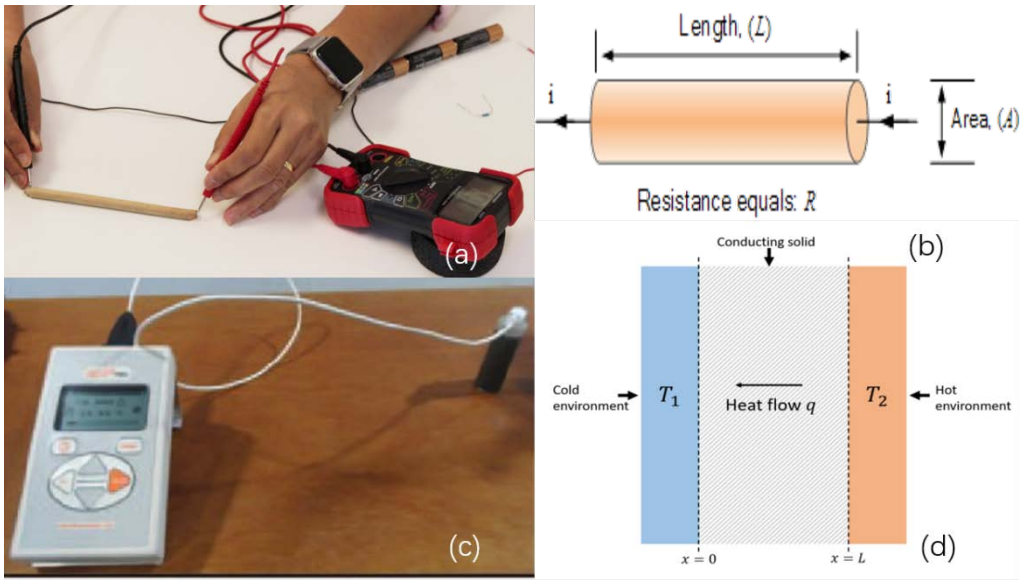

Figure 3.13. (a & b) Electrical conductivity testing and calculation using a multimeter; (c & d) thermal conductivity testing and calculation using KD2 pro thermal analyser

3.6 Rheological Characterisation

The commercial silicone materials are generally not 3D printable due to their low viscosities. The modification method used here is adding certain amount of fumed silica powder, thus, direct silicone printing technique could be then applied to make the aortic valve model in chapter 6. The relevant rheological characterisations of modified silicone inks are described in this section.

Complex viscosity [105] measures the total resistance to the flow of a fluid and plays an important role in a material's printability, it can influence the extrusion's morphology (figure 3.14). Suitable viscosity is crucial for extruding a smooth strand for 3D printing. Low viscosity generally causes the failure of the material to form a filament and stay on the printer bed, whereas high viscosity is more likely to result in an inconsistent flow from the nozzle, or even jamming. Hence, attaining the perfect printability of inks involves finding trade-offs and a suitable viscosity. Experimentally, kinematic viscosity can be measured by viscometer or rheometer, and the rheological characterisation

results are important for choosing the correct type of silicone as well as a suitable printing temperature. While rheological parameters already exist for commercial RTV silicone in current research, numerical analysis on how fumed silica affects silicone printing and the printed flexibility remains unknown.

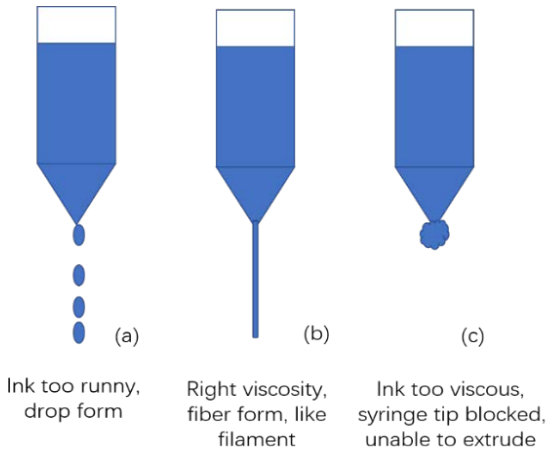

Figure 3.14: Illustration of the effect of different ink viscosities: runny inks will cause the failure of the material to form a filament, inks with proper viscosities can shape the material into filament form while very viscous inks will block the extruder tip

Figure 3.15: Experimental setup for silicone materials' rheological characterisation: (a) two-part Dragonskin 10 RTV silicone (Bentley Advanced Materials, UK); (b) used hydrophobic fumed silica powder; (c) Anton-Paar MCR92 rheometer, test in progress

The rheological experiments consisted of two-time sweep tests, one for different

temperatures and the other for different amounts of fumed silica inside the prepared silicone inks. To compare temperatures, the material sample was made of Dragonskin 10 silicone (Smooth-on, USA), shown in figure 3.15 (a), and fumed silica powder (figure 3.15 (b)). The amount of silica powder was fixed at 10% v/v, and the temperature range was 40–80 ℃. To compare the amounts of fumed silica, the temperature was fixed at 60℃, and the amount of silica powder was 0–20% v/v. Both experiments were completed using an Anton-Paar MCR92 rheometer (Anton Paar, USA), shown in figure 3.15 (c), in oscillation mode (a rheological testing mode to investigate phase transitions and crystallisations during a curing process, can be used to determine both viscous and elastic properties of the materials) on a 40 mm diameter steel plate peltier. The exported data was analysed with Origin 2020 (OriginLab, USA), which is an all- in-one software to handle tasks such as signal processing, data manipulation, graphing and reports.

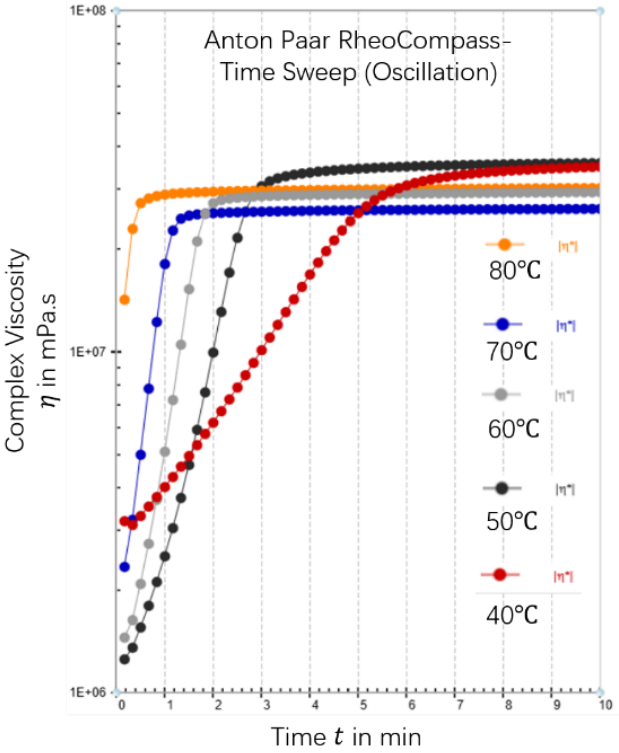

Figure 3.16: Time sweep experiments of Dragonskin 10 silicone +10% fumed silica (v/v percent) at different temperatures (40–80 ℃)

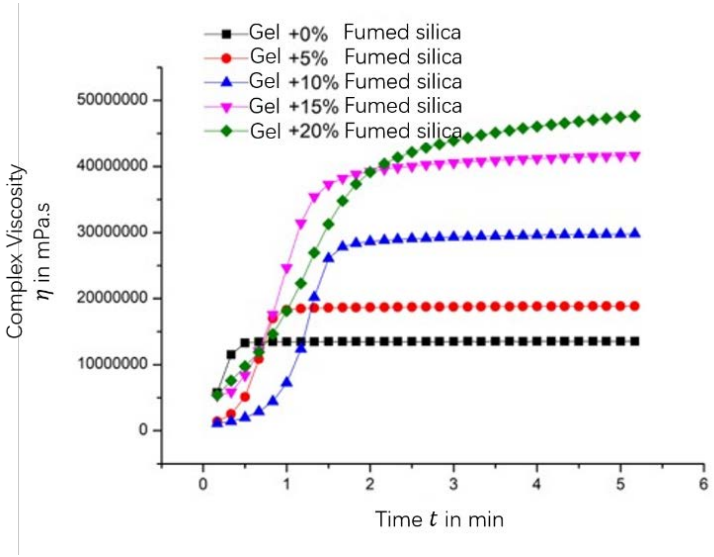

Figure 3.17: Time sweep experiments of Dragonskin 10 silicone at 60 ℃ with different amounts of fumed silica (0–20% v/v)

Figure 3.16 shows the complex viscosities of Dragonskin 10 silicone with 10% fumed silica along different temperatures from 40℃ to 80℃, the inks' viscosities increase from 10^6 mPa.s to 10^7 mPa.s within 0.5-5 mins. While figure 3.17 shows the complex viscosities of Dragonskin 10 silicone at fixed temperature 60℃ along different fumed silica amount from 0% to 20%, the lowest finale viscosity is around 1.5×10^7 mPa.s and the highest finale viscosity is around 4.5×10^7 mPa.s.

3.7 Discussion

3.7.1 Analysis of Mechanical Characterisation Results

3.7.1.1 Mechanical analysis of phantom materials

From the mechanical testing results presented in Table 3.1-1 & 3.1-2, it can be seen that amongst all the selected materials, silicone 0020 is the most elastic, while Jehbco

silicone is the stiffest. Moreover, the myocardium's Young's modulus reported in [16] is between 0.18 and 0.28 MPa (equivalent to 180-280 kPa). As a 3D printable material, Layfomm40 has the closest Young's modulus value (128.5 kPa) to real myocardium with a difference of 28.6%–54%, while the Young's modulus values of the other three 3D printable materials are much larger than the myocardium's one: Layfomm60 & Tango Plus: 2-3 times, Gel-Lay: 5-8 times of myocardium's Young's modulus. Meanwhile, Layfomm40's hardness (4 HA) can achieve the same level as the classic tissue-mimicking material silicone Ecoflex-0050 (5HA) at its maximum flexibility after rinsing. A conclusion can be drawn that among all 3D printable materials, Layfomm40 is the best choice to mimic cardiac tissue in terms of flexibility (both Young's modulus and hardness).

However, Layfomm40 could not be used to make the dynamic valve model, thus, a more durable material type--silicone was investigated. From the hardness and Young's modulus data presented in table 3.3, when compared to the arcus aorta's hardness reported in [17], which is Shore A 13.4±1.9, Dragonskin 10 silicone has the closest value of Shore A 9.5 among the listed materials, with a difference of 29.10% compared to biological tissue, therefore, it was selected to make the aorta phantom in chapter 6 using the two-part moulding technique. While Ecoflex 0030 was chosen as the valve materials with a Young's modulus difference of 11.29% when compared to the value of real valvular leaflets' tissue (62 kPa) reported in [18].

The use of fumed silica powder could change the unprintable commercial silicones to printable ones, with certain increases in materials' hardness and Young's modulus values presented in table 3.4-1 & 3.4-2, however, there is no quantitative relationship between the increase in flexibility and the amount of silica. With a broader range of ink flexibility, the silicone printing technique can be used in more applications, while the most suitable printing option depends on the application requirement.

3.7.1.2 Mechanical analysis of moulding materials

The moulding materials' mechanical performances were also analysed as they shall affect the phantom fabrication procedure when moulding technique applied. Separate water solubility test was performed first, from table 3.5-1, it can be observed that PVA is the dissolves the most easily, while High-T-Lay is the most difficult, and the dissolving time increases non-linearly with the tested infill densities. While table 3.5-2 shows that high temperatures could accelerate the moulding materials' dissolving.

Regarding to the strength analysis from table 3.6-1 & 3.6-2, PVA has the smallest average flexural modulus with 242 MPa and Lay-PVA has the largest with 1,412 MPa, which means PVA is the best option in terms of flexible moulding materials, and Lay-PVA is the strongest. With a lower infill density, the mould becomes very fragile while high infill density makes the mould hard to dissolve. Thus, the final printing option for the internal moulding material was PVA with 40% infill density.

3.7.2 Analysis of Ultrasound Acoustic Properties

From the ultrasound images in figure 3.7, it can be observed that the low pixel intensity of Tango Plus sample means that it could result in corresponding low-quality ultrasound images, while the Poro-Lay & silicone materials are more ultrasound compatible. This finding is also consistent with the quantitative ultrasound acoustic measurements.

The velocity of real tissue is reported to be around 1500 m/s in [106], while the attenuation and acoustic impedance of real cardiac tissue are 0.5 dB/cm and $1.67 \times 10^6 \frac{kg}{m^2}/s$, respectively, at 1 MHz [19]. According to the linear dependency of attenuation on frequency, the estimated attenuation of real cardiac tissue is 0.75 dB/cm at 1.5 MHz. A comparison between the real tissue and the new materials is summarised

in table 3.9-1 and 3.9-2, where the relative difference is calculated by the absolute difference dividing the value of the cardiac tissue.

Table 3.9-1. Ultrasound acoustic value differences between different 3D printable materials and real tissue

Samples	Layfomm40	Layfomm60	Gel-lay	Tango Plus
Attenuation Difference (@1.5MHz)	776%	693%	732%	3,808% (max)
Impedance Difference	4.79%	3.59%	2.99% (min)	34.13% (max)
Velocity Difference (m/s)	32 (min)	44	81	809 (max)

Table 3.9-2. Ultrasound acoustic value differences between different unprintable materials and real tissue

Samples	Silicone 0050	Silicone 0020
Attenuation Difference (@ 1.5 MHz)	516%	303% (min)
Impedance Difference	13.17%	25.15%
Velocity Difference (m/s)	437	462

From the calculated differences listed in table 3.9-1 & 3.9-2, it is clear that all the silicones and rinsed Poro-Lay series materials have significantly less difference to myocardium [106,19] than Tango Plus: Tango Plus has the largest attenuation (3808%), impedance (34.13%) and velocity differences (809 m/s) compared to real tissue, while silicone 0020 has the smallest attenuation difference of 303%, Gel-Lay has the smallest impedance difference of 2.99% and Layfomm40 has the smallest velocity difference of 32 m/s. However, the ultrasound properties' difference between the materials within Poro-Lay series are quite small, which means the Poro-Lay materials are good ultrasound materials.

Combined with the mechanical results that Layfomm40 has the highest flexibility among all the 3D printable materials, it was chosen out of all the 3D printable materials to make the ultrasound compatible cardiac phantom, while Tango Plus was chosen for better printing quality and easy stable storage.

3.7.3 Analysis of Optical Microscope Images & Conductivity of Layfomm40

The results in figure 3.9 (b-2) & figure 3.10 (b) demonstrate the irreversible thermochromic coating's permanent colour-changing effect after heating. In the further microscope images figure 3.12 (d), the thermochromic solution could also be absorbed inside Layfomm40 just like water and saline, however, the pigment was easily washed away when the Layfomm40 model was placed in a water tank. Thus, instead of immersing the model in ink, pigments were mixed with acrylic paint and brushed on its surface in the subsequent atrium simulator design in chapter 5. The microscope observation results of the rinsed Layfomm40 are consistent with its formula description: the PVA component of Layfomm40 will dissolve inside water/other mixed liquids, and the TPU component will keep its shape with micro holes generated in the

polymer structures. These micro holes could be potentially used for cell growing, which is an interesting topic in the future work.

From the results presented in table 3.8, even though the electrical conductivity of Layfomm40 (3.0×10^{-6} S/m) is much lower than cardiac tissue's (0.16 S/m [104]) and other rigid conductive 3D printable materials' (0.007-0.058 S/m), it is still much higher than the value of the traditional soft tissue-mimicking material, silicone rubber, which is only 5.16×10^{-12} S/m [21], and the small conductivity of saline water rinsed Layfomm40 was enough for initiating the RFA device in later functional testing described in chapter 5. However, the thermal conductivity of Layfomm40 is 0.4 W/m/K, which is comparable to the value of cardiac tissue (0.56 W/m/K [23]), with a difference of 28.57%.

From the current analysis, there is no commercial 3D printable materials with both good thermal and electrical conductivities comparable to real cardiac tissue at the same time, let alone other properties like flexibility. The results show that the saline water rinsed Layfomm40 is more ideal than silicone rubber or other rigid conductive filaments to make the RFA simulator in chapter 5. This is not only because of its good flexibility and ultrasound acoustic property as demonstrated from mechanical and ultrasound acoustic characterisations, but also because of its ability to simultaneously transfer heat and electrical current, which is essential for the RFA system to work and leave a mark on the surface where ablated.

3.7.4 Rheological Analysis of Modified Silicone Inks for Silicone Printing

From the rheological characterisation of the modified silicone inks, figure 3.16 shows that as temperature increases, the complex viscosity η of the ink increases and reaches a plateau faster. For example, it takes more than five minutes for the silicone material

to cure at 40 ℃, but only 30 seconds at 80 ℃. However, there is no obvious correlation between the plateau complex viscosity and the temperature because ink molecules move faster and collide with each other more frequently, accelerating the crosslinking process. Figure 3.17 demonstrates that the addition of fumed silica increased the complex viscosity of the crosslinked Dragonskin 10 silicone, and as the concentration of the silica increased, the plateau complex viscosity of the silicone increased. Meanwhile, the increase in fumed silica addition also increased the crosslinking time of the silicone gel, from around 30 seconds for Dragonskin 10 silicone to around two minutes for 20% silica-added silicone. One explanation for this is that the curing process is determined more by the temperature and the reaction of the crosslinker and catalyst after mixing, whereas the powder can only increase the original and cured viscosity without changing the chemical reaction.

From the previous two rheological tests, it can be concluded that both high temperature and suitable amount of fumed silica are necessary to make the silicone ink printable, during the later printing test, the chosen ink was prepared with Dragonskin 10 silicone with 20% fumed silica powder addition, and the temperature of the heating system was set to 80℃, in cases where higher viscosities or hardness were desired, the fumed silica can be added up to 60% depending on the chosen silicone base materials.

3.8 Conclusion and Relation to Following Chapters

The different characterisations described in chapter 3 help the selection of proper soft materials for different cardiac models' fabrication:

Based on the flexibility and ultrasound acoustic characterisation results, Layfomm40 was chosen because of its close Young's modulus value and ultrasound compatibility to myocardium, while Tango Plus was chosen for better printing quality and easy stable storage to make the whole ultrasound cardiac phantoms developed in chapter 4. Based

on the optical microscope observations and conductivity results, saline water rinsed Layfomm40 material coated with irreversible thermochromic painting was chosen to make the bi-atrial model for RF ablation and CARTO3 mapping in chapter 5. Based on the high durability and flexibility, silicone materials were chosen to make the aorta & valve models (Dragonskin 10 has a close Shore A hardness to aorta and Ecoflex 0030 has a close Young's modulus value to valvular leaflets), PVA was selected as the moulding materials when two-part moulding technique was applied, while silicone inks mixed with fumed silica powder were chosen to make another valve model when silicone printing technique was applied in chapter 6, the relevant rheological characterisation results help find suitable silicone printing parameters.

4. DEVELOPMENT OF A CARDIAC PHANTOM FOR MULTIMODAL IMAGING AND INTERVENTIONAL PROCEDURES

The aim of this chapter is to use direct 3D printing technique to make the whole cardiac phantom for interventional procedures and multimodal medical imaging, particularly ultrasound imaging. The patient-specific phantom needs to be easy to manufacture, customisable and inexpensive. Based on the previous mechanical and ultrasound acoustic property characterization results, the following work demonstrates the fabrication of ultrasound-compatible cardiac phantoms with novel 3D printable materials—Layfomm40 & Tango Plus, and the work presented in in this chapter can be found in the journal publication:

Wang, S., Noh, Y., Brown, J., Roujol, S., Li, Y., Wang, S., Housden, R., Ester, M. C., Al-Hamadani, M., Rajani, R., & Rhode, K. (2020, December). Development and testing of an ultrasound-compatible cardiac phantom for interventional procedure simulation using direct three-dimensional printing. *3D Printing and Additive Manufacturing*, 269–278. https://doi.org/10.1089/3dp.2019.0097

4.1 Introduction to 3D Printed Cardiac Phantom

Early evaluation of CVD can be carried out using models or phantoms of the cardiovascular system and reduce the dependency on animal, cadaveric or human studies [107]. The development of high-fidelity anthropomorphic cardiac phantoms is an area of current research. While the literatures summarized in section 2.1 presents several ultrasound materials to be used for soft tissue-mimicking phantom fabrication

and 3D printed cardiac models, a full-chamber ultrasound compatible cardiac phantom directly made by 3D printing has not been reported.

The work described in this chapter is the production of complete cardiac phantoms with four main chambers for multimodal medical imaging, particularly ultrasound, and interventional procedures, using the techniques of 3D printing with soft materials (including Layfomm40 & Tango Plus). Both phantoms' fabrication procedure are easy and inexpensive. 3D printing technology is investigated through both a high-end PolyJet printer, using Tango Plus material (Stratasys Objet500, Israel), and a commonly used FDM printer (WASP Delta 2040, Italy), using Poro-Lay materials (Kai Parthy, Germany). Both materials' mechanical and ultrasound acoustic properties were characterised in chapter 3 as they need to be taken into consideration before printing. Results are presented including visual inspection, qualitative comparison of echocardiography, fluoroscopy, CT, and MRI images during cardiac interventional simulation.

4.2 Development of Patient-specific Cardiac Phantoms Using 3D Printing

4.2.1 3D Cardiac Model Segmentation

After comparing the materials' stiffness, hardness, and ultrasound acoustic properties in chapter 3, Layfomm40 can be regarded as the best tissue-mimicking 3D printable material. However, it must be immersed in water for a long time to keep its maximum flexibility, while Tango Plus is more stable and easier to store. The overall procedure for fabricating an ultrasound cardiac phantom is summarised in figure 4.1.

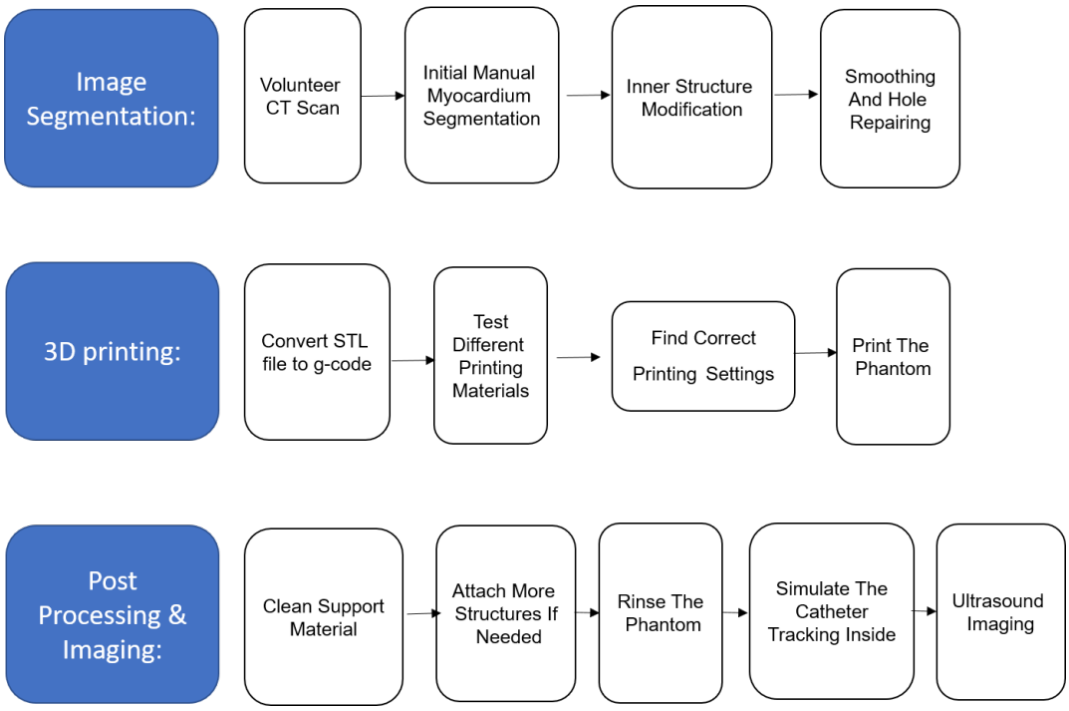

Figure 4.1. Overall procedure for ultrasound cardiac phantom fabrication using 3D printing technique.

Before printing, the cardiac model should first be segmented from volumetric medical images. In this paper, the original images were obtained from a chest CT scan (519 slices) of a healthy male volunteer. They were then segmented semi-automatically using ITK-Snap (University of Pennsylvania & Utah, USA). The segmentation includes the structures of the left ventricle (LV), right ventricle (RV), left atrium (LA), right atrium (RA), mitral valve (MV), aorta (AO), superior vena cava (SVC), inferior vena cava (IVC) and the spine. As shown in figure 4.2, the red label is the myocardium, which needs to be printed, while the yellow, green and brown labels are the venae cavae, pulmonary artery and spine, respectively.

After post processing the exported red and brown labels, a 3D surface model was obtained, as shown in figure 4.2 (d). After a rough segmentation, the 3D software, Seg3D, was used to smooth the original segmentation and fix the holes inside. This was done by applying a median filter with a smoothing value of 4. Finally, to simplify the removal of the support material, the whole model was cut in half using Netfabb,

to be glued together with super glue after 3D printing. The final segmentation results used for 3D printing are shown in figure 4.3 where both the outside and inside of the 3D heart model could be clearly visualised. Using the inner slice view, the internal cardiac structures are verified to be accurate representation of patient's heart.

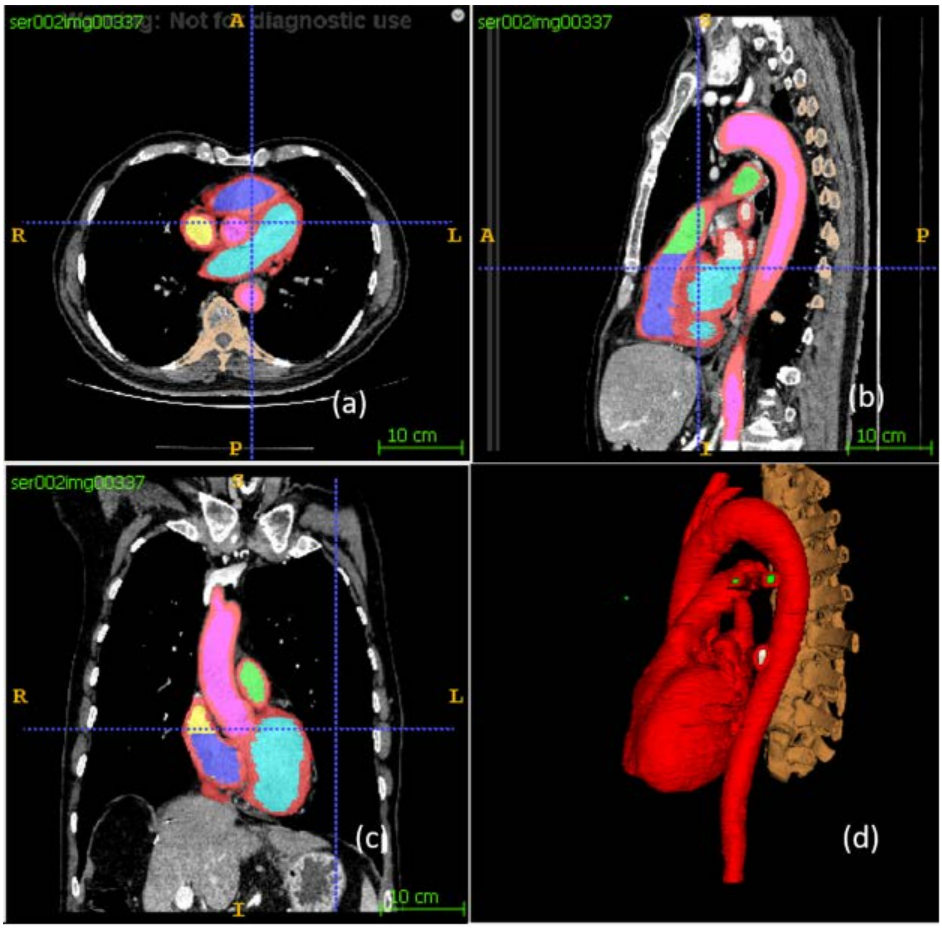

Figure 4.2. Original cardiac and spine segmentation of CT scan using ITK-SNAP with different colours representing different areas: axial view (a), sagittal view (b), coronal view (c) and 3D view (d)

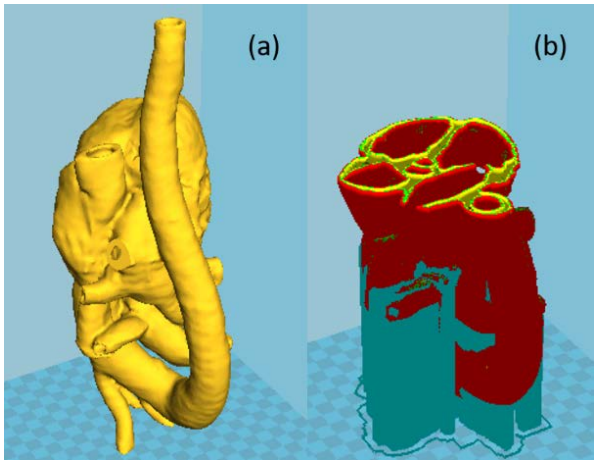

Figure 4.3. Post-processed segmented cardiac model: outside view (a) and inner slice view (b)

4.2.2 3D Printing

As previously mentioned, Tango Plus was chosen for its better stability and Layfomm40 was selected for its high flexibility and low ultrasound attenuation amongst all the 3D printable materials. Before sending the model to a printer, the 3D objects should first be converted to g-code in Cura. As shown in figure 4.4, a PolyJet Objet500 printer was used for Tango Plus, while an FDM-based WASP Delta 2040 (WASP, Italy) printer was used for Poro-Lay. Compared with general rigid filaments, Layfomm40 has stricter printing settings. The printing speed should be less than 40 mm/s, and the temperature set to 225 ℃ in order to prevent nozzle clogging. For better printing quality, the filament should be dried in a filament drier before printing. The general steps for printing with Tango Plus are similar, except that the material is prepared in the form of gel instead of a filament spool. To remove the support materials, the Tango Plus phantom was immersed in 5% soda water for two hours, while the Layfomm40 phantom's support material was manually removed with tools. After printing, Tango Plus can be stored in air without any post processing, while Layfomm40 should be rinsed in water for two days to reach its maximum flexibility.

Figure 4.4. 3D Printing: Layfomm40 (a) used by the WASP Delta 2040 printer (b) and Tango Plus (c) printed on a PolyJet Objet500 printer (d)

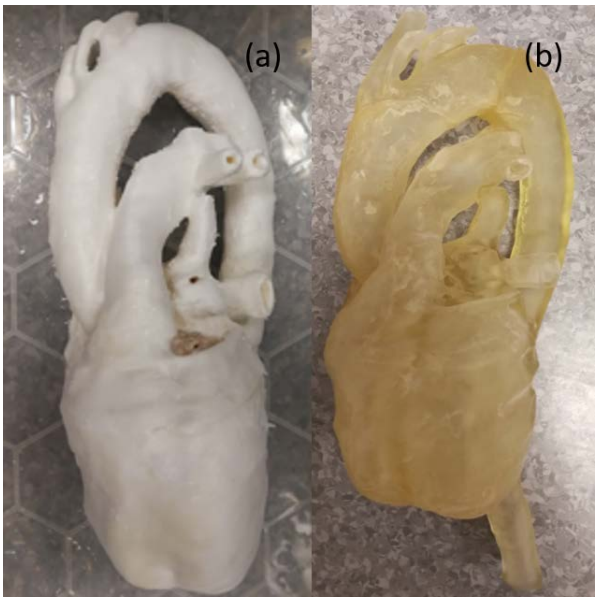

Figure 4.5. Printed whole cardiac phantoms: Layfomm40 (a) and Tango Plus (b)

The printing results are shown in figure 4.5. The size of the printed cardiac phantom is 29.98x14.52x11.26 cm^3, which is approximately the same size as a normal human heart. The printing and material costs for the Layfomm40 and Tango Plus phantoms were

GBP 68.70 and GBP 521.24, respectively. In terms of printing requirements, Tango Plus requires a high-end PolyJet printer because it is liquid gel, not a normal filament spool, thus making it less affordable. However, once printing begins, Tango Plus is much easier to control due to its lower melting point. With Layfomm40, which can be printed with any inexpensive desktop FDM printer, printing might result in failure due to its higher melting point and stickiness.

4.3 Multimodal Imaging Validation of Cardiac Phantoms

After preparing the two cardiac phantoms, the multimodal imaging experiments were conducted using 2D echocardiography, X-Ray and 3D CT and 3D MRI imaging systems. The results from the two materials, Tango Plus and Layfomm40, were compared. Since the appearance of both materials differs significantly from real myocardium, a comparison with patient data was not considered.

4.3.1 Ultrasound Imaging Validation

The 2D ultrasound images were acquired through an iE33 ultrasound machine (Philips, Netherlands) with a 2D matrix phased array x3-1 transducer (Philips, Netherlands) under a TOE transgastric basal short-axis view, during which an ablation catheter was inserted into the right ventricle of the phantom. During the experiment, the phantoms were stuck to the bottom of a box filled with water. During image collection, the most difficult problem was adjusting the probe’s location to find suitable standard views that present both the catheter and cardiac structure in the best way.

Figure 4.6 shows the 2D echocardiography results of the two cardiac phantoms. The ablation catheter appears as a bright spot labelled with a red circle. The ultrasound results indicate that both Layfomm40 and Tango Plus are suitable tissue-mimicking

materials for ultrasound phantoms because they both present clear cardiac inner structures from non-contact imaging. By comparing the two phantoms, it can be seen from figure 4.6 that the echocardiography of the Layfomm40 phantom has better ultrasound image quality with less reflection and fewer artefacts on the phantom surface. Moreover, Layfomm40's speckle size is smaller than that of Tango Plus and closer to real myocardium's appearance. The catheter tip (red circle) inside both phantoms is very distinct and easy to identify, which demonstrates the plausibility of building up future TOE datasets using the phantoms.

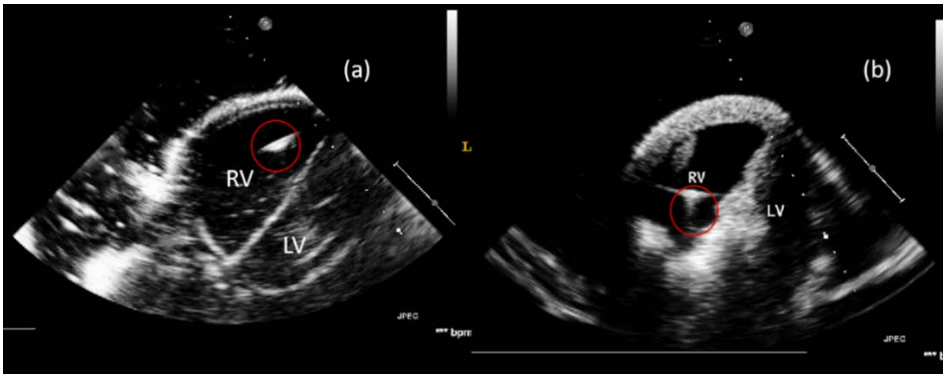

Figure 4.6. 2D Echocardiography with the catheter (red circle) in the right ventricle (RV): Layfomm40 phantom (a) and Tango Plus phantom (b)

4.3.2 X-Ray and CT Imaging Validation

The X-Ray and cone beam CT scans were acquired using Siemens Axiom Artis C-arm system (Siemens, Germany). From the initial water-based experimental results, both Layfomm40 and Tango Plus show a similar Hounsfield Unit (HU) to water in X-Ray and CT images. Therefore, the final images were acquired in air for a higher phantom-background contrast of both the heart and the catheter. To distinguish the two phantoms during post analysis, a CS catheter was inserted through the inferior vena cava into the right ventricle of the Tango Plus phantom and through the aorta into the left ventricle of the Layfomm40 phantom. Figures 4.7 and 4.8 show the X-Ray and CT images of both phantoms. The X-Ray and CT show no obvious difference between Tango Plus

and Layfomm40 in terms of X-ray contrast or CT number, measured on the Hounsfield Scale and close to 0 for both phantoms, i.e., similar to water. Compared to the echocardiography results, the catheter tip under fluoroscopy can be tracked and reconstructed more easily, but the cardiac inner structures, especially the valves, are difficult to see in X-Ray. The latter are better visualised using CT.

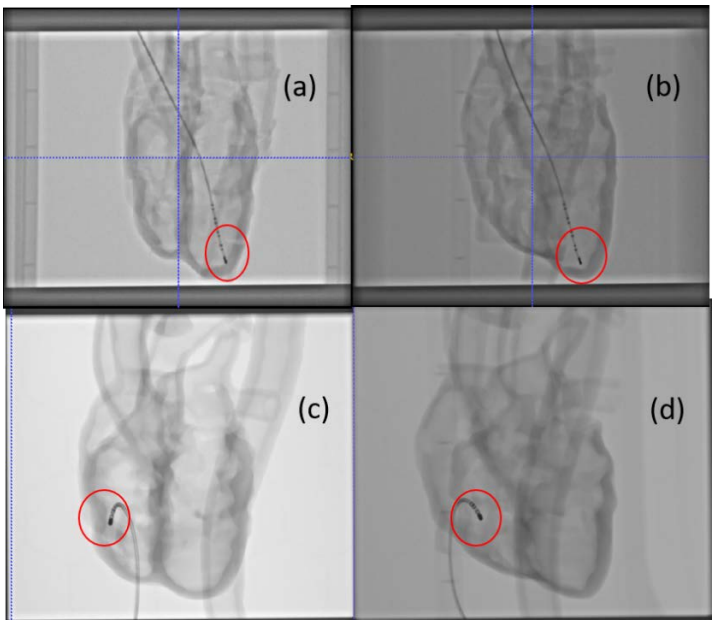

Figure 4.7. X-Ray images of the Layfomm40 (a and b) and Tango Plus (c and d) phantoms showing the front and side views, with ablation catheters inside the left and right ventricles, respectively

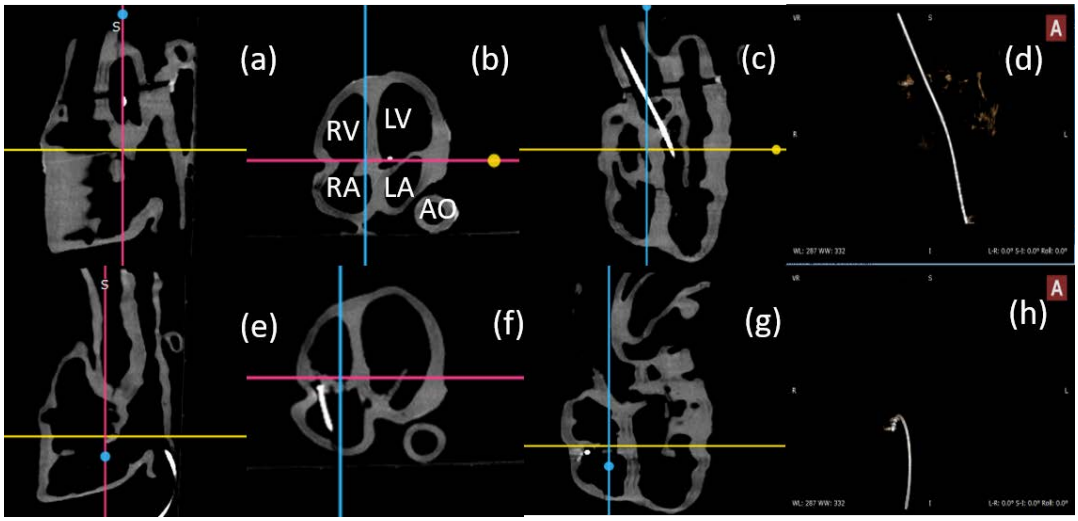

Figure 4.8. CT images from x, y, z views and the corresponding reconstructed ablation catheters. Layfomm40 (a–d) and Tango Plus (e–h) phantoms

4.3.3 MRI Imaging Validation

The MRI scanner used was a Siemens Magnetom Aera 1.5T (Siemens, Germany). Due to safety considerations of the strong magnetic field of the environment, no catheter could be inserted into the phantoms.

During imaging, both phantoms were placed in a plastic water tank under four classical MRI imaging modes: T1-weighted, T1-mapping, T2-weighted and T2-mapping. The whole procedure lasted approximately one hour in order to ensure image quality because longer MRI imaging times can guarantee higher resolutions. 3D T1-weighted and T2-weighted data were acquired using a fast spin echo sequence (voxel size = 1.3×1.3×1.3 mm^3). Single-slice T1- and T2- mapping were carried out using the modified look-locker inversion recovery sequence (5-(3)-3 MOLLI scheme [108]) and a T2-prepared based sequence, using a balanced steady state free precession (bSSFP) readout [109] (voxel size = 1.4×2.1×8 mm^3) for both.

Figures 4.9 and 4.10 show the MRI images of the two phantoms without catheters. From the T1 MRI imaging results, the Layfomm40 phantom have a higher contrast with the water background than the Tango Plus phantom, which is closer to real tissue, however, in T2 mode, the difference between the two phantoms is not as obvious as in T1 mode. The image contrast of the Layfomm40 phantom is 80%, while that of Tango Plus is -57% relative to water in T1 mode. The image contrast of Layfomm40 is -90%, while that of Tango Plus is -96% relative to water in the T2 mode.

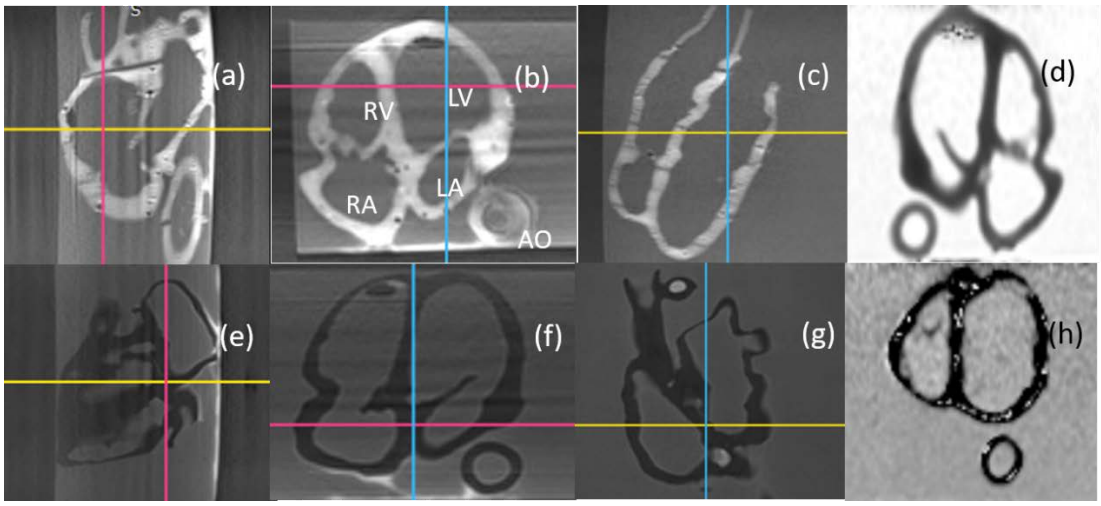

Figure 4.9. MRI images from multiplanar orthogonal views in T1-weighted and T1-mapping modes. T1-weighted: Layfomm40 phantom (a–c) and Tango Plus phantom (e–g); T1-mapping: Layfomm40 phantom (d) and Tango Plus phantom (h)

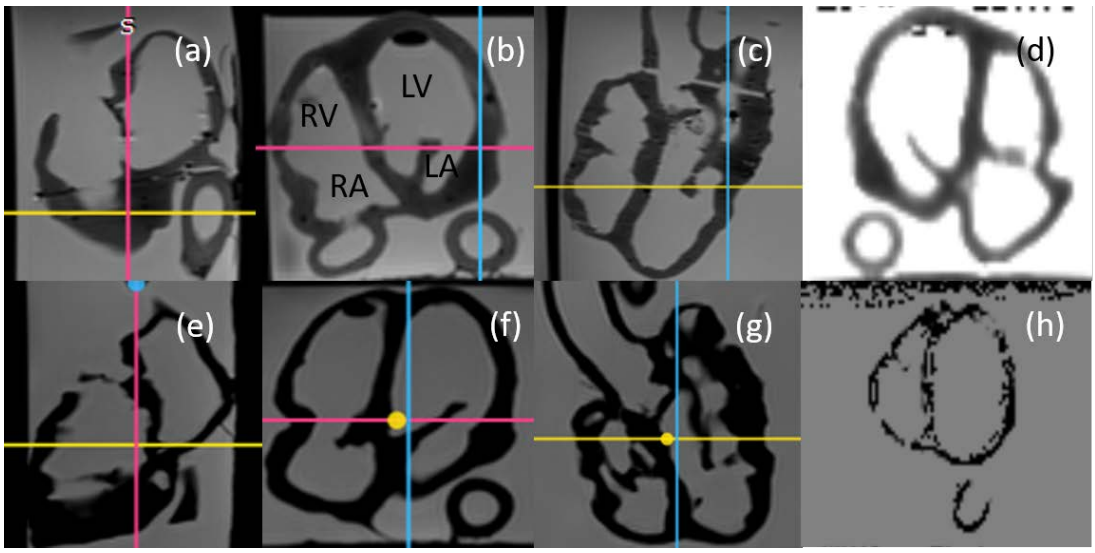

Figure 4.10. MRI images from multiplanar orthogonal views in T2-weighted and T2-mapping modes. T2-weighted: Layfomm40 phantom (a–c) and Tango Plus phantom (e–g); T2-mapping: Layfomm40 phantom (d) and Tango Plus phantom (h)

4.4 Discussion

From the comparison between Tango Plus cardiac phantom and Layfomm40 phantom, the Tango Plus phantom has observably better quality in terms of resolution and surface smoothness. The resolution of the Tango Plus phantom is 0.2 mm, which is two times better than the resolution of the Layfomm40 phantom, which has a resolution of 0.4 mm. Additionally, Tango Plus can be stored in air at room temperature, while Layfomm40 can only be stored in water to maintain its flexibility. Meanwhile, from the visual inspection of the 3D printing results, both phantoms demonstrate good shape and dimension stability. Even though the Layfomm40 material could absorb abundant water inside, the TPU copolymer inside it could help keep the printed models' stability in the flexible form after its PVA component washed away, various fluids could then fill the created pores to tune the material's properties so it can resemble real cardiac tissue in many aspects. The FDM printing technique provides many options in tuning the 3D models' dimensions by rescaling in x, y, z direction easily using the slicing softwares (for example, Cura). However, during Layfomm40's printing, the required high melting temperature around 225℃ may result in slight warping, which needs more attention in the following works.

By comparing the two phantoms' echocardiography images in figure 4.6, the echocardiography of the Layfomm40 phantom has better ultrasound image quality with less reflection and fewer artefacts on the phantom surface. Moreover, Layfomm40's speckle size is smaller than that of Tango Plus which makes it closer to real myocardium's appearance under ultrasound, this finding matches its mechanical properties described in chapter 3, that rinsed Layfomm40 has the closest Young's modulus value to real myocardium [16] with an error of 28.6%–54%. But the X-Ray and CT results in figure3.29 & figure 3.30 show no obvious difference between Tango Plus and Layfomm40 in terms of X-ray contrast or CT number, measured on the Hounsfield Scale and close to 0 for both phantoms. This could be explained by that

radiographic contrast relies on the materials' density difference [110], high radiographic contrast difference could only be observed in materials where density differences are notably distinguished, a higher density material will attenuate more X-rays than a lower density material and appear to be darker in the radiographies; however, the density of rinsed Layfomm40 is 1082 kg/m^3 and Tango Plus is 1100 kg/m^3, the density difference is only 18 kg/m^3, thus, their X-ray and CT imaging results appear to have similar contrast.

The difference in MRI results is still significant between Layfomm40 and Tango Plus phantoms, especially in T1-weighted mode. The T1 and T2 times of the Layfomm40 were 692 ms and 1,267 ms, respectively. While the T1 time of the Layfomm40 was in a similar range as the in vivo myocardial T1 time (~1,000 ms using MOLLI [108]), its T2 time was greater than the in vivo myocardial T2 time (~50ms [109]). The reduced quality of the T1/T2 maps of the Tango Plus did not allow for a confident quantification of T1/T2 times. From the T1 MRI imaging results, the Layfomm40 phantom have a higher contrast with the water background than the Tango Plus phantom, which is closer to real cardiac tissue. This is because the molecules of Layfomm40 after water absorption consist of more hydrogen atoms than those of Tango Plus as Tango Plus is water-resistant. The MRI imaging relies on the excitation of hydrogen atoms [111], which are ubiquitous in the human body. The hydrogen nucleus, which acts as a small magnet, absorbs a certain amount of energy and resonates, that is, the phenomenon of magnetic resonance occurs.

From the multi-modal imaging results and corresponding Young's modulus & ultrasound acoustic results stated in Chapter 3, Layfomm40 is a promising and cost-effective 3D printing material which could be used potentially as a substitute for animal experiments like organoids [112], its porous structure could be used for cell growing and drug delivery after water absorption. Compared to the animal evaluation system, Layfomm40 cardiac model can reduce the complexity of experiments and keep the

compatibility to real-time imaging technology with much lower cost. In previous research, hydrogels were commonly used as biomaterials in advanced functional biosystems creation as they could facilitate cell migration and adhesion in 3D environment [113]. However, the major disadvantage of hydrogels is their lack of mechanical strength due to the fast degradation. Compared to hydrogels, dry Layfomm40' rigidity could guarantee more complicated 3D structures of the printed model, meanwhile, the low cost and ease of availability of Layfomm40 help promote its wider applications and investigations, the cost of Layfomm40 is only 68.95 £/kg, while the cost of GelMA hydrogel is between 7.09-73.44 £/g, and the cost of alginate is 36.7-122.4 £/g.

4.5 Conclusion & Relation to Next Chapter

From the presented results in this chapter, it can be concluded that both Poro-Lay materials and Tango Plus have potential to represent soft cardiac tissue and used for cardiac interventional procedures. The Layfomm40 phantom was printed using an FDM printer and the Tango Plus phantom was printed using a high-end PolyJet printer. After fabrication, the phantoms were imaged using ultrasound, X-Ray, CT and MRI systems, revealing that both materials are suitable for multimodal medical imaging, while Layfomm40 phantom showed better performance under ultrasound and MRI with fewer artefacts and higher contrast. Meanwhile, Layfomm40's ability to absorb other liquids was observed after rinsing, thus, it will be an ideal choice to make cardiovascular models for ablation simulation. Chapter 5 will illustrate the procedure of making a conductive bi-atrial phantom for atrial ablation simulation, with the guidance of CARTO3 mapping and ultrasound imaging.

5. RADIOFREQUENCY ABLATION SIMULATION USING 3D PRINTED THERMOCHROMIC BI-ATRIAL PHANTOM UNDER CARTO3 MAPPING & ULTRASOUND GUIDANCE

The aim of this chapter is to make a bi-atrial phantom to enhance electrophysiological training, thus, the model needs to be compatible to the radiofrequency ablation system and the CARTO3 mapping system, which are often used during the real interventional procedures. Additionally, the ablated points on the phantom surface should be reproduced repetitively during every training and easily visualised for validation of the ablation locations afterwards.

The work about the development of the ablation simulator's finale version presented in section 5.2 of this chapter was mainly affected by COVID-19. The initial CARTO3 mapping experiment using the thermochromic bi-atrial model was completed during November in 2020, after this experiment, due to the impact of COVID-19, I returned to China to start the thesis-writing, while kept collaborating with the students working towards the update of the simulator based on the initial electrophysiological testing results. In June of 2022, the paper of this bi-atrial ablation simulator was published in Applied Sciences Special Issue:

Wang S, Saija C, Choo J, Ou Z, Birsoan M, Germanos S, Rothwell J, Vakili B, Kotadia I, Xu Z, Rolet A, Namour A, Yang WS, Williams SE, Rhode K. (2022, June). Cardiac radiofrequency ablation simulation using a 3D-printed bi-atrial thermochromic model. *Applied Sciences*. https://doi.org/10.3390/app12136553

5.1 Introduction to Atrial Ablation Simulator

Radiofrequency ablation (RFA) using catheters is regularly used to treat atrial fibrillations (AF) [22]. The complexity of cardiac ablation procedure necessitates high-level training for clinical electrophysiologists, including theoretical knowledge, systematic exercise-based learning and professional procedural skills. Ablation simulation systems, including computer and physical models, have become important in clinical training. Furthermore, simulation systems can also be used for ablation device testing and as an alternative approach to animal and cadaver experiments.

The rise of atrial electrophysiology models is motivated by better understanding of the AF mechanism, more efficient design of interventional approaches and guidance with imaging and 3D electroanatomic mapping (EAM) techniques such as ultrasound, X-ray fluoroscopy and the CARTO3 system [25]. Fabricated models and simulation of the whole procedure can help in the development of clinical protocols and the validation of related research hypotheses.

In previous chapters, Layfomm40 and silicone elastomers were investigated to make a complete cardiac phantom, aorta and pathological valve models, and these demonstrated compatibilities with multimodal medical imaging. However, silicone is not electrically or thermally conductive, while Layfomm40 can obtain conductivity after rinsing in saline water, which makes it an ideal material choice for an atrial ablation simulator, as the ablation system requires electrical conductivity to initiate the RFA device and thermal conductivity to penetrate through the phantom.

This chapter aims to produce a 3D printed atrial model that can be used for AA simulation training using a Layfomm40 bi-atrial phantom which is coated with irreversible colour-changing paint. Thermochromic materials are frequently used as temperature indicators with colour change, allowing direct identification of ablation

lesions. The model can therefore be used to train cardiac electrophysiologists in catheter manipulation and ablation procedures. Permanent colour change after radiofrequency ablation allows for immediate identification of lesions in practice. Optical microscopy was used to analyse the inner structure of Layfomm40. With a patient-specific atrium model and mould, a box is designed to mimic the patient position during real interventional procedures. Ultrasound imaging and the CARTO3 mapping system were then used to guide the catheter insertion procedure during a trial simulated ablation on the phantom.

5.2 Atrial Ablation Simulator Fabrication

5.2.1 Atrial Model Segmentation and Initial Simulator Creation

In building the atrial ablation simulator, it is imperative to have an accurate patient-specific atrium model with proper chamber and vascular structure. The model must be hollow to allow the catheter and other devices to be inside and be placed in a saline water environment representing the patient in an anatomical supine position. As shown in figure 5.1 (a), the 3D solid atrium model was first manually segmented from the same cardiac CT image series in chapter 4 using ITK-SNAP (University of Utah, USA). The solid model was then exported into Seg3D (University of Utah, USA), smoothed using a level 2 median filter, eroded by 2 mm and cut. Hence, the hollow atrium model has even myocardium thickness, as shown in figure 5.1 (b). The left and right atrium chambers were divided by the atrial septum so that the catheter puncture could be simulated in the interventional procedure. Table 5.1 shows measurements of the 3D atrium model's main vessels, including IVC and SVC thickness and outer diameter, both IVC and SVC have elliptical shapes. The eight measurements were taken from eight distinct positions of the corresponding vessels using the dimension functions of Meshmixer (Autodesk, USA). The maximum and minimum thickness of the IVC were

3.395 mm and 1.39 mm, respectively. Meanwhile, the SVC has a maximum thickness of 2.528 mm and a minimum of 1.947 mm. The IVC's average thickness and average outer diameter were 2.111 mm and 45.766 mm×30.334 mm, respectively. Moreover, the SVC had an average thickness of 2.317 mm and an average outer diameter of 36.021 mm×26.652 mm.

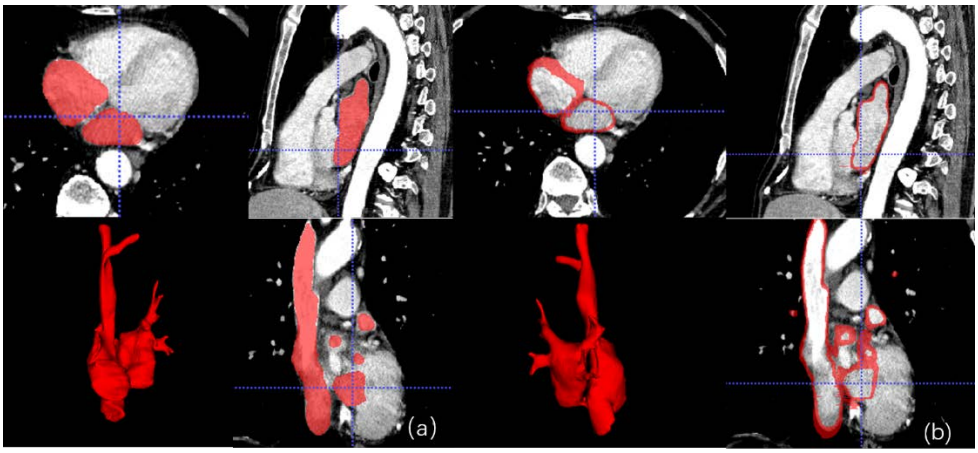

Figure 5.1. Atrium segmentation: axial view, sagittal view, coronal view and reconstructed 3D model; (a) solid segmentation; (b) hollow segmentation

Table 5.1. Size of the atrium model's main vessels

Trials	IVC Thickness (mm)	SVC Thickness (mm)	IVC Outer Diameter (mm)	SVC Outer Diameter (mm)
1	3.395	2.528	45.182×18.500	36.691×26.550
2	1.390	2.324	50.485×38.715	36.461×25.373
3	2.461	2.408	51.595×30.926	38.017×24.450
4	1.816	2.382	45.518×33.620	41.106×27.763
5	1.747	2.435	42.053×35.233	41.007×32.722
6	2.214	2.297	42.490×25.827	33.810×26.513
7	1.910	2.215	43.234×28.913	31.882×25.370
8	1.949	1.947	45.571×30.940	29.195×24.478
Average	2.111	2.317	45.766×30.334	36.021×26.652

Figures 5.2 (a) and (b) depict the detailed structures of the reconstructed atrium model, which include right atrium (RA), left atrium (LA), superior vena cava (SVC), inferior vena cava (IVC), left atrial appendage (LAA), left upper pulmonary vein (LUPV), right upper pulmonary vein (RUPV), left lower pulmonary vein (LLPV) and right lower pulmonary vein (RLPV). The 3D model was then cut in half and exported into Cura (Ultimaker, The Netherlands) to generate the printing toolpath, as shown in figure 5.2 (c). The reason for printing half models was that the single extruder Flsun-QQ printer used for this experiment could not print with water-soluble support material and the main model at the same time. The cut models' open surface enabled the removal of internal supports; such supports will not impede future imaging and ablation procedures. Figure 5.2 (d) shows the final Layfomm40 atrium model coated with grey thermochromic ink, which was mixed with irreversible colour-changing powder (SFCX, UK) and white acrylic paint at 1:10 ratio. The model's size was $102.05 \times 74.75 \times 159.73\ mm^3$.

To guide the ablation catheter, the initial atrial ablation simulator (figure 5.3) used the 3D printed connectors and PVC tubes to anchor the atrium model in a supine position. The catheter was inserted through a sheath and travelled from the IVC to the right atrium, then penetrated to the left atrium. However, this initial simulator lacked extra devices to hold the atrium model and connected tubes. Additionally, future CARTO3 mapping experiments would require the use of conductive patches and magnets. Thus, an extra atrium base and patch holders were needed to improve the simulator's stability and prevent the model from floating. The following sections illustrate the procedure of new simulator fabrication.

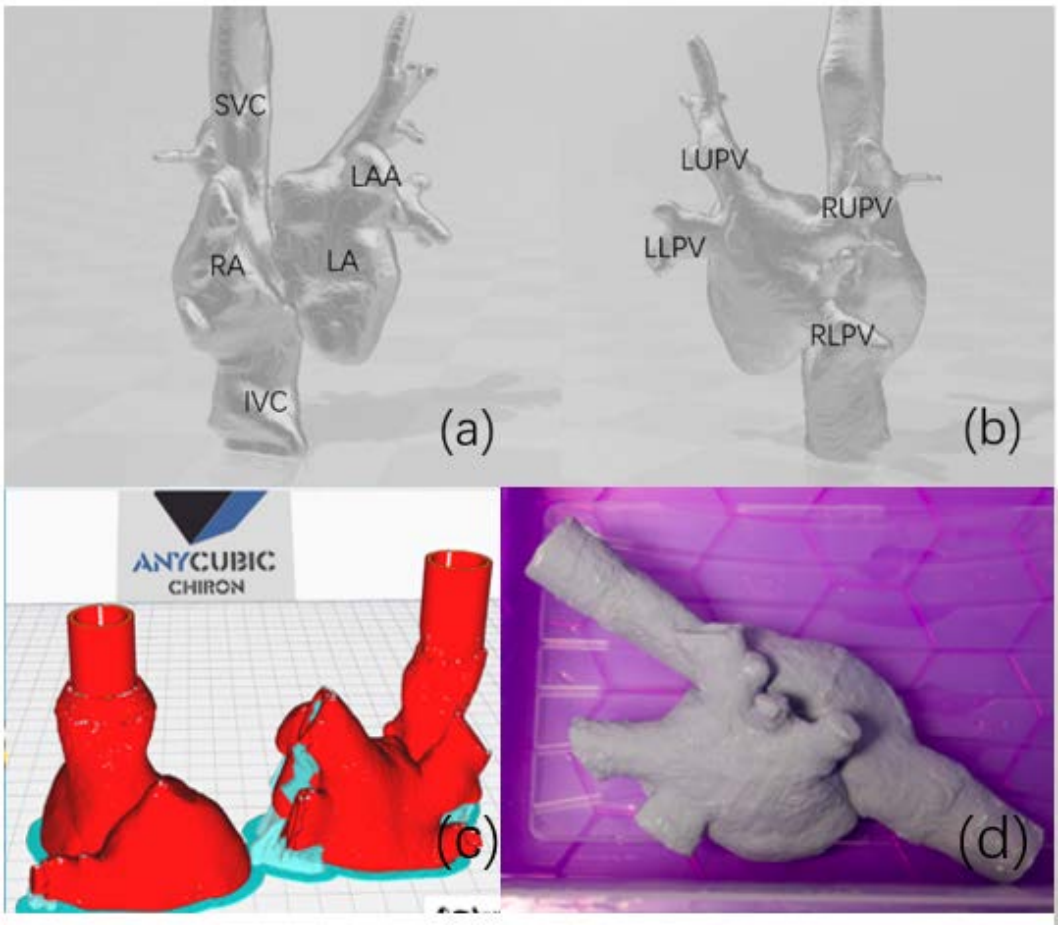

Figure 5.2. (a) Anterior and (b) posterior views of the atrium model; (c) cut atrium model's upper and bottom parts for 3D printing; (d) final Layfomm40 atrium coated with thermochromic paint

Figure 5.3. Initial design of atrial ablation simulator

5.2.2 Fabrication of Atrial Ablation Simulator's Second Version

As the previous simulator had problems with the atrium model floating, a second version of the atrial simulator was developed with a new model base and patch holders. The required water volume to conduct the ablation procedure was at least 10290 cm^3, with a minimum height of 7 cm. Like blood, the saline water used had a 0.9% concentration. To initiate the CARTO3 mapping system, six conductive patches should be placed on the bottom of the box and top of the water, and the patch diameter is 20 cm. As the patches will float inside the water tank, they should be fixed by extra cylinders to make sure they are located at proper heights. Based on the height of the atrium model container and water, the long cylinder should be 30 cm to hold the bottom patches, and the short cylinder should be 17 cm to hold the top patches. Figure 5.4 depicts the computer-aided design (CAD) of the patch holders and atrium box.

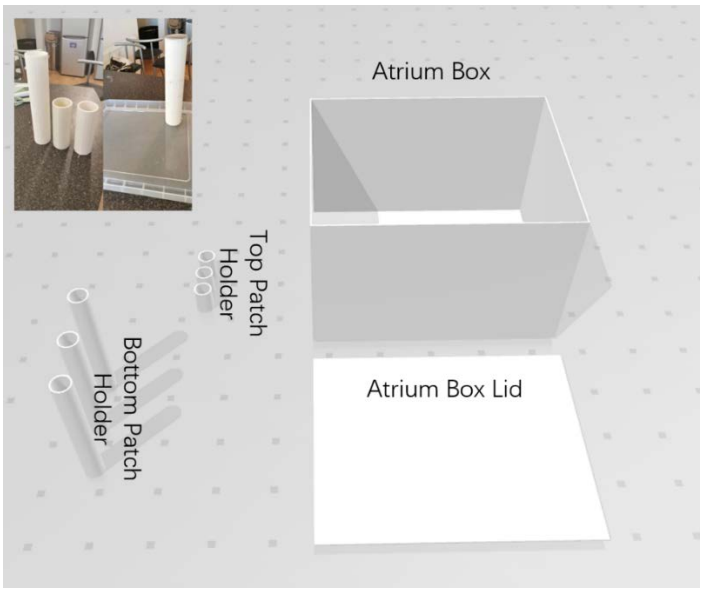

Figure 5.4. Upgraded CAD design of the atrium model container with patch holders

Initially, the cylinders were printed using white PLA materials, as shown in figure 5.5. The holes on the box lid were cut using a wood engraving craft kit that has a burner pen with an adjustable temperature. All the holes have the same size as the conductive patches with equal distance between them. Once the PLA cylinders were attached to

the box, the designed atrium mould base was placed in the box's centre for imaging and ablation purposes.

Figure 5.5. Upgraded assembly of atrium model container with patch holders

Since the base was used to hold the atrium and prevent floating, its initial version was designed as a negative mould of the solid atrium segmentation (figure 5.6 (a and b)). The mould was then cut into half via Netfabb (Autodesk, USA), as depicted in figure 5.6 (c and d). The hollow atrium model fits the mould's internal structure perfectly. Figure 5.7 displays the hollow atrium model and mould printing results using clear resin at 0.3 scale of the original size, they were used to validate if the atrium model will fit the current mould design. The atrium model was placed within the bottom mould (figure 5.7 (c)) and the top mould (figure 5.7 (b)) functioned as a seal. The assembled model and mould remained stable in the water tank because the resin density is 1.1 kg/m^3, which is higher than the water density (1 kg/m^3)

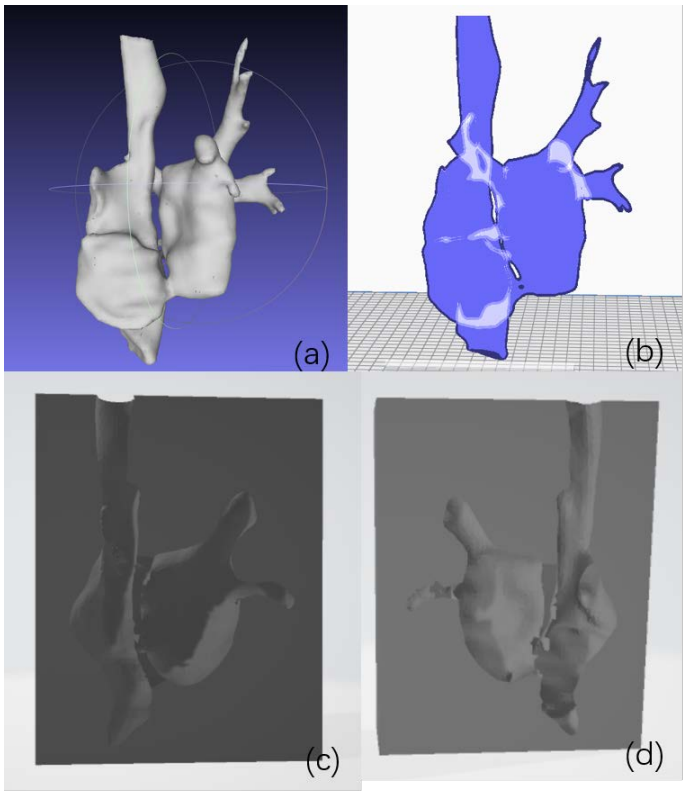

Figure 5.6. Initial CAD of the atrium mould: (a) solid atrium model segmentation; (b) virtual X-ray view of the atrium model; (c) bottom & (d) top mould based on the solid atrium segmentation.

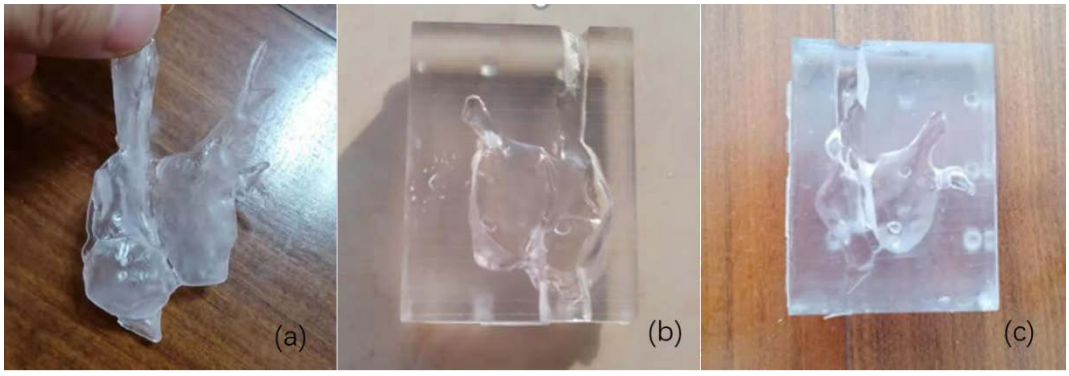

Figure 5.7. Printing results of the initial atrium mould using clear acrylic resin in 0.3 scale to validate the model fitting: (a) hollow atrium model; (b) top & (c) bottom of atrium mould.

However, the atrium model's complicated vessel structures prevented it from completely fitting into the mould. Part of the main model remained outside, making it

difficult to link the whole atrium to the tubes and container. Thus, the atrium base was optimised, the top mould was changed to include two clamps to grip the IVC and SVC. Subsequently, the atrium mould base was extended, and two more clamps were added to keep the PVC tubes attached to the atrium (figure 5.8 (a and b)). The clips and o ring were used to assemble all the base parts. First, they were printed at 50% scale with resin (figure 5.8 (c and d)), once the new mould base and atrium model were confirmed to fit with each other, they were printed in full scale using white PLA (figure 5.8 (e)). The whole assembly was able to fit into the box container (figure 5.8 (f)). Hence, the printed Layfomm40 atrium model was built using this mould and placed inside the container, with all patch holders fixed on top of the lid (figure 5.9). Even though the PLA material's density was lower than that of water, the atrium and mould base assembly did not float inside the water tank since the design fitted securely between all patch holders.

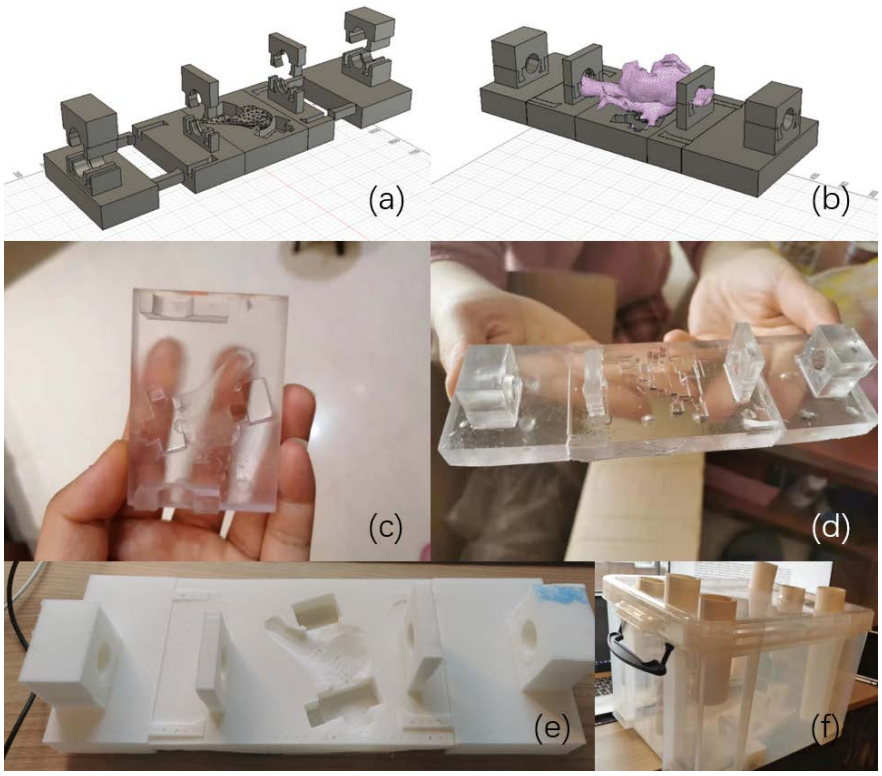

Figure 5.8. (a& b) Upgraded CAD model of the complete atrium mould and container; (c & d) resin printing results of 0.5 scale; (e &f) PLA printing results and full-scale version assembly

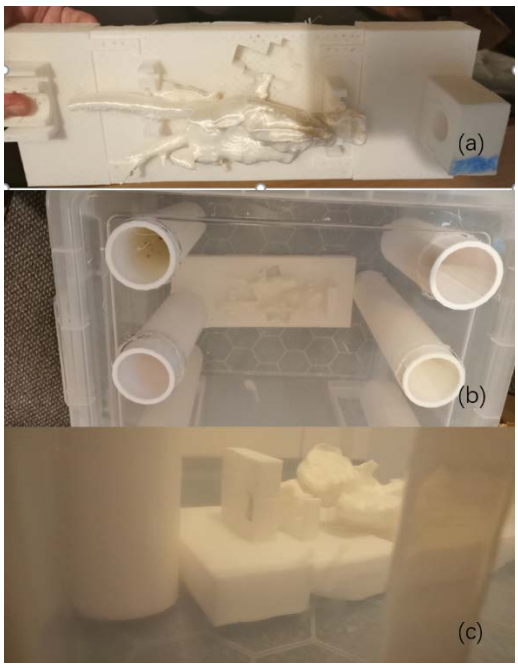

Figure 5.9. Upgraded mould assembly with Layfomm40 atrium model inside a water-filled container: (a) top view of atrium model and mould base assembly; (b) top view of container with patch holders; (c) side view of mould assembly when filled with water

5.2.3 Fabrication of Atrial Ablation Simulator's Final Version

Even though the previous mould design assisted in keeping the atrium model, tubes and all conductive patches inside the container and preventing them from floating, there were still some issues. The 3D printed patch holders were not impermeable, and water leakage might affect the magnets used for CARTO3 mapping. During the experiments, the atrium model was difficult to rotate or move due to the mould's fixed clamps. Thus, further modifications were made to the simulator's design, focusing mainly on the clamps and patch holders. As shown in figure 5.10 (a & b), the small clamps held the atrium's SVC and IVC, while the bigger ones were used for the attached PVC tubes. Unlike the previous version, the top and bottom parts of both clamps were connected by PLA plastic rivets, and their caps were manufactured using a metal spatula, creating a 1–2 mm nail head. Once the rivets were completed, they were used to join the clamps that held the IVC and SVC. The reason for using plastic rivets instead of nylon bolts

and nuts was that the latter could be easily unscrewed during model rotation. At the same time, by adjusting the screws' height, these clamps could slide and be fastened on the mould rails. Figure 5.10 (c) shows the printed 0.5 scale version of the mould and atrium constructed with rigid white resin and a Yidimu light-emitting diode (LED) printer (Yidimu, China). The layer's thickness was only 0.025 mm. After printing, all parts were polished with a scraper and cleaned with alcohol to guarantee accurate dimensions. Once the new design proved to be functional, the full-scale version was printed using white PLA (figure 5.10 (d)). As there were six patches with magnets in total to initiate the CARTO3 mapping system, some PVC plumbing tubes with screws on the end caps and Teflon tapes were mounted on top of the container lid. Compared to 3D printed PLA holders, they were watertight. Furthermore, another six printed TPU hooks were placed inside the holders so that the conductive patches could latch onto them. The patch cables were withdrawn from the container to connect the external device. Figure 5.11 illustrates the entire holder assembly on the lid, and the following figure 5.14 (c) further demonstrates that all conductive patches could be firmly attached to the cylinder holders, so later ablation and CARTO3 mapping experiments would be carried out in a stable setup.

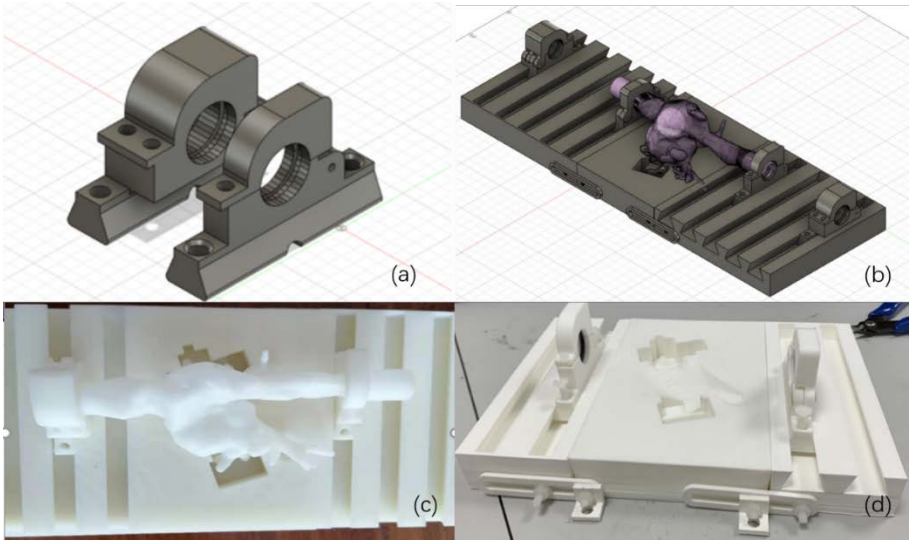

Figure 5.10. CAD model – atrium mould assembly final version (a & b); (c) 0.5 scale printing results using white resin; (d) full-scale version printing results using PLA

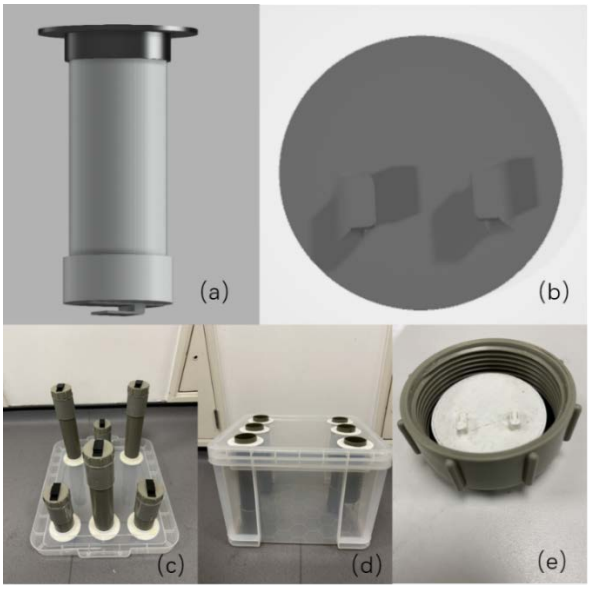

Figure 5.11. Patch holder and container assembly final version: (a & b) electrical patch and sensor holder; (c, d & e) container with six holders

Once the container was ready, the atrium model and the mould base were placed in the box's centre (figure 5.12). To prevent the Layfomm40 model from being broken by the force of stretching the tubes, it was connected to the side catheter valve by two silicone tubes and clamps. The catheter valve on the container's side was used to replicate the insertion of the sheath inside a patient (figure 5.13 (a)). The plastic sheath can help guide the ablation catheter's trajectory and provide a steady force during ablation. The valve was made using a standard garden hose pipe fitting and sealed on the box with one-part silicone sealant. Once inside the atrium, the catheter may be bent and rotated clockwise and counterclockwise (figure 5.13 (b, c & d)) until it finds the right position to ablate the lesion tissue.

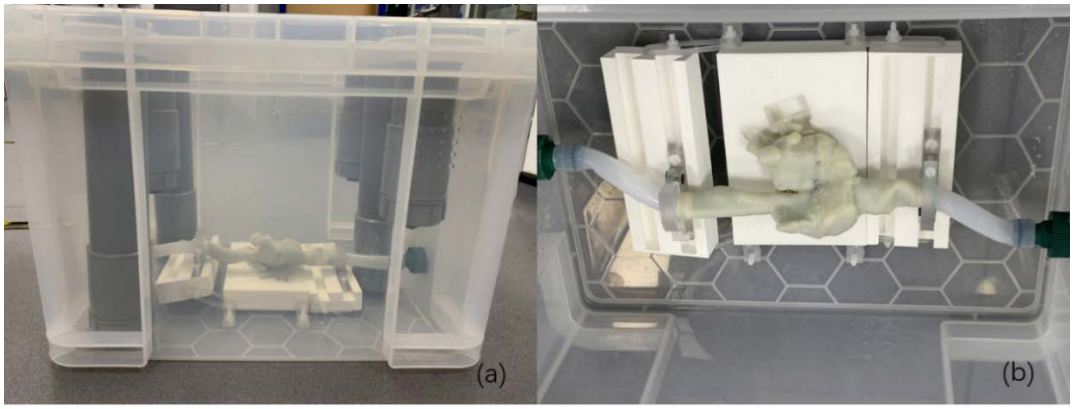

Figure 5.12. Atrium model and mould assembly inside the container: (a) side view and (b) top view

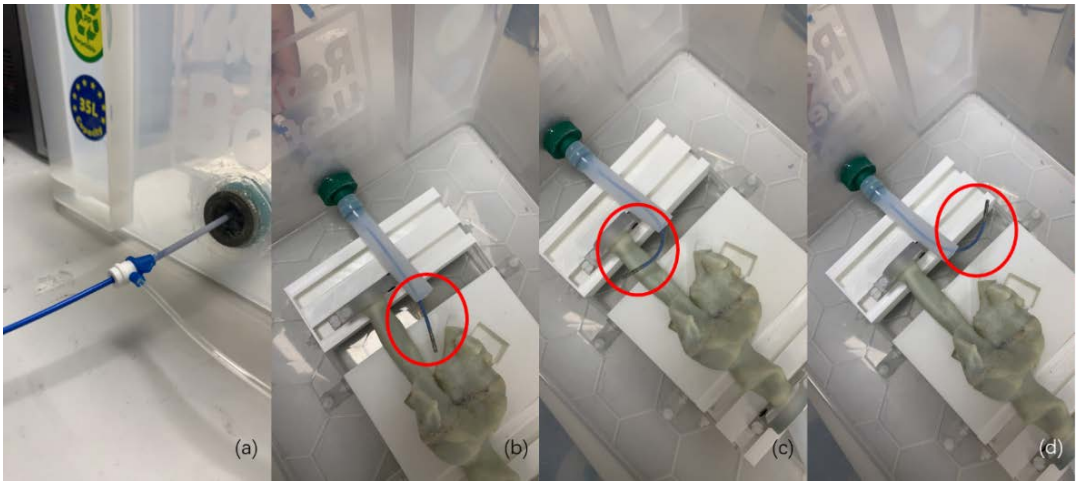

Figure 5.13. Catheter insertion and manipulation inside the atrium box: (a) insertion through plastic sheath; (b, c & d) manipulation of ablation catheter: straight, bending clockwise and bending counterclockwise.

Once all simulator components were tested to work with each other, they were assembled and compactly contained within a 48x39x31$\boldsymbol{cm^3}$ transparent box (Really Useful Plastic Box, UK) with two catheter sheath entry points on both sides connecting to IVC &SVC, as shown in figure 5.14 (a). In figure 5.14 (b), the entry point for the IVC catheter sheath outside the box was extended using silicone tubing to simulate realistic pathlengths for the catheter during atrial ablation procedures and connected to the cardiac phantom on the other side. The water tank was filled up to 25 *cm* in depth with 38°C 0.9% saline water to simulate the human thorax and its conductive properties. As mentioned previously, the lid of the box shown in figure 5.14 (c) was designed to

place the six conductive patches and the corresponding magnets, with three patches above the phantom (simulating the patches on patient chest) and three at the bottom (simulating the patches on patient back). As shown in figure 5.14 (d), the tubes were constructed using standard PVC pipes and gasketed screw-on end-cap fittings and Teflon tape to ensure no leaks were present. The patches were attached to the holders externally via the 3D printed hook while the clips of the magnets were fixed inside it. The phantom base in figure 5.14 (e) was designed to hold the phantom in place during surgery. The clamps grip onto the phantom's tube fittings and hold it in position. Each clamp can slide on its rail, where they are firmly secured in position. The rails can be adjusted in height, angle, and distance from the base to accommodate different heart phantoms. The phantom rests on a soft sponge in the adjustable centre piece, rendering the phantom versatile for all shapes, and finally further secured using a nylon Velcro strap as demonstrated in figure 5.14 (f). All parts of the base assembly are secured in place using M4 nylon bolts and nuts.

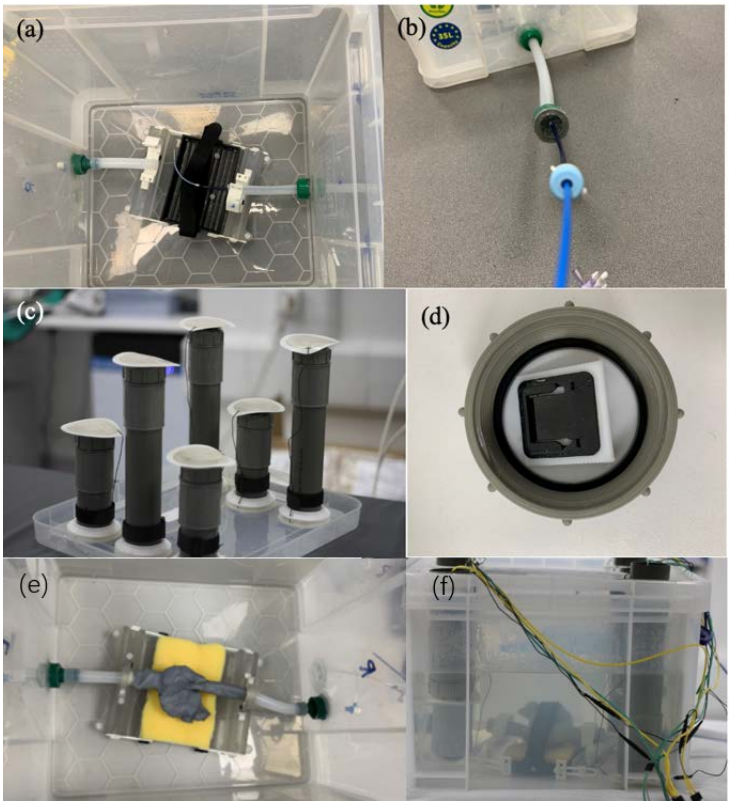

Figure 5.14. (a) Top view of catheter moving in the simulator; (b) catheter entry point from the tube outside the container; (c) fully assembled lid with conductive patches attached; (d) clips of magnets; (e) top view of atrium model, base and box assembly; (f) side view of fully assembled simulator

5.3 Functional Testing of the Atrial Ablation Simulator

5.3.1 RF Ablation Testing of the Layfomm40 Atrium Model

In previous conductivity analysis of Layfomm40 in chapter 3, its electrical conductivity is around $2.98\times 10^{-6}\ S/m$ and thermal conductivity is between 0.339–0.448 W/m/K respectively, this result is the foundation of the simulator's compatibility to the RFA system. In the RFA experiment, radiofrequency was delivered from a Stockert 70 Cardiac Ablation RF Generator (Biosense Webster Inc, USA) and a non-irrigated 8F ThermoCool SmartTouch SF ablation catheter (Biosense Webster Inc, USA) via a 11cm 8F introducer sheath (Cordis, USA). The ablator module could be programmed to function with various power and temperature settings, the catheter can be seamlessly integrated with the CARTO3 system, with combined contact force technology and advanced navigation capabilities, it can provide active measurement of stable contact force and catheter tip location. Unwanted electrical pathways due to lesion formation would be removed by selectively ablating the cardiac tissue using the catheter tip. The whole system's working procedure is depicted in figure 5.15. The radiofrequency generator was connected to the ablation catheter. To avoid overheating, another RF patch was added, and the simulation was run in a water tank. When activated, the catheter tip's heat was transferred to the tissue in a circular pattern. The resulting lesion size is related to the following parameters (figure 5.16): ablation time, water temperature, impedance of the ablated area and ablation power.

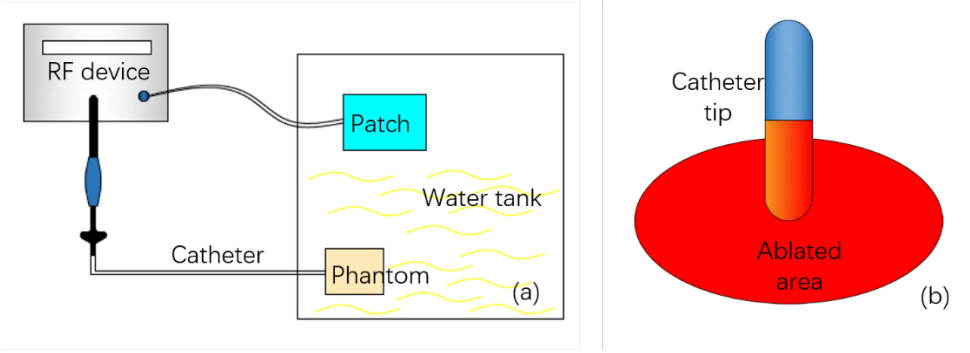

Figure 5.15. (a) Radiofrequency ablation system working procedure illustration; (b) catheter ablation description

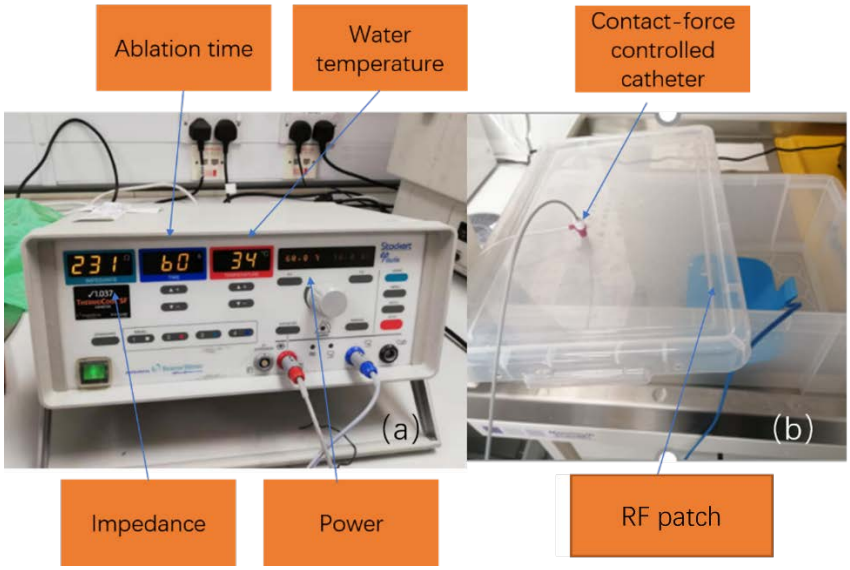

Figure 5.16. (a) Illustration of RF generator device with the following parameters: ablation time, water temperature, impedance of ablation area, ablation power; (b) water tank simulation with catheter insertion via the contact-force controlled sheath and RF patch inside water

To ensure that the simulation could create a log of ablation location on the Layfomm40 material as on real tissue, the ablation was first performed on chicken breasts and subsequently on Layfomm40 discs. The printed disc had a 2 cm radius and 5 mm thickness, with one layer of irreversible thermochromic paint, and the pigment: white acrylic paint base mass ratio of the thermochromic paint is 1:10. Figure 5.17 shows that Layfomm40 with irreversible colour-changing coating can produce an ablated point

similar to the mark on a chicken breast. A conventional ThermoCool Smart Touch ablation catheter (Biosense Webster, USA) was used during this benchmark experiment, as it was a trial experiment before the next ablation temperature and power setting comparison experiment, the ablation catheter was directly put on top of the disc without using the contact force control setup during the 30s ablation. The aim of this experiment was to demonstrate the novel use of colour changing paint that is temperature dependent to display ablation mark with similarity to the chicken breast mark in terms of appearance.

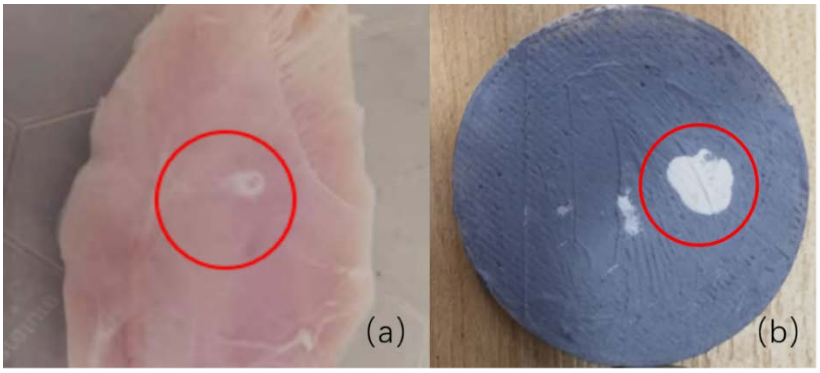

Figure 5.17. Ablated lesion size of (a) chicken breast and (b) thermochromic Layfomm40 disc using an ablation temperature of 70 ℃ and power of 70 watts during the initial trial 30s ablation.

Table 5.2 shows the results of how RF generator settings affect the ablation mark's size, all sizes were measured using a Luthier's Featherweight digital ruler. And this time in order to eliminate the effect of contact force variation, the catheter was inserted at a 90° angle through a femoral sheath. The impedance could be adjusted by changing the amount of salt in the saline water, which must generally be between 120–130 Ω. Each simulation lasted 60 seconds, with the water temperature around 38 ℃. To create a repetitive and stable ablation mark size of 3.25±0.25 mm, the ablation temperature should be between 70–80℃, while the ablation power should be between 70–90 Watts. With the current thermochromic pigment mass ratio 1:10, if the temperature was lower than 60℃ and the power was less than 40 Watts, no ablated marks could be generated

on the Layfomm40 disk. Moreover, a temperature higher than 90℃ and power higher than 90 Watts would produce a much larger mark than was required, with a diameter of around 5 mm.

Table 5.2. Ablated mark sizes on thermochromic Layfomm40 disc using different ablation temperatures and power settings (mm)

Ablation Temperature (℃) / Power (Watts)	50	60	70	80
30	NA	NA	NA	NA
40	NA	NA	2.7	2.4
50	NA	2.3	1.3	1.6
60	NA	1.4	1.8	3.3
70	NA	2.4	3.2	3.3
80	NA	1.9	3.0	3.2
90	NA	2.5	3.2	3.5

5.3.2 CARTO3 Mapping on Layfomm40 Atrium Model

The CARTO3 electroanatomic mapping system used in this experiment is manufactured by Biosense Webster, which helps facilitate the integration of patients' electrophysiological and anatomical information, as well as aid cardiologists in determining the right location to treat tachycardia [25]. The system is a catheter-based electrophysiological system which consists of three main sub-components: ECG (electrocardiogram) subsystem which connects to the patient body; location technologies including CARTO magnetic location technology and advanced catheter location; and mapping technology which builds up and displays the cardiac chambers

together with the mapping points during reconstruction. During the interventional ablation procedure, the ablation catheter is connected to the patient interface unit and RF generator. When recognised by the system, the catheter can be displayed on screen in real time.

While the anatomical mapping result is being built, the surface reconstruction of the corresponding cardiac chamber can be visualised in a high level of detail. As shown in figure 5.18, the initialisation of the CARTO3 mapping setup is determined by the locations of back patches (green circle) and chest patches (yellow circle), and during one interventional case, the system can adjust for any movement automatically in case of patient position change. Figure 5.18 (a) shows the interface of the CARTO3 mapping system. The conductive patches should be placed precisely based on the positions shown in figure 5.18 (c), which imitates an actual patient's supine position [114] (figure 5.18 (b)).

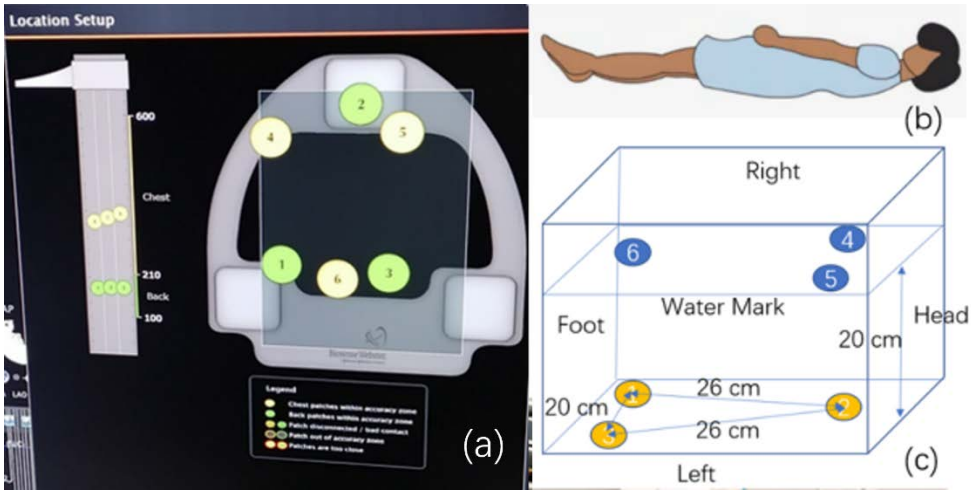

Figure 5.18. (a) The interface of the CARTO3 mapping system's location setup; (b) supine position of a real patient [114]; (c) simulated supine position in a water tank

Then, the simulator was taken to the cardiac catheterization laboratory, placed on the patient table and connected to the CARTO3 system. An 8F ThermoCool Smart Touch SF (Surround Flow) (Biosense Webster, USA) ablation catheter was inserted via a

11cm 8F introducer sheath (Cordis, USA) into the inferior vena cava. The ablation catheter was connected to the CARTO3 system, the irrigation system and the RF generator. The right side of the model was mapped to generate the geometry of the right atrium and the vena cava. The introducer sheath was replaced with a 60cm 8.5F 55º Heartspan Transseptal Fixed Sheath (Biotronik, Germany). The catheter passed from the right atrium into the left atrium through the transseptal puncture in the bi-atrial model. Mapping was then performed of the left atrium, while ablations were performed only in the right side of the model. Every ablation duration was fixed for 45 seconds.

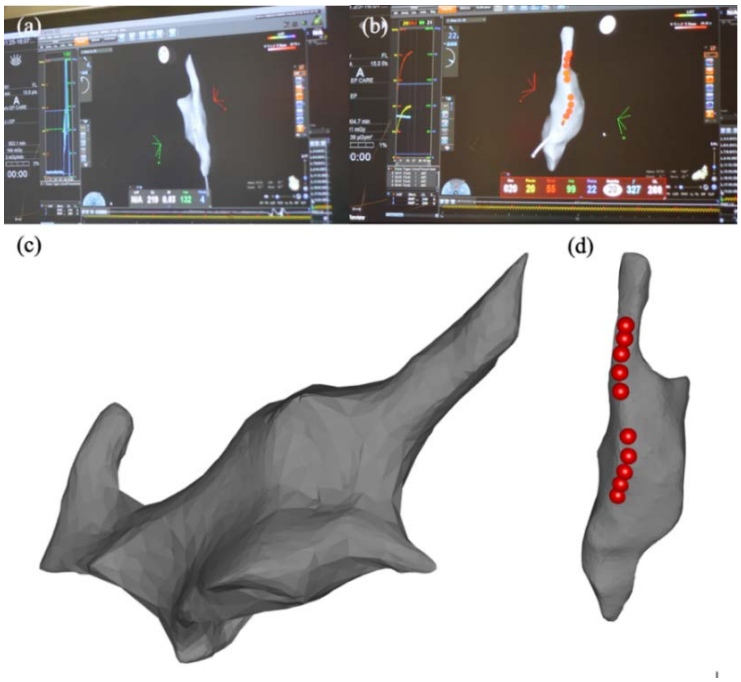

Figure 5.19. (a) CARTO3 mapping the RA; (b) screen view during RA ablation; (c) LA mapping results; (d) RA mapping results with 10 ablation point

As shown in figure 5.19 (a & b), the RA was mapped first, once a satisfactory result was achieved the doctor proceeded to locate the transeptal puncture using the mapping catheter and fluoroscopy as guidance. Using this sheath and the catheter was effectively manoeuvred to map the LA as shown in figure 5.19 (c). After this the mapping catheter was removed and the RF ablation catheter was introduced. As shown in figure 5.19 (d) and figure 5.19 (a & b), five lesions were first created in the cavoatrial junction/SVC following a vertical distribution, in order of increasing ablative power, from inferior to superior, the power settings for each ablation point were as follows: 15.9W; 16.0W; 22.0W; 23.0W; 30.6W; using a fixed power setting of 21.5±1.5W, five additional marks were created in the posteroinferior aspect of the RA, displaying an average diameter of

3.43mm, and the thermochromic pigment : acrylic paint mass ration used on this model was increased from 1:10 to 2:15, to allow lower ablation power settings and easier ablation points demonstration. For demonstrative purposes, a sample cutting was made for closer inspection of ablated marks. No colour change was observed in the external thermochromic paint layer (figure 5.20 (e)), indicating that transmural heat penetration did not occur. This is further supported by figure 5.20 (f); preserved full-thickness integrity of the Layfomm-40 confirms no thermal deformation of the ablated atrial wall.

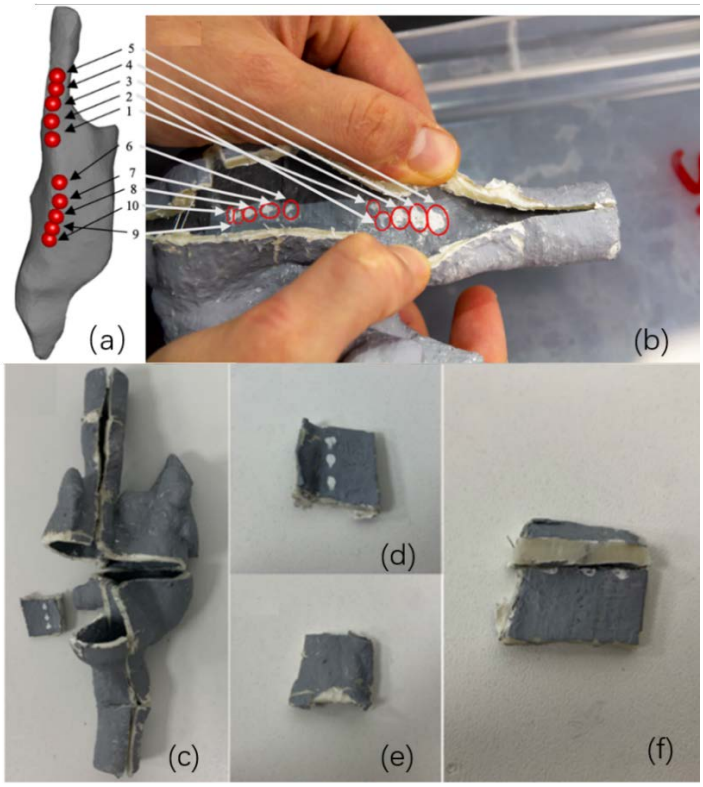

Figure 5.20. (a) Exported geometry and ablation points from the CARTO3 system showing the RA and the vena cava; (b) cut away of the atrium model immediately after the ablation experiment showing the lesions and their correspondence to the ablation points; (c) cut away of the dry atrium model; (d) ablation points clearly visible on the internal surface; (e) external surface is not affected by the RFA; (f) transmural cut that shows no effect inside the model wall.

5.3.3 Ultrasound Testing on Layfomm40 Atrium Model

TOE is usually used during the transseptal puncture to ensure high rates of success and low complications. Mid-oesophagus bicaval view [115] is one of the 20 standard TOE views used to monitor the catheter puncture between the atria, as it demonstrates both clear LA & RA, as well as IVC & SVC.

To simulate the complete atrial ablation procedure, a separate ultrasound experiment was implemented on the Layfomm40 atrium model. Chapter 3 and chapter 4 have proven the good ultrasound compatibility of the Layfomm40 material, but the limitations of the environment made it difficult to collect all possible TOE standard views in vitro on the full chamber cardiac phantom. By adjusting the probe on top of the two chambers of the atrium model, a realistic bicaval view was obtained with the catheter inserted inside the right atrium. The echocardiography of the phantom from the bicaval view in figure 5.21 (a) showed that the imaging result was close to a real patient's echo shown in figure 5.21 (b) (data collected in St Thomas Hospital, London, UK). The only difference between the simulated ultrasound image and the real ultrasound image was that the former's scattering had higher contrast to the background, producing a clearer outline of the atrial septum.

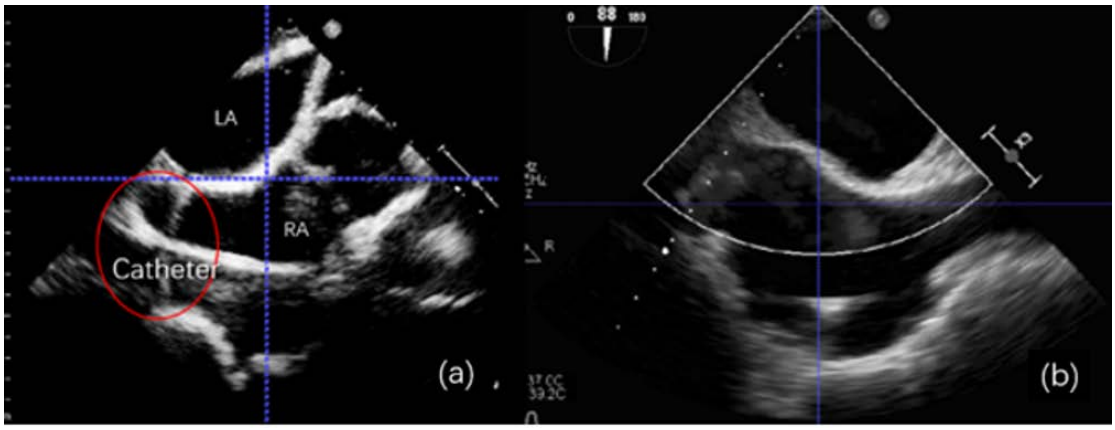

Figure 5.21. Atrium ultrasound—bicaval view (a) phantom echocardiography with inserted catheter in red circle; (b) real patient echocardiography

5.4 Discussion

From the measurements listed in table 5.1, the bi-atrial model's IVC's average thickness is 2.111 mm and the SVC's average thickness is 2.317 mm, which match the results reported in [116] that myocardium wall thickness is between 1 and 4 mm. The left atrium chamber diameter is between 37.9–43.6 mm, which is also within the range of a real patient's LA diameter (39.6±5.6 mm) [117]. Meanwhile, from the anterior and posterior views of the bi-atrial model shown in figure 5.2, the 3D segmentation includes the most important anatomical details of both the LA, RA and associated vessels, which guarantees the fidelity of its CARTO and ultrasound imaging results. However, this initial simulator built was too simple to be applied in the radiofrequency ablation and CARTO3 mapping system, thus, two new versions were developed until all simulator components were tested to work with the electrophysiological system, from the visual inspection of the in-vitro catheterisation procedure shown in figure 5.13, the ablation catheter could be inserted, bent and rotated smoothly inside the simulator.

The ablated material must be conductive for the ablation system to work. The Layfomm40 was tested after 3 days of rinsing in saturated saltwater, preliminary results in chapter 3 show that it has an electrical conductivity around $2.98\times 10^{-6}\ S/m$ and thermal conductivity between 0.339–0.448 W/m/K respectively, its small electrical conductivity is enough for initiating the RFA device while its thermal conductivity helps the ablation heat penetrate through the bi-atrial model.

During the initial trials shown in figure 5.17, the Layfomm-40 discs with irreversible thermochromic paint coating were confirmed to be RFA sensitive. Table 5.2 shows that marks could be formed on the discs with temperatures ≥60ºC and power settings ≥40W. The diameter of the mark best matched the mark produced on the chicken breast when the temperature and power were ≥70ºC and ≥70W, respectively. Settings below these either produced no mark or inconsistently sized marks. Consistent marks were produced

with temperatures of 70-80ºC and powers of 70-90W, the average mark's diameter for these settings was measured to be 3.3±0.3mm (±1SD, n=9), which was the same as the ablation mark's diameter around 3 mm in the chicken breast at 70W, 70ºC with 60 seconds ablation time. Figure 5.19 and figure 5.20 indicate that satisfactory ablation result could be achieved using the CARTO3 mapping system as guidance, while transmural heat penetration did not occur on the 3D printed bi-atrial model, the ablation locations displayed in the CARTO3 system match the results in reality. Furthermore, the atrium echocardiography in bicaval view shown in figure 5.21 also recorded the transseptal puncture procedure during catheterisation.

Combined with both CARTO mapping results and ultrasound imaging results, the RFA simulator demonstrates good potential in pre-surgical planning, relevant medical device testing, and even personalized clinical translation. The next step of this work would be a trial with trainees using this ablation simulator to prove it can be beneficial for the patients.

5.5 Conclusion and Relation to Next Chapter

As a further step for the use of Layfomm40 material other than medical imaging, this chapter describes the development of a multi-functional atrial ablation simulator consisting of a Layfomm40 bi-atrial model with irreversible thermochromic coatings. The simulator includes an adjustable atrium mould base, and two sliding clamps, six conductive patch holders and a plastic container. The conductivity of Layfomm40 in the saline water environment activated the radiofrequency ablation device and catheter, and the mixed thermochromic painting helped the lesion mark appear visibly on the ablated area so that it could be identified after the ablation procedure. The setup of the whole simulator included features to allow compatibility with the CARTO3 mapping system, and the material's ultrasound compatibility made it possible to produce a realistic bicaval echocardiographic view during the transeptal puncture procedure.

However, based on the comparisons between Layfomm40 and traditional silicone materials in chapter 3, as well as the visual inspections of both cardiac phantoms fabricated in chapter 4 & 5, Layfomm40 suffered from delamination problem, thus, not durable enough to be applied in dynamic experiments like flow tests, while silicone can withstand the high pressure for long time. Besides, the previous Layfomm40 cardiac phantoms can only provide clear images from the chamber view, but limited in other echocardiography views, for example, the aortic valve short axis (AXSA) view, which is often used in blood flow measurements, thus, in the next chapter, to acquire the haemodynamic results, silicone aorta and different pathological aortic valve models will be fabricated separately. The manufacturing techniques include both two-part moulding and direct silicone printing. The related flow and imaging tests will be illustrated as well, offering more simulation results with the power of 3D printing.

6.MANUFACTURING OF ULTRASOUND- AND MRI-COMPATIBLE AORTA AND VALVE PHANTOMS USING TWO-PART MOULDING TECHNIQUE VS. SILICONE PRINTING TECHNIQUE

The aim of this chapter is to make aorta & valve models which could resemble biological ones, in addition to the anatomical appearances, these models need to be compatible to both ultrasound and MRI imaging, as these two imaging modalities will be used to monitor the valve opening and closing. Meanwhile, they should also be durable enough to provide reliable transvalvular pressure data.

The work about the valve manufacturing using silicone printing technique in section 6.3 of this chapter was mainly affected by COVID-19, the printer assembly was suspended during the lockdown period from March to May in 2020. Luckily, the main work presented in this chapter was not affected by COVID-19, the ultrasound & MRI-imaging experiments using two-part moulded silicone valves were completed in 2019, and the relevant results were published in *MICCAI-STACOM* international conference: *Manufacturing of ultrasound-and MRI-compatible aortic valves using 3D printing for analysis and simulation.* While I led the silicone model's manufacturing work, another Ph.D student Harminder Gill in Dr Pablo Lamata's group from King's College London led the haemodynamic experiments using these silicone valves during collaboration. Thanks to the effort of Harminder Gill, the haemodynamic results and analysis of the manufactured valve models were published in *Journal of Cardiovascular Translational Research: Aortic stenosis: haemodynamic benchmark and metric reliability study.*

Wang, S., Gill, H., Wan, W., Tricker, H., Fernandes, J. F., Noh, Y., ... & Rhode, K. (2019, October). Manufacturing of ultrasound-and MRI-compatible aortic valves using 3d printing for analysis and simulation. *In International Workshop on Statistical Atlases and Computational Models of the Heart* (pp. 12-21). Springer, Cham. https://doi.org/10.1007/978-3-030-39074-7_2

Gill, H., Fernandes, J. F., Nio, A., Dockerill, C., Shah, N., Ahmed, N., Raymond, J., Wang, S., Sotelo, J., Urbina, J., Uribe, S., Rajani, R., Rhode, K., & Lamata, P. (2023). Aortic Stenosis: Haemodynamic Benchmark and Metric Reliability Study. *Journal of Cardiovascular Translational Research*. https://doi.org/10.1007/s12265-022-10350-w

6.1 Introduction to Silicone Aorta & Valve Models

As mentioned in the previous literatures in section 2.1.3, aortic valve stenosis [89] is the most common valve-related disease, which can result from different underlying pathologies, and its macroscopic appearance is typically classified into one of the following categories: calcified valve, rheumatic valve or bicuspid valve. Treatment of the valve, by means of surgical or minimally invasive methods, is required, as no pharmacological methods demonstrate efficacy at preventing progression. However, due to the limited views and resolution of medical imaging devices, current diagnostic methods using imaging systems are inadequate for optimal management, such as determining the timing of valve replacement, while model-based in-vitro simulations of valve disease and pre-procedural interventional planning can benefit from advances in 3D printing, as 3D phantoms can present more detailed and accurate cardiac anatomy and related diseases in reality [118].

The fabricated whole cardiac phantom described in chapter 3 cannot be used for high-fidelity representation of cardiac valves. Moreover, the used material, Layfomm40, is

not durable enough to withstand physiological flow conditions. As silicone is an optimal material with stiffness and tenacity similar to soft tissue [119], this chapter will describe the manufacturing of silicone aorta and aortic valve models, with two-part moulding or silicone printing techniques.

To make the anthropomorphic aorta & aortic valve models for ultrasound & MRI imaging and in-vitro flow simulations, a novel low-cost two-part mould technique was first developed, with an internal mould using polyvinyl alcohol (PVA) that can be easily dissolved in water at room temperature. As well as the normal silicone valve, some typical pathological valves were fabricated for comparison, and the imaging compatibility was validated using both ultrasound and MRI together with transvalvular pressure-drop measurements. Besides, silicone printing technique was also applied to make another valve model, with comparable performances to the moulded one under ultrasound and flow test.

The use of 3D-printed valve models and the experience of manufacturing them is expected to be broadened in the near future with progress in material engineering, computer-aided design and diagnostic imaging systems [120]. Although it seems a far stretch of the imagination, the in-vivo implantation of 3D printed aortic valves may become the final goal [121].

6.2 Anatomical Valve and Aorta Manufacturing Using Two-part Moulding Technique

Based on the mechanical characterisation results in chapter 3, among different 3D printable and unprintable materials, Dragonskin 10 silicone was chosen as the aorta material with a Shore A hardness difference of 29.10%, while Ecoflex 0030 was chosen as the valve materials with a Young's modulus difference of 11.29%, and both phantoms were fabricated using the two-part moulding technique.

As mentioned previously, silicone phantoms are used to simulate real-life aortic-valve-related surgical cases, so various valvular pathologies were also investigated, such as rheumatic, calcified and defective leaflets, as shown in figure 6.1 [89]. To simulate different valve pathologies, post-processing, such as calcification, was also performed on the original normal phantom. Under the same imaging and flow environment, the phantoms were expected to behave differently: rheumatic valve leaflets will not be able to fully open due to adhesion, the calcified valve will have abnormally high contrast on the cusps and there will be backflow similar to the rheumatic valve, the bicuspid valve will only have one moving leaflet as the other two are merged into one, and the dilated valve will need higher pressure to open and close than a normal valve.

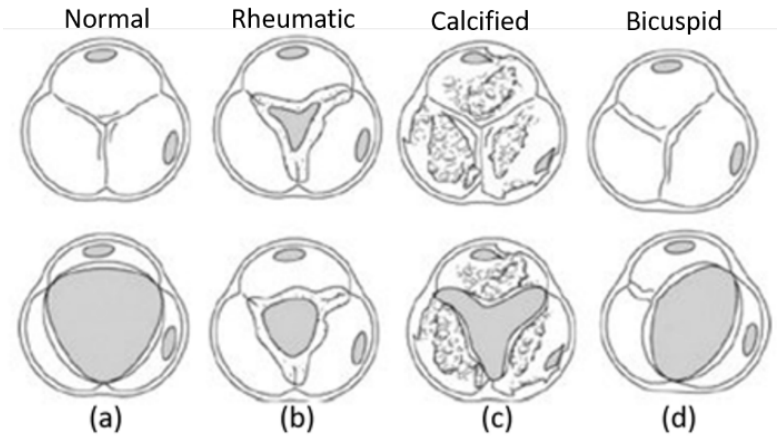

Figure 6.1. Pathological valve models: (a) normal valve, (b) rheumatic valve, (c) calcified valve and (d) bicuspid valve [89]

6.2.1 Manufacturing of the Silicone Aortic Valve

Before making the actual silicone valve, the 3D model needed to be constructed either via segmentation or computer-aided design (CAD). Initially, the original solid valve model was segmented from a male chest CT scan using the ITK-SNAP (University of Pennsylvania, USA) thresholding tool, then smoothed using a median filter in Seg3D (University of Utah, USA). Finally, a hollow model was generated using the erosion–

dilation method in Seg3D, with a valve thickness of 2 mm. The segmentation can be viewed in figure 6.2. However, this segmentation had valve disease and the aortic root was curved, and we needed a healthy model with a straight root, such as that demonstrated in figure 6.4 (d), as the baseline. Another CAD valve model was therefore drawn using SolidWorks 2018 (Dassault Systèmes, USA) based on the segmented valve structure, which was used as the final version to make the moulds.

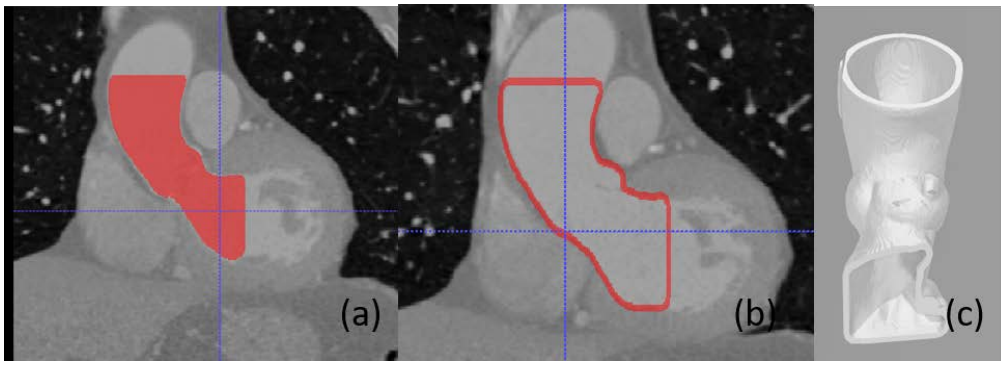

Figure 6.2. Aortic valve model generation: (a) solid valve segmentation, (b) hollow valve segmentation and (c) 3D hollow valve model.

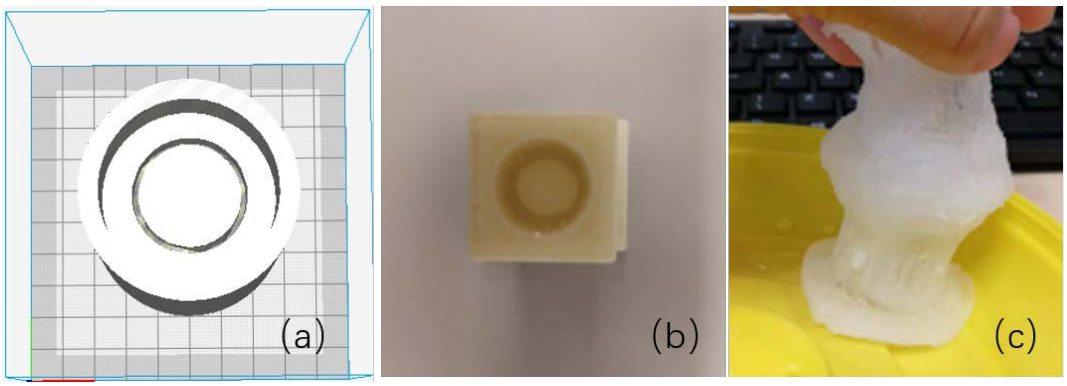

Figure 6.3. (a) 3D CAD model; (b) printed results of the initial valve-manufacturing trial using a hollow PVA mould; (c) silicone valve model after mould dissolving

Initially, the mould has a single valve-shaped cavity, as shown in figure 6.3 (a). During the first trial, as the complex cavity contained many curved, thin tracts and unremovable printing supports, it became too difficult to pour all the silicone liquid into the mould (shown in figure 6.3 (b)), and after dissolving the mould, the silicone valve had

incomplete structures and an uneven thickness, as shown in figure 6.3 (c). Thus, the two-part mould technique was then developed to replace the one-part mould.

The cavity was created using the same valve model, but instead of only using the cavity function, the mould was split into an external mould (figure 6.4 (a)) and an internal mould (figure 6.4 (b)). Thus, after printing, the support materials of both moulds were easily removed. The external mould was printed using rigid PLA, while the internal mould was printed using water-soluble PVA. With the assembled prints held together by clamps (figure 6.4 (c)), degassed Ecoflex 0030 was poured into the mould. Once the external mould was opened and the internal mould was dissolved, the normal valve model was completed, as depicted in figure 6.4 (d).

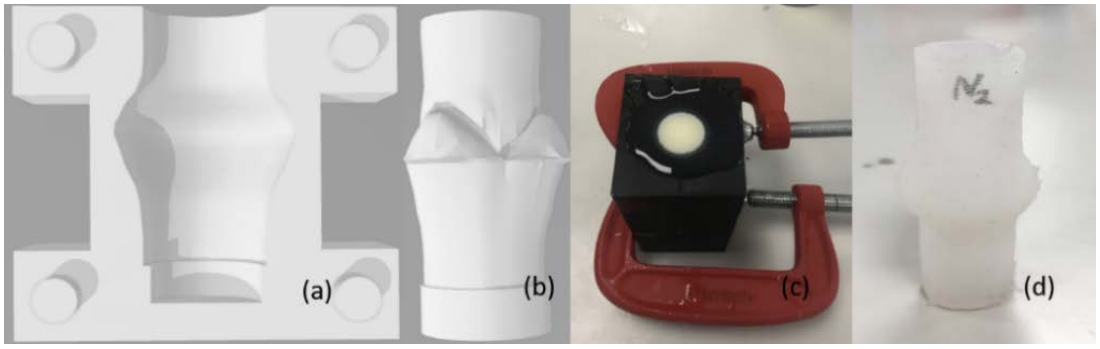

Figure 6.4. Two-part mould-based silicone valve manufacturing: (a) external mould, (b) internal mould, (c) two-part mould assembly and (d) a normal silicone valve.

From figure 6.5, it is clear that the quality of the silicone valve fabricated using two-part moulds outperforms the one-part moulded valve, with smoother surface and more even thickness.

Based on the normal silicone valve, some pathological valve models were then created, as depicted in figure 6.6, including a rheumatic (figure 6.6 (b)), calcified (figure 6.6 (c)) and bicuspid (figure 6.6 (d)) valve model. The rheumatic valve was created by ensuring that the anatomical orifice consisted of cuts made a third of the way down on each valve

closure line to recreate the circumferential fusion of the cusps. The calcified valve was created by paint-brushing on more silicone to replicate leaflet thickening and stiffening, while the bicuspid valve was created by leaving one commissure fused to mimic a raphe.

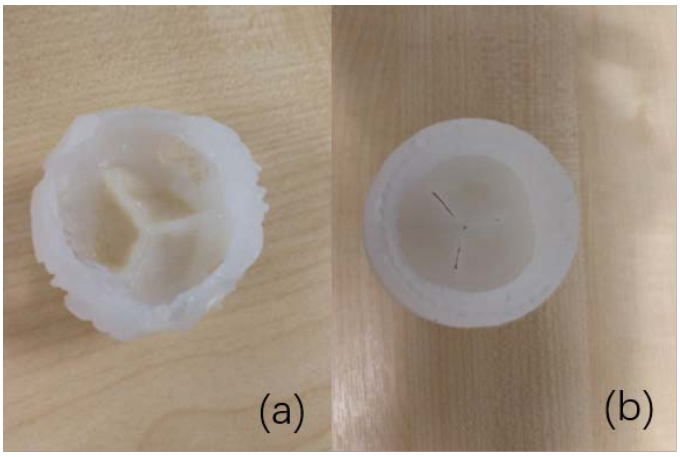

Figure 6.5. Comparison between (a) one-part moulded and (b) two-part moulded silicone valve.

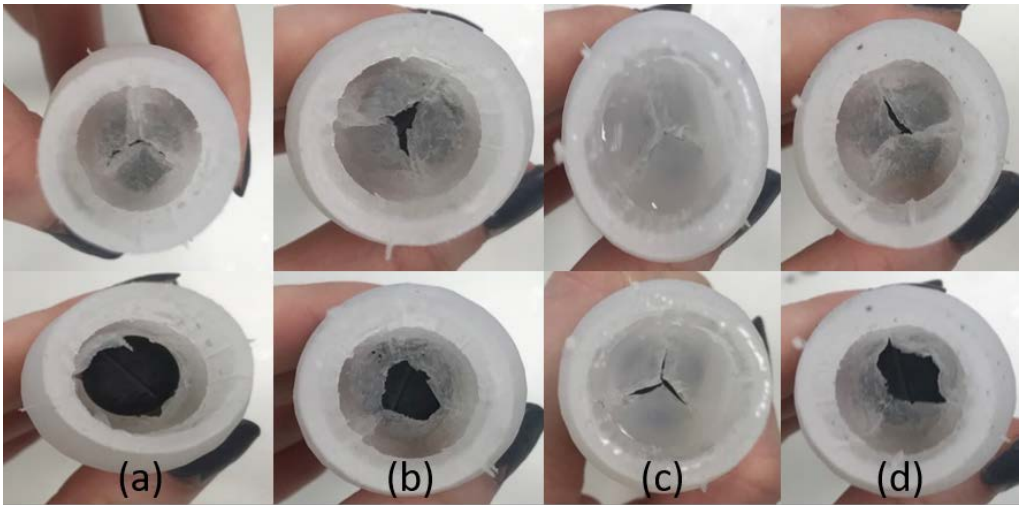

Figure 6.6. Manufactured silicone valves, closed at the top and open at the bottom: (a) normal valve, (b) rheumatic valve, (c) calcified valve and (d) bicuspid valve.

6.2.2 Manufacturing of the Silicone Aorta

Based on the same two-part mould idea, the hollow aorta model was created using Dragonskin 10 silicone. As shown in figure 6.7, the hollow aorta and the mould parts were designed using SolidWorks 2018. The size of the aorta phantom was the same as that of the average adult aorta (313*135* 32 mm^3), and its thickness was 2 mm. To better connect the valve model to the aorta, the aortic root was the same size as the valve root (32 mm), and on the bottom of the mould a circular cut was left open to let the silicone in. As the Flsun 3D printer is limited by printing size, the aorta moulds were printed using a large-size Anycubic Chiron printer with a maximum build volume of 400*400*450 mm^3. As shown in figure 6.8 (a), the internal PVA mould was printed using a 0.97 scale of the original CAD design to leave more space between the external mould and the internal one. The time taken to fully dissolve the internal PVA mould was approximately 1 day, and the final aorta model fit well with the previous valve model, as shown in figure 6.8 (c).

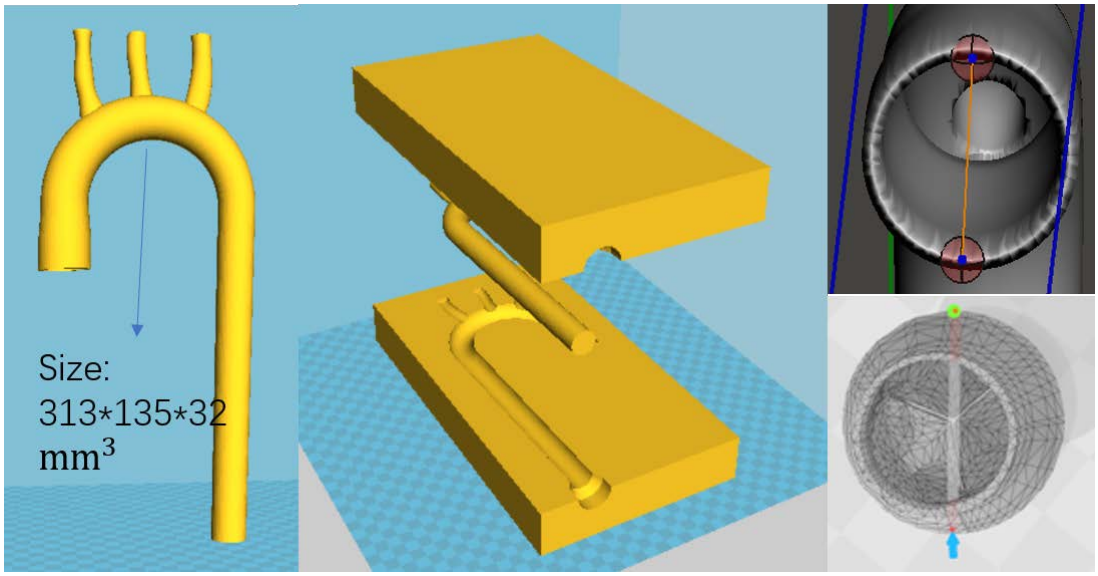

Figure 6.7. STL file of the hollow aorta and its external and internal moulds.

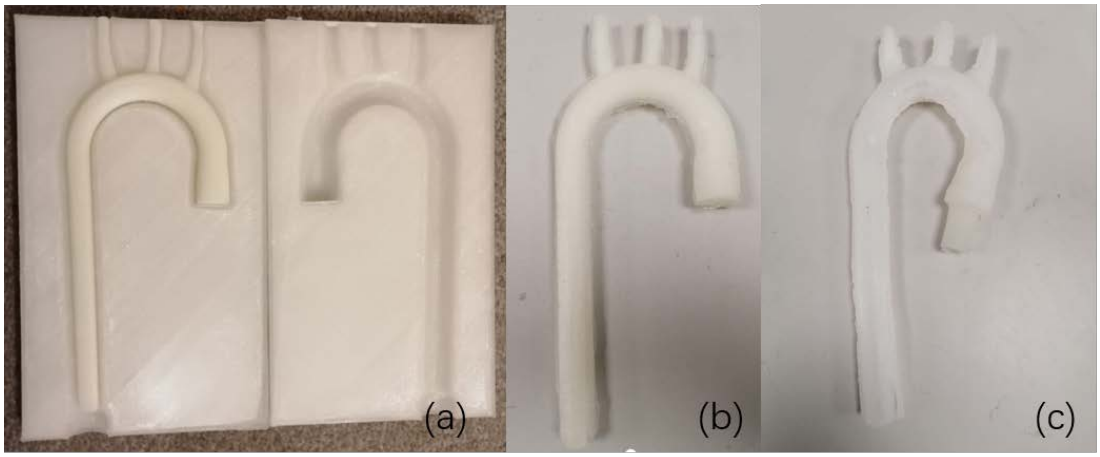

Figure 6.8. (a) Printed aorta moulds; (b) silicone aorta with PVA internal mould; (c) final assembled silicone aorta and valve phantoms.

6.3 Anatomical Valve Manufacturing Using Silicone Printing

Other than the two-part moulding technique, the silicone valve model was also fabricated using silicone printing, as the aorta model's size exceeded the developed silicone printer, only the valve model was made and compared to the moulded one in the following work. The assembling of the silicone printer mainly follows the tutorial in [12], with extra modification of the silicone ink.

6.3.1 Silicone Printer Assembly & Testing

The silicone printer includes three main systems: the extruding system, heating system and the silicone pumping system.

The extruding mechanism involves the assembly of the printer base as well as the customised DIW extruder. Due to cost and adaptability, the silicone printer base is a full DIY kit named Anet A8 (Anet, China) with an open-source design as shown in figure 6.9, the printer base consists of a liquid crystal display (LCD), mainboard, lead

rods, printing bed, power supply, x-y-z motors and extruderand its building volume is 220×220×240 mm^3 which is larger than most commercial bio-printers.

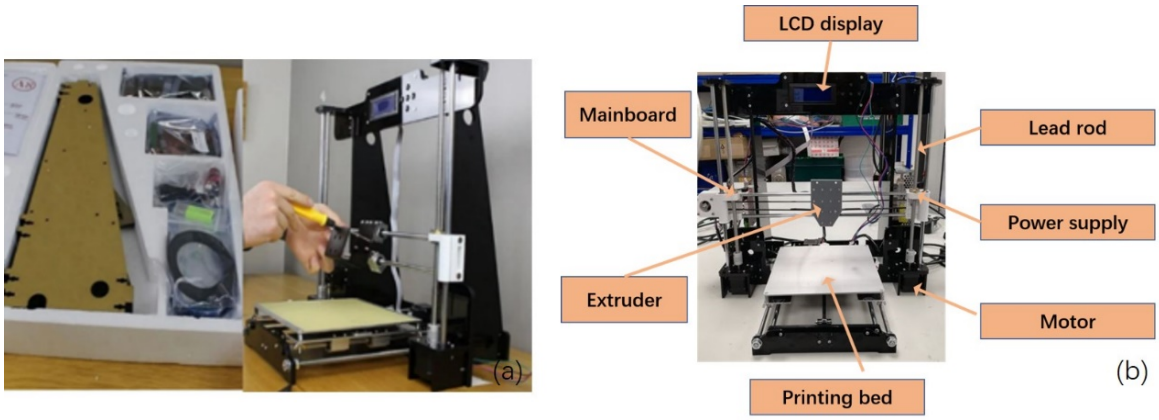

Figure 6.9: Open-source Anet base of a silicone printer with modified extruder holder

The original Anet A8 metal extruder needs to be replaced by a new DIW extruding system to print with two-part silicone. Figure 6.10 depicts a detailed silicone extruder assembly based on the tutorial from [12]. It consists of an upper and lower nozzle, extruder mount, pillar, left and right heater holder, heater wing arm and joint, upper seal and silicone mixer.

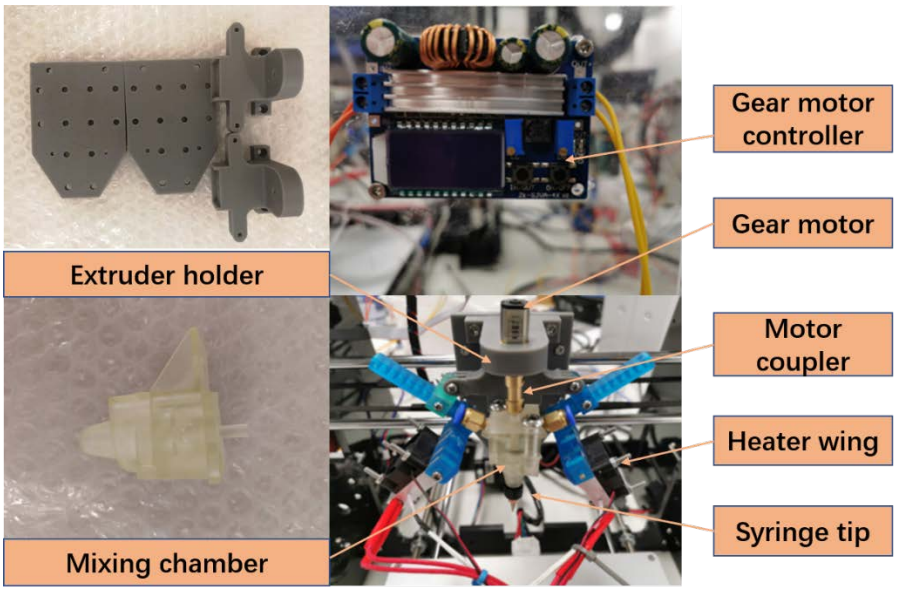

Figure 6.10: Silicone extruder parts and final assembled extruding mechanism

After completing the extruding mechanism, to provide a suitable temperature for

silicone printing, an extra heating system needs to be assembled with the silicone extruder to blow hot air. Figure 6.11 depicts one important component of the heater wing: convective aluminium blocks. The two blocks were designed based on two 50*10*30 mm^3 aluminium cuboids. They are used to transfer heat and have 36 holes arranged in a 6×6 square to allow the air to blow. The fan is attached on top of the block with screws facing towards the extruder tip. When the thermistor is inserted along with the heater, the aluminium block will heat up to a set temperature, and the hot air will pass through the block to help the silicone cure.

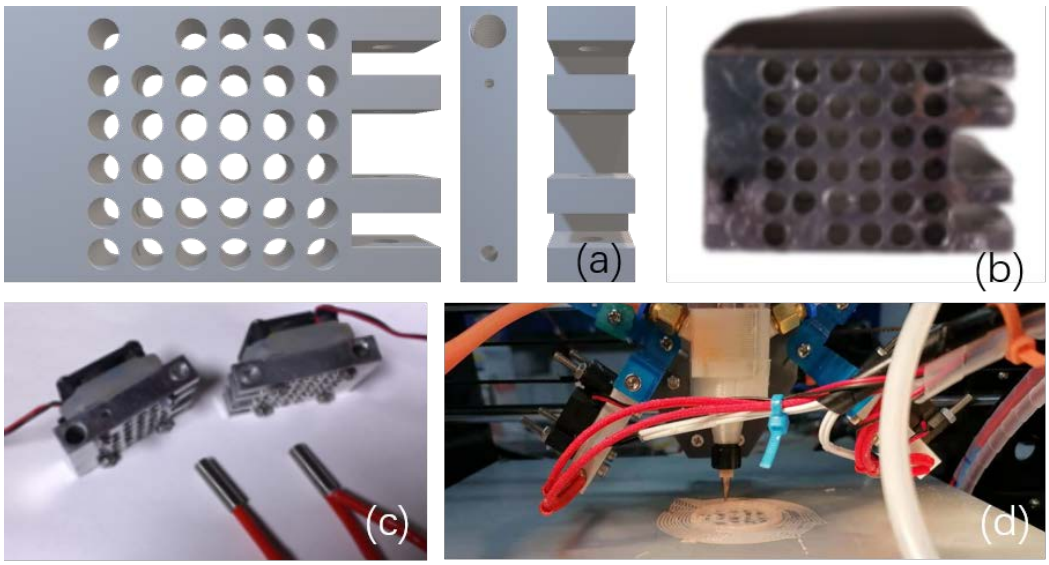

Figure 6.11: Aluminium heating block: (a) 3D view of heat wing CAD model; (b) manufactured metal heat wing; (c) heating iron connected with metal heat wing; (d) heating module connected with silicone extruder

This heating system is controlled by the circuit map placed on a separate acrylic sheet (figure 6.12) following the steps in [12]. During printing, the temperature of the metal heating bed needs to be set around 70 °C. Depending on the types of silicone ink, the printouts generally require post-curing at either high temperature or room temperature from several minutes to hours.

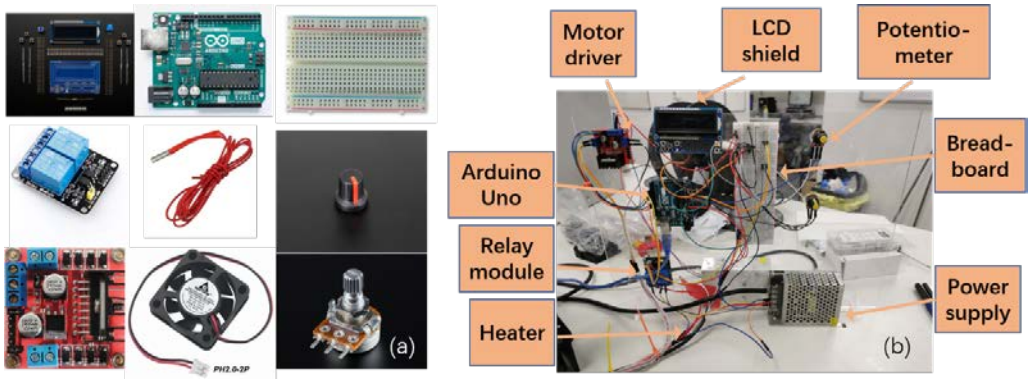

Figure 6.12: (a) Circuit map components of the heating system: LCD shield for speed and temperature display, Arduino board to control fan speed, breadboard, relay module, heater, potentiometer cap, motor driver, brushless fan, potentiometer; (b) circuit map assembly on acrylic sheet.

The commercial syringe pump used for silicone printing in [12] was too expensive and could not easily be customised to adapt to modified silicone inks with much higher viscosities, thus, an external pumping system was developed separately:

The syringe pump was based on a set of linear guides, including an optical axis, lead screw, pillow block bearing, linear rail support, CNC stepper coupler and ball bearing, as shown in figure 6.13. The base parts were used to connect the metal linear guides and motor with the gearbox, and the syringe holder parts were used to fix the 20 ml syringe. All of the drawings in figure 6.13 (a) were completed using UG software (Siemens PLM Software, USA). Figure 6.13 (b) shows the final assembled version of the pump. To print the modified silicone inks with fumed silica addition using a 24 V power supply, the gear ratio should either be 27:1 or 50:1 (from practical tests of all possible gearboxes, 5:1 – 20:1 is too small, 100:1 is too slow); all of the other parameters are listed in table 6.1. With more linear guides and a flat base, the pumps can work with more stability and less noise.

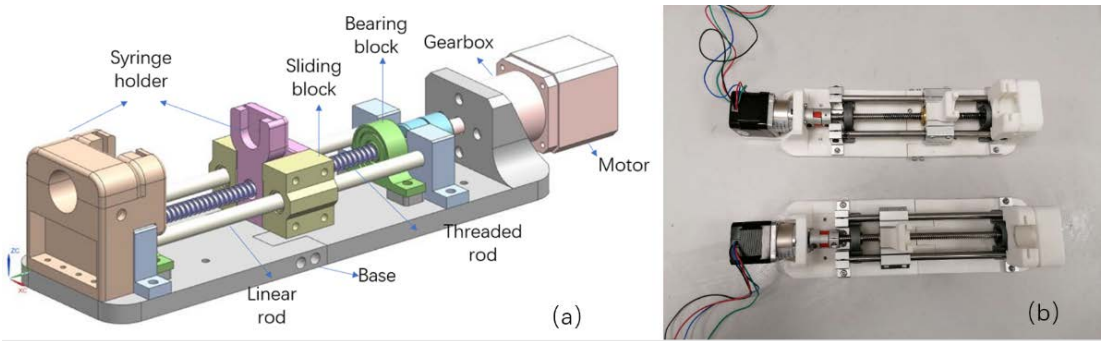

Figure 6.13: (a) Upgraded syringe pump 3D drawings; (b) printed and assembled working syringe pump.

Table 6.1. Key parameters of the syringe pump components

Description	Parameter
Pressure and Force	100 pounds per square inch, 216 N
Thread Torque	1.2–1.45 N·m
Gearbox's Amplifying Ratio	27:1
Voltage and Input Current	24 V, 1.2 A
Gear Motor Step	1.8 degrees/step, 200 steps

The referenced printing parameters for a successful print are a layer thickness of 1.3 mm or higher, a printed infill of 100%, a maximum printing speed of 7 mm/s, a syringe tip larger than 1.3 mm, pumping flow rate of 20 ml/hr if the printing speed reaches its maximum, bed temperature at 60°C, heater temperature at 80 °C and fan speed under 80%.

Before using the silicone printer to manufacture the aortic valve model, a small cylinder was printed during the initial silicone printing test. Based on the rheological characterisation results in chapter 3, Rebound 25 with 20% v/v fumed silica was used

and printed on a heated printer bed. The diameter of the cylinder was 15 mm, and the length was also 15 mm (figure 6.14 (a)). After five minutes, the printing procedure was complete. The printed cylinder is shown in figure 6.14 (c), and the silicone printer can accurately print the CAD model without dimension change (figure 6.14 (d)), this is because the used silicone ink' moderate viscosity can help the extrusion form the filament shape and stay on the printer plate, and the fast crosslinking under heat can prevent the silicone sample from flowing and collapsing.

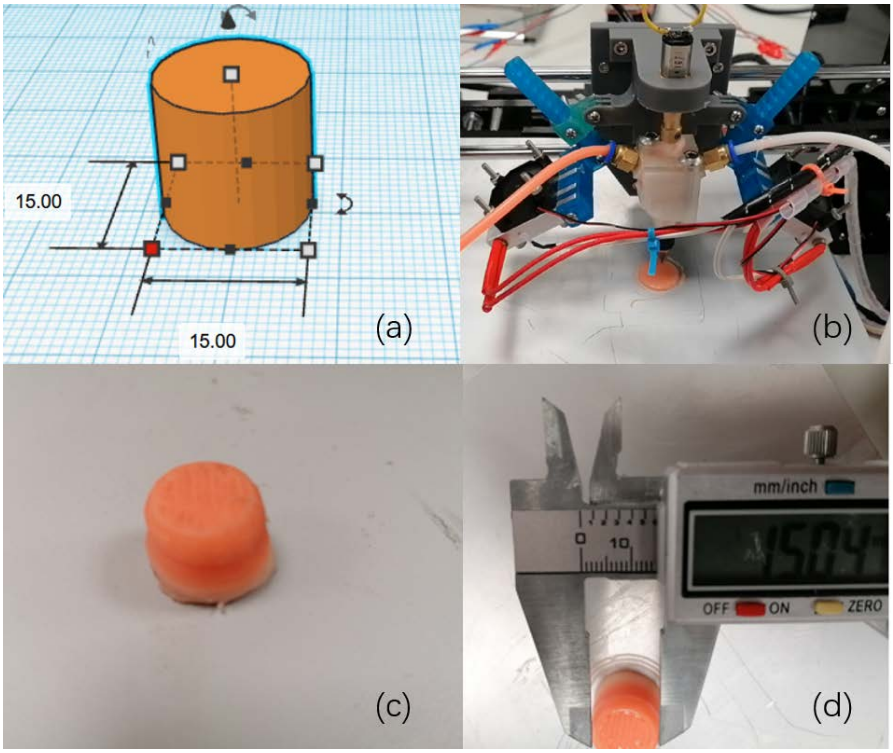

Figure 6.14: (a) 3D CAD model of cylinder sample with the diameter of 15 mm; (b) cylinder sample printing in progress; (c) printed cylinder; (d) diameter measurement of printed cylinder: 15.04 mm.

6.3.2 Comparison Between Moulded & Printed Silicone Valve

Once the silicone printer was assembled and the printing ability was confirmed, the CAD model of the aortic valve shown in figure 6.15 (b) was uploaded in Cura (Ultimakr, The Netherlands) and sliced into g-code. As the silicone printer was still limited by the

inability of printing support materials, the valve printed only consisted of three leaflets without aortic root, then during the later flow test, it was mounted on a plastic fixture inside the tubing as shown in figure 6.16, just like the moulded silicone valve. The ultrasound machine used in figure 6.16 was GE Vivid E95 (GE, USA), and the pulsatile flow pump was a CardioFlow 5000 MRI-compatible pump (Shelley Medical Imaging Technologies, Canada).

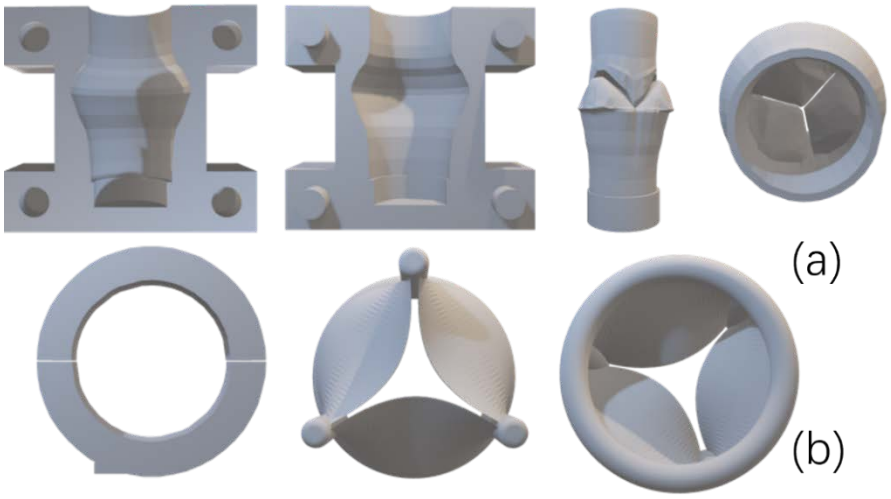

Figure 6.15: CAD Model of (a) moulded valve; (b) directly printed valve

Figure 6.16: Ultrasound imaging platform for valve experiments with a pulsatile flow pump

The moulded silicone valve used Ecoflex 0030 without adding any fumed silica. To make a clear comparison, the directly printed valve in figure 6.17 (b) used Dragonskin

10 silicone mixed with 40% fumed silica as well as blue acrylic paint for differentiation. The changing of the silicone material for the printed valve was because of the unprintability of Ecoflex 0030, whose viscosity is only 3000 mPa.s while the required viscosity for printable silicone ink should be between 10^6-10^7 mPa.s.

Despite of the material change of the printed valve, its ultrasound results shown in figure 6.17 and figure 6.18 demonstrate similar valve structures as the moulded valve's. Figure 6.18 depicts the detailed real-time echoes of both valve models, where the opening and closing of the leaflets can be clearly visualised. Meanwhile, both valves survived in the pulsatile flow during pumping, which indicates that the directly printed silicone valve is as durable as the moulded counterpart.

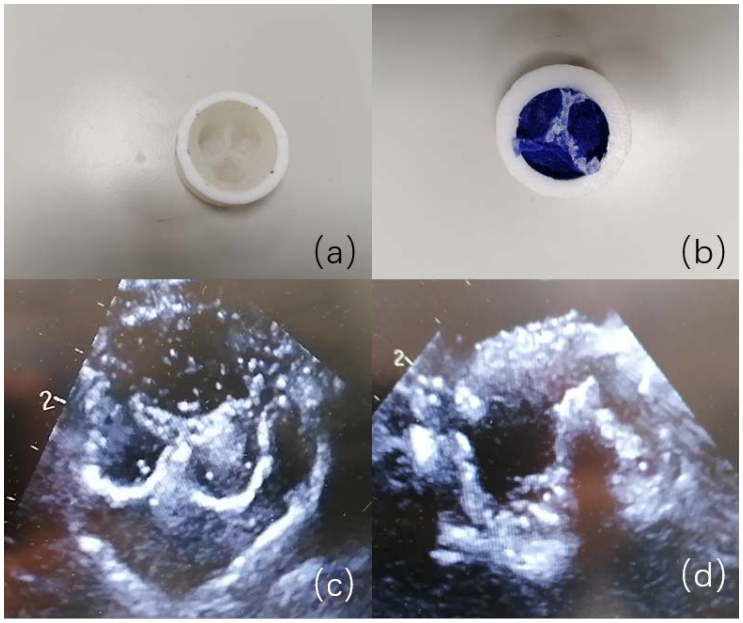

Figure 6.17: (a) Moulded silicone valve; (b) directly printed valve; (c) ultrasound image of (a); (d) ultrasound image of (b)

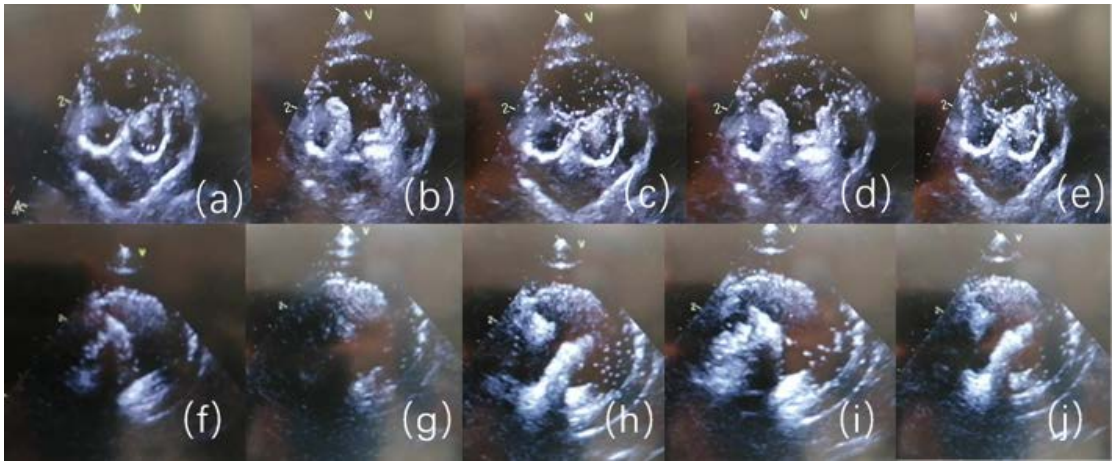

Figure 6.18: (a)–(e) Echoes of the moulded valve; (f)–(j) echoes of the directly printed valve.

6.4 Ultrasound & MRI- Imaging Results and Pressure Analysis of the Aorta & Valve Phantoms

The combination of ultrasound/MRI imaging and peak pressure analysis allows for a more accurate valve pathology identification. Thus, after the manufacturing of the silicone aorta and valve, the phantoms were connected to an MRI-compatible pulsatile-flow pumping platform and monitored by both ultrasound and MRI imaging with pressure data collected. The typical valve pathologies were also compared in terms of in-vitro and in-vivo data.

6.4.1 Ultrasound & MRI-Imaging Results of the Aorta & Pathological Valves

To validate whether the aorta and valve phantoms can provide the desired imaging results, the four types of silicone valve and the aorta were first imaged using 2D

ultrasound from both aortic-valve long-axis view (AV-LAX) and aortic-valve short-axis view (AV-SAX) and 3D MRI from AV-SAX view. The 2D ultrasound images were acquired with the Philips IE33 system (Philips, Netherlands) with a S5-1 probe in a water tank, as shown in figures 6.19 (a) and 6.20 (a)–(c). Figure 6.20 (d)–(f) provides an example of the simulated echocardiography of an aortic valve, aortic arch and descending aorta compared with those in real patients (figure 6.20 (h)–(j)). It can be seen that the silicone phantoms are tissue-mimicking under ultrasound with both a clear inner structure and surface scattering, which means Dragonskin 10 and Ecoflex 0030 have good reflection as well as low attenuation, and the silicone models have been manufactured with the necessary anatomical structures.

Figure 6.19. Medical imaging validation: (a) ultrasound imaging and (b) MRI.

To obtain the MRI images, the silicone aorta and valves were connected to and perfused with an MRI-compatible pulsatile flow pump (CardioFlow 5000 MR). This time, the images were acquired in 1% agar to optimise the imaging results. The imaging procedure is demonstrated in figure 6.19 (b). The catheterisation unit was placed distal to the aortic phantom, the reservoir and pump unit were placed outside the MRI device and the fluid was circulated, as defined by the control unit.

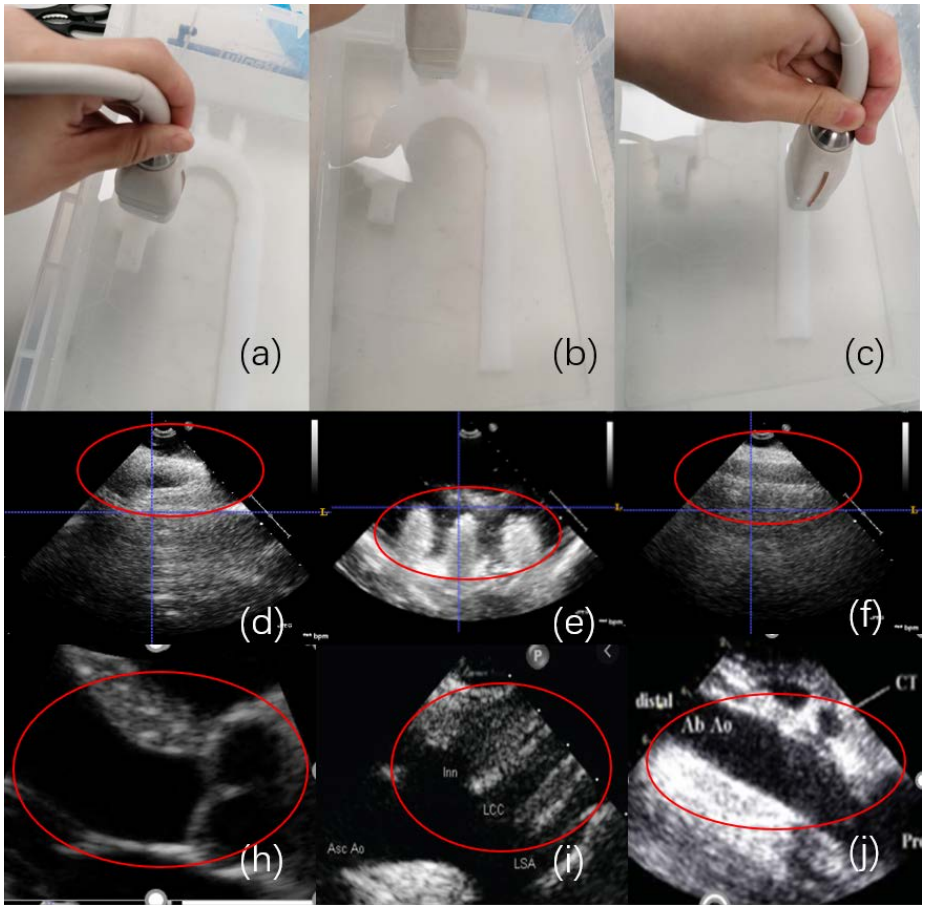

Figure 6.20. Ultrasound imaging of the assembled aorta and valve phantoms: (a)–(c) probe manipulation at the top of the valve, aortic arch and aorta; (d–f) simulated echocardiography; (h–j) real patient echocardiography.

Figure 6.21 (a)–(d) shows the ultrasound images of the four types of aortic valve from an AV-SAX view. Even though the ultrasound images are limited by low resolution and the difference between these valves is less significant, we can still see that the normal valve has a clear three-leaflet structure, the rheumatic and calcified ones have more vague anatomies and the bicuspid one demonstrates an abnormal opening on one side of the leaflets. The MRI images shown in figure 6.21 (e)–(h) present the four valves more clearly. While the normal valve opens fully, under the same pressure, the rheumatic valve and calcified valve open significantly less and the bicuspid valve opens eccentrically. These imaging results qualitatively demonstrate the imaging compatibility and functionality of the artificial aorta and valves made using 3D printing.

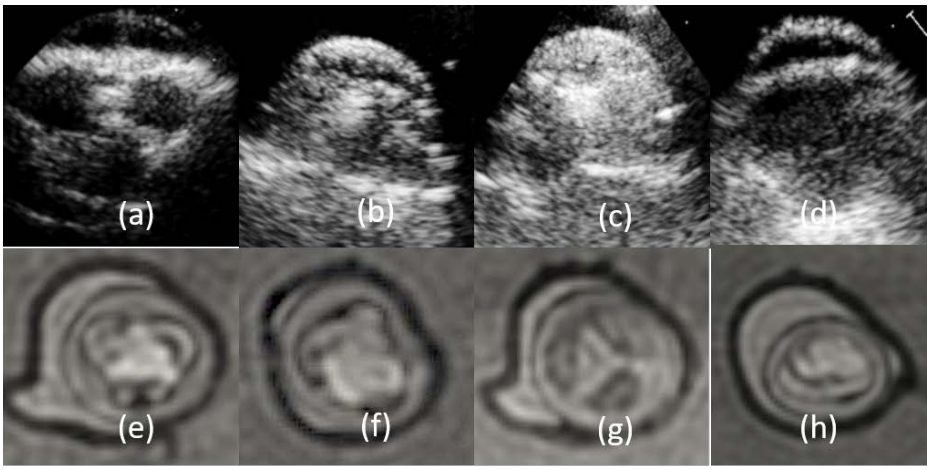

Figure 6.21. 2D ultrasound images of (a) a normal valve, (b) rheumatic valve, (c) calcified valve and (d) bicuspid valve; MRI images of (e) a normal valve, (f) rheumatic valve, (g) calcified valve and (h) bicuspid valve from an AV-SAX view.

6.4.2 Pressure Analysis of Valve Models with Various Pathologies

The pressure results presented in this section were mainly provided by our collaborator Harminder Gill, the joint-work could be referred in the following two publications:

Gill, H., Fernandes, J. F., Bissell, M., Wang, S., & Lamata, P. (2020). 3D printed valve models replicate in vivo bicuspid aortic valve peak pressure drops. *Journal of the American College of Cardiology*, 75(11), 1636.

Gill, H., Fernandes, J. F., Nio, A., Dockerill, C., Shah, N., Ahmed, N., Raymond, J., Wang, S., Sotelo, J., Urbina, J., Uribe, S., Rajani, R., Rhode, K., & Lamata, P. (2023). Aortic Stenosis: Haemodynamic benchmark and metric reliability study. *Journal of Cardiovascular Translational Research*. https://doi.org/10.1007/s12265-022-10350-w

Peak-pressure analysis of aortic coarctation can be used to determine disease severity and guide surgical repair. It can be measured together with echocardiography to get

overestimated pressure values or merged with the MRI technique to obtain haemodynamic parameters [122].

The pressure data collection system diagram is illustrated in figure 6.22, and the detailed components are listed in the legends of figure 6.23: There were eight pressure ports inserted in the flow system, each port could result in a column of fluid in direct continuity. The pressure ports were located at a fixed distances of -30, +15, +30, +50, +75, +100, +200 and +500mm relative to the valve position. Non-compliant 254mm sections of 900PSI-rated Luer-lock PVC tubing (30526-14, Masterflex, Oldham, UK) were attached to the ports allowing parallel connection of 8 PRESS-S-000 pressure sensors (PendoTech™, Princeton, NJ, USA). Each sensor was calibrated and validated against a solid-state pressure catheter (Mikro-Cath, Millar Inc, Houston, TX, USA). The output from the sensors fed into a data controller (National Instruments, Austin, TX, USA) and the results were recorded using MatLab (MathWorks, Natick, MA, USA).

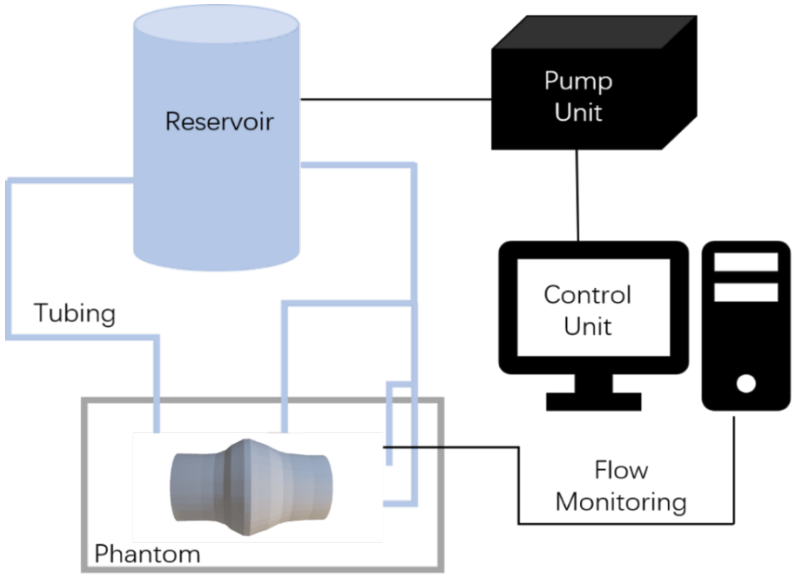

Figure 6.22. Pressure analysis platform of the silicone valve phantoms with a pulsatile flow pump: the liquid inside the reservoir will be pumped by the pump unit with pre-defined control settings, then flow through the tubing and different types of valves, while the valve model will be fixed inside the tubing.

The manufactured valve phantoms were fixed inside the silicone tubing of the system while these tubes were held in an acrylic box and connected to the reservoir and the pump unit. The pump unit was controlled in terms of desired flow and heart rate: the flow rate was set between 200 and 260 ml/s, and the heart rate was set to 75 bpm. The 4D flow sequences were acquired with a spatial resolution of 1.04–2.08 mm and temporal resolution of 20–60 ms.

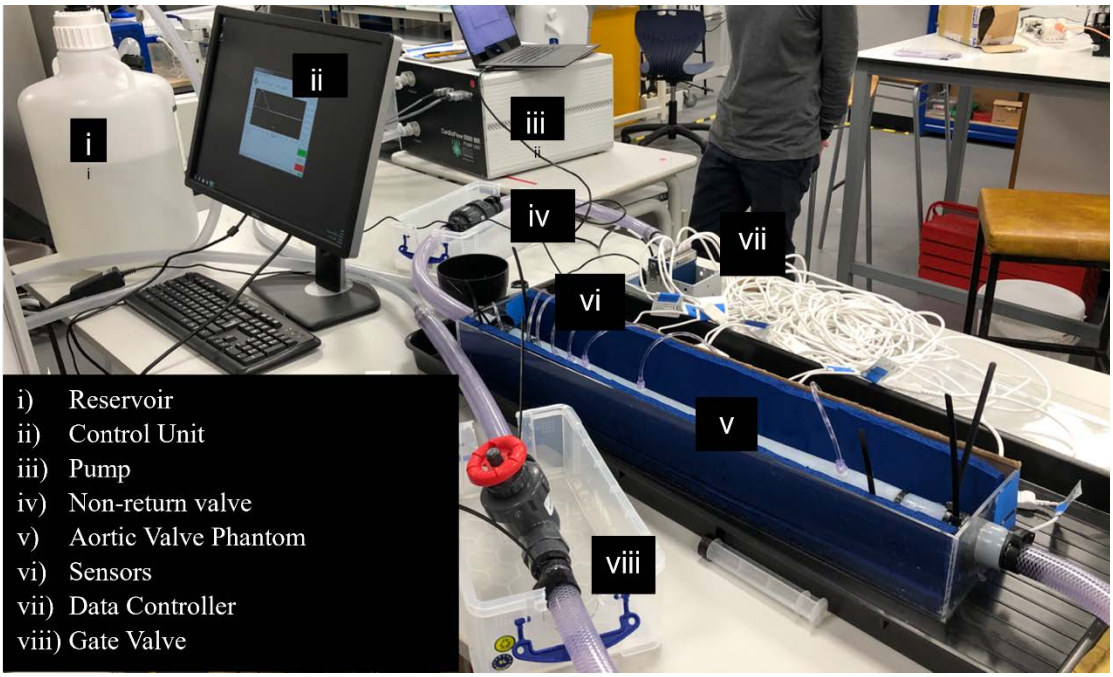

Figure 6.23. Schematic diagram of the phantom circuits and flow system set-up, with component parts listed in legend, the aortic valve models could be inserted inside tubing as shown in (v)

The four valve types with different levels of pathology were compared in terms of systolic peak pressure. The pressure data was collected from the locations shown in figure 6.24: ascending aorta (AA1, AA2, AA3), left ventricle outflow tract (LVOT1, LVOT2) and valve cusps. From table 6.2, it can be observed that the normal valve had the lowest peak-pressure drop at 17 mm Hg, while the stenotic valve had the highest peak pressure of 92 mm Hg.

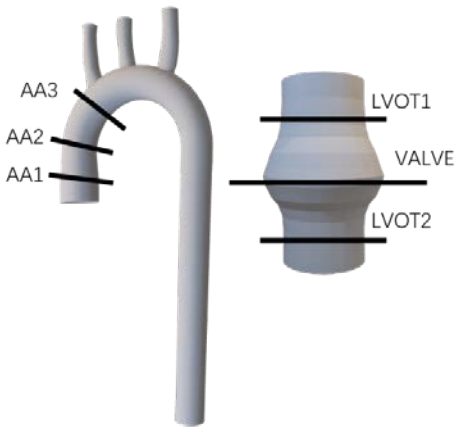

Figure 6.24. Location description of the aorta and valve phantom to measure systolic pressure.

Table 6.2. Systolic pressure measurement

Valve Type	AA3 (mm Hg)	AA2 (mm Hg)	AA1 (mm Hg)	LVOT 1 (mm Hg)	LVOT (mm Hg)	Peak Pressure (mm Hg)
Normal	141	138	133	150	147	17
Rheumatic	135	133	133	155	153	22
Bicuspid	148	143	144	170	168	27
Stenotic	118	119	120	210	209	92

6.5 Discussion

From the practical printing experience and visual inspection of Layfomm40 cardiac models, they suffered from the problem of delamination after rinsing, thus, Layfomm40 is not durable to withstand physiological flow and pumping. Based on the mechanical characterisation results in chapter 3, silicone is an optimal material with enough compliance, flexibility and durability, so silicone elastomer was chosen to make the

aorta and aortic valve models, and the manufacturing technique evolved from two-part moulding method to direct silicone printing method.

The results in figure 6.3 show the limitation of traditional one-part moulding technique, the hollow PVA mould contained many support materials inside the crannies, which blocked the silicone liquids during injection, once the silicone valve model cured and removed from the one-part mould, holes and coarse surface could be observed from the valve appearance. Figure 6.5 (b) demonstrates the silicone valve fabricated using two-part moulds, as the moulds are printed separately, the support materials could be removed before assembling, the clear cavity made the silicone injection flow smoothly and the valve model cured properly after mould dissolving. By comparing the two versions of the valve, the two-part moulded silicone valve is more exquisite than the one-part moulded valve in figure 6.5 (a), and this two-part moulding method could be also applied in the aorta model manufacturing.

The other three types of pathological aortic valves were manufactured based on the normal valve as shown in figure 6.6 by modifying the valve cusps. From the visual inspection (figure 6.6) & imaging results (figure 6.21) of the four valves, it can be seen that the normal valve could open fully under pressure with main jet located centrally, while the rheumatic valve only opens partially with a narrowed jet through the reduced-size orifice, as the leaflets sticked to each other; the calcified valve could barely open due to the abnormal thickness of the leaflets with needle-like jet flowing through it, and the bicuspid valve demonstrates unilateral restriction with incomplete opening and an eccentric jet. The opening and closing circumstances of the silicone valves match the actual situations of corresponding aortic stenosis on real patient, that the scar tissue on the aortic valve will narrow the valve opening, the calcium deposits on the leaflets will create a rough surface and reduce the blood flow [123].

Then, from the comparison between the moulded valve and directly printed valve,

conclusion can be drawn that as an alternative technique to fabricating medical-grade silicone models, silicone printing could simplify the manufacturing procedure without extra moulds design while there is minimal change in the product's quality, both silicone valve models could survive in the dynamic flow experiment under ultrasound imaging monitoring.

The functions of the silicone valve models were validated in terms of ultrasound & MRI-imaging, as well as further pressure analysis. The ultrasound and MRI-imaging compatibility of the silicone models were proven in section 6.4.1. On the other hand, the 3 disease aortic valve models did show the expected characteristics of narrower ejection jets from the ultrasound and MRI images in figure 6.21.

The following discussion about the use of the silicone valves in haemodynamic simulation was based on the pressure results in the recently published journal paper of our collaborator Harminder Gill:

Gill, H., Fernandes, J. F., Nio, A., Dockerill, C., Shah, N., Ahmed, N., Raymond, J., Wang, S., Sotelo, J., Urbina, J., Uribe, S., Rajani, R., Rhode, K., & Lamata, P. (2023). Aortic Stenosis: Haemodynamic benchmark and metric reliability study. *Journal of Cardiovascular Translational Research*. https://doi.org/10.1007/s12265-022-10350-w

These pressure results were collected on the flow circuit setup described in figure 6.23, the circuit consisted of a fabricated valve model, mounted into flexible tubing representative of the aorta, connected to a reservoir and a configurable flow pump.

Even though the in-vivo validation represents the ideal strategy in clinical practice, recruiting patients can be difficult, expensive and time-consuming. Therefore, realistically, in-vitro data acquired from flow phantoms could be one effective solution. The three different stenotic valves were tested on the platform in figure 6.32 and

compared to the normal silicone valve, these phantoms allowed the study of the ultrasound-based blood speckle imaging for a more accurate estimation of the peak pressure drop and the validation of an MRI-based method to estimate the pressure recovery distance.

The systolic pressure results listed in table 6.2 match expected haemodynamic findings, where the point of maximum acceleration, equivalent to the effective orifice area, is more distal to the anatomic orifice in more severe stenoses. These results also demonstrate pressure recovery, best displayed by the normal valve, and the pressure drop observed across the normal aortic valve model on the flow platform is consistent with a non-diseased aortic valve of patients: A peak velocity of >2.5m/s provides evidence to support a diagnosis, which equates to a pressure drop of 25mmHg by application of the Bernoulli equation [122]. Within our range of simulated flow rates, the instantaneous peak pressure drop remains a maximum of 24.1mmHg, indicating the success in recreating a non-pathological aortic valve. Reassuringly, this high degree of reproducibility was maintained amongst two different identical silicone valves (correlation between control with valve X vs valve Y R^2 =. 0.995, calculated from both instantaneous peak pressure drop data in figure 6.25), highlighting the consistency of valve fabrication.

The size and pressure gradient of our silicone valve model are also comparable to the commercial prosthetic valves. The diameter of the valve model shown in figure 6.5 (b) is 28.5mm, while the ADIAM (ADIAM Life Science AG) polycarbonate urethane (PCU) valve size is 29 mm [124], the St Jude Medical (SJM) standard valve size is between 19-27 mm, and the SJM Biocor valve size is between 21-27 mm [125]. The pressure gradient data collected on the normal silicone valve (provided by Harminder Gill) is 25 mmHg, this result is also close to the gradient (around 8 to 22 mmHg) of most mechanical heart valves (MHV) [126], as well as the gradient of a normally functioning (albeit mildly stenotic) natural valve [127]. However, the blood

compatibility and thrombogenicity need to be confirmed with further investigation of the silicone valve before using it as a new prosthetic valve type.

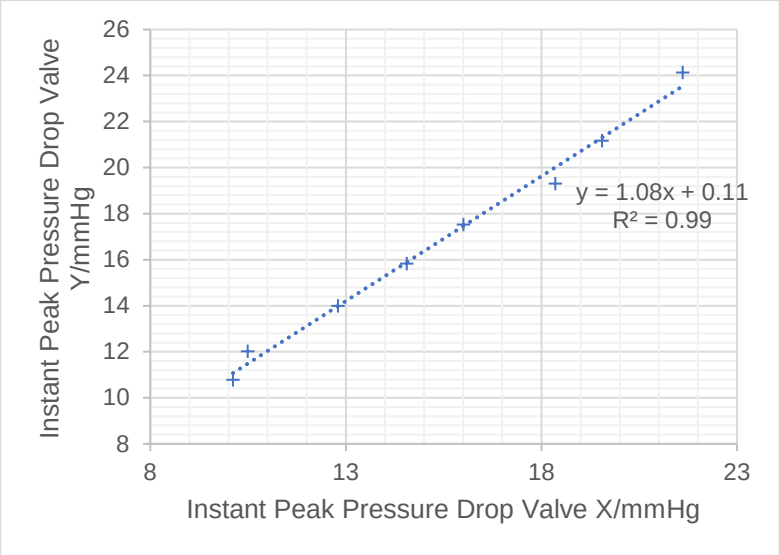

Figure 6.25. The instantaneous peak pressure drop/mmHg compared to the replacement of valve X with valve Y

6.6 Conclusion

As explained in the previous chapter, Layfomm40 and Tango Plus were not suitable to make a durable aorta or valve model, thus, this chapter introduces two effective silicone phantom manufacturing techniques for valvular interventional procedure simulation: two-part moulding & silicone printing, both techniques could produce silicone models durable enough for dynamic flow testing, while these silicone models with complicated and hollow structures cannot be made via traditional one-part moulding method. From the visual inspection results, the silicone models demonstrate plausible valve opening and closing both in healthy and pathological conditions. The fabricated silicone models are also comparable with real patient ones– from both ultrasound& MRI images.

Additionally, the flow testing on the normal silicone valve and different pathological silicone valves provides a reliable solution to obtaining the ground-truth pressure measurement. Catheterized fluid-filled pressure sensors and pressure wires, used in-vivo, display important limitations. Unlike the in-vivo experiments, which are limited by the need to interpolate along the length of the vessel to estimate the instantaneous peak pressure drop, the silicone valves manufactured in this chapter could be used for direct pressure transduction from sensors in the phantom wall in-vitro and tested for control and reproducibility.

In conclusion, the aorta & valve models described in chapter 6 first successfully pass the visual inspection in terms of sizes and anatomical appearances, meanwhile, the valve model fabricated using direct silicone printing keeps the durability under flow as the moulded one. In the functional experiments, the ultrasound & MRI-imaging comparisons between the normal valve and pathological valves demonstrate the phantoms' medical imaging compatibility as well as expected valve opening and closing performances, further hemodynamic analysis proves that the transvalvular pressure gradient of the silicone valve is comparable to natural & commercial prosthetic valves, which expands the silicone models' applications from in-vitro simulation to potential implantation in the future.

7. CONCLUSIONS & FUTURE WORK

7.1 Chapter Summaries and Thesis Conclusions

As mentioned in the beginning of the thesis, the overall theme of the work presented is using 3D printing to make anthropomorphic cardiac phantoms with soft materials. These soft materials, including Layfomm40 and silicones, could demonstrate tissue-mimicking properties in terms of flexibility, ultrasound acoustic property, etc. And the fabricated cardiac phantoms in chapter 4-6 also satisfy the functional needs in different simulation procedures, such as medical imaging, ablation, and pulsatile flow. Safety risks related to the engineering methods are low. As no animals or patients involved in listed experiments, ethical approval is not required, but the strong connection to cardiology research does encourage future clinical trainings.

From the characterisation results of the soft materials mainly used in the thesis, major findings of Layfomm40 as a 3D printable material were summarized in chapter 3, that it has the closest Young's modulus value (128.5 kPa) to real myocardium with a difference of 28.6%–54% when compared to other 3D printable materials, and it also has close ultrasound acoustic properties and thermal conductivities to biological tissue, the porous structure created after rinsing makes its application in further tissue engineering become possible.

Meanwhile, the successful fabrications of ultrasound compatible whole cardiac models, thermochromic bi-atrial models and silicone aorta and valve models could demonstrate anatomical similarities to real heart, with different functional successes validated using corresponding clinical systems. Separate chapter summaries are presented in the following subsections 7.1.1-7.1.3:

7.1.1 Directly 3D Printed Ultrasound Compatible Cardiac Phantom

Chapter 4 makes an initial investigation for engineering ultrasound compatible cardiac phantoms using directly 3D printing.

At present, all 3D printable elastomers have low flexibility with minimum Shore A hardness of 30 HA that the ultrasound wave cannot easily penetrate. Other ultrasound compatible materials with high flexibility cannot be printed using current printing techniques, especially when the model has complicated geometries, such as cardiac phantoms. The fabrication idea of chapter 4 to solve the problems is to use rigid printable material—Layfomm40 and soften it afterwards. Layfomm40, with the highest flexibility and closest ultrasound velocity and attenuation to myocardium, was chosen as the most ultrasound-compatible 3D printable material. A 3D cardiac model was first segmented from an adult chest CT scan and then printed directly with Layfomm40, while another Tango Plus cardiac phantom was also printed for comparison. In addition to ultrasound imaging, both cardiac phantoms were validated under X-ray, CT and MRI imaging modalities. The cardiac outer and inner structures were clearly visible from these imaging results.

7.1.2 Thermochromic Bi-atrial Model for Ablation Simulation

As mentioned in chapter 4, Layfomm40 was utilised as a promising soft tissue-mimicking material for making anatomical phantoms. Layfomm40's absorption properties make it the ideal choice for constructing functional models as it absorbs saline water, colour changing pigments and other liquids simultaneously, chapter 5 describes Layfomm40's further use in thermochromic bi-atrial model fabrication for ablation simulations.

Unlike previous models that only required imaging compatibility, the bi-atrial model

constructed in chapter 5 has to be thermally and electrically conductive as well to work with the radiofrequency system and heat-responsive so that the ablated mark would remain afterwards. The bi-atrial model was coated with irreversible thermochromic pigments with permanent colour-changing effects. The transition temperature was 44℃, just between the water and the ablation temperatures, ensuring that the colour-changing conditions were satisfied. The model detailed the superior vena cava, the inferior vena cava and the left and right atria. Before printing, the Layfomm40 sample was immersed in saline water, and the colour-changing coating was tested with the RF ablation system and compared to chicken breast tissue. The comparison results showed that similar marks were evident on the Layfomm40 sample as those produced on real tissue. Finally, the bi-atrial model was printed with Layfomm40 and assembled inside the water tank with a holding base and silicone tubes. Monitoring of the interventional procedure took place using ultrasound imaging and the CARTO3 mapping system.

7.1.3 Ultrasound and MRI-compatible Silicone Aorta & Valve Models

In order to find and simulate the optimal treatment for aortic valve stenosis, valve model compatible with ultrasound and MRI with durability for pulsatile flow was required. As Layfomm40 is porous and easily delaminated under external force, it is not strong enough to withstand the dynamic flow environment. Compared to all 3D printable and non-3D printable materials, silicone elastomers outperform others, with a wide range of flexibility, high durability and multi-modal imaging compatibility.

Thus, a two-part moulding technique with separable internal and external moulds was applied first to make the silicone aorta and valves in chapter 6. The external mould was printed with PLA for reuse, and the internal one was printed with water-soluble PVA material, allowing it to be easily removed. The Ecoflex 0030 silicone cured inside the mould to construct a detailed complete aortic valve with three cuspids. The aorta model was also created with a stiffer silicone (Dragonskin 10) using the same technique. The

valve's opening and closing under the pulsatile flow was monitored under ultrasound and MRI imaging modalities, and further hemodynamic analysis proves that the transvalvular pressure gradient of the silicone valve (~25 mmHg) is comparable to natural & commercial prosthetic valves, which expands the silicone models' applications from in-vitro simulation to potential implantation in the future.

Additionally, chapter 6 also demonstrated the silicone printer's capability in aortic valve's development. Sophisticated non-mouldable silicone models are now printable using this technology, while the durability and flexibility of the model can be maintained.

7.2 Current Limitations and Future Work

As described in the title, the work presented in the thesis did demonstrate the success in making different functional anthropomorphic cardiac phantoms. However, theses cardiac phantoms haven't been tested with a trial with patients. Meanwhile, the phantom materials' biocompatibility and thrombogenicity still remain to be tested. There is still a long way to go from interventional simulations to actual clinical translations for engineered cardiac phantoms.

One direction of the future research could be in-vitro cell co-culturing with these materials, if they are tested to be biocompatible, the next step work is to use them for organoids [112] manufacturing, possible applications in effective therapeutic drug delivery [128] could be combined during relevant experiments. Another future work direction is when they are less likely to be used on patients directly, fabricated phantoms could be used during the pre-surgical planning where patients will be involved as well, treatments between the patients with and without the pre-surgical planning shall be analysed and compared to show the impact of these phantoms. Moreover, further improvements of the Layfomm40 cardiac phantoms are still required as they limit in

poor printing accuracy and durability from presented results in the thesis, one solution could be optimising the material qualities by coatings or mixing with polymers.

REFERENCES:

[1] Ngo, T. D., Kashani, A., Imbalzano, G., Nguyen, K. T. Q., & Hui, D. (2018). Additive manufacturing (3D printing): A review of materials, methods, applications and challenges. *Composites Part B: Engineering*, 143, 172–196. https://doi.org/https://doi.org/10.1016/j.compositesb.2018.02.012

[2] Imes, C. C., & Lewis, F. M. (2014). Family history of cardiovascular disease perceived cardiovascular disease risk, and health-related behavior: a review of the literature. *The Journal of cardiovascular nursing*, 29(2), 108–129. https://doi.org/10.1097/JCN.0b013e31827db5eb

[3] Carr, J. G. (2020). Cardiac interventions in the office interventional suite. *Office-Based Endovascular Centers*, 287–298. https://doi.org/10.1016/b978-0-323-67969-5.00035-6

[4] Xu, T., Shen, W., Lin, X., & Xie, Y. M. (2020). Mechanical properties of additively manufactured thermoplastic polyurethane (TPU) material affected by various processing parameters. *Polymers*, 12(12), 3010. https://doi.org/10.3390/polym12123010

[5] Pagac, M., Hajnys, J., Ma, Q.-P., Jancar, L., Jansa, J., Stefek, P., & Mesicek, J. (2021). A review of VAT photopolymerization technology: Materials, applications, challenges, and future trends of 3D printing. *Polymers*, 13(4), 598. https://doi.org/10.3390/polym13040598

[6] Laing, J., Moore, J., Vassallo, R., Bainbridge, D., Drangova, M., & Peters, T. (2018). Patient-specific cardiac phantom for clinical training and pre-procedure surgical planning. *Journal of medical imaging (Bellingham, Wash.), 5(2)*, 021222. https://doi.org/10.1117/1.JMI.5.2.021222

[7] Byrne N, Velasco Forte. (2016). A systematic review of image segmentation methodology used in the additive manufacture of patient-specific 3D printed models of the cardiovascular system. *JRSM Cardiovasc Dis*, vol 5. https://doi.org/10.1177/2048004016645467

[8] Luciana C Cabrelli, Pedro I B G.B Pelissari, et al. (2017). Stable phantom materials for ultrasound and optical imaging. *Phys. Med. Biol. 62(2)*:432–447.

[9] Talvenmaa, P. (2006). Introduction to chromic materials. *Intelligent Textiles and Clothing*, 193–205. https://doi.org/10.1533/9781845691622.3.193

[10] Ahmadi, Z., Chauhan, N. P., Zarrintaj, P., Khiabani, A. B., Saeb, M. R., & Mozafari, M. (2019). Experimental procedures for assessing electrical and thermal conductivity of polyaniline. *Fundamentals and Emerging Applications of Polyaniline*, 227–258. https://doi.org/10.1016/b978-0-12-817915-4.00013-0

[11] Motlogelwa, S. (2018). Comfort and durability in high-performance clothing. *High-Performance Apparel*, 209–219. https://doi.org/10.1016/b978-0-08-100904-8.00012-2

[12] Yirmibesoglu, O. D., Morrow, J., Walker, S., Gosrich, W., Cañizares, R., Kim, H., Daalkhaijav, U., Fleming, C., Branyan, C., & Menguc, Y. (2018). Direct 3D printing of silicone elastomer soft robots and their performance comparison with molded counterparts. *2018 IEEE International Conference on Soft Robotics* (RoboSoft), Livorno, Italy, 295–302. doi:10.1109/ROBOSOFT.2018.8404935

[13] Bryce, Douglas M. (1996). Plastic injection moulding: manufacturing process fundamentals. *SME*

[14] Abtan, A. A., Richardson, R. C., & Thomas, B. (2016). Analyzing the 3D printed material Tango Plus FLX930 for using in self-folding structure. *2016 International Conference for Students on Applied Engineering (ISCAE)*. https://doi.org/10.1109/icsae.2016.7810171

[15] Gent, A. N. (1958). On the relation between indentation hardness and Young's modulus. *Transactions of the Institute of the Rubber Industry, 34*(2), 896–906. https://doi.org/10.5254/1.3542351

[16] Qiu, K., Haghiashtiani, G., & McAlpine, M. C. (2018). 3D printed organ models for surgical applications. *Annual Review of Analytical Chemistry*, 11(1), 287–306. https://doi.org/10.1146/annurev-anchem-061417-125935
[17] Tejo-Otero, A., Fenollosa-Artés, F., Achaerandio, I., Rey-Vinolas, S., Buj-Corral, I., Mateos-Timoneda, M. Á., & Engel, E. (2022). Soft-tissue-mimicking using hydrogels for the development of phantoms. *Gels*, 8(1), 40. https://doi.org/10.3390/gels8010040
[18] Mohammadi, H., Bahramian, F., & Wan, W. (2009). Advanced modeling strategy for the analysis of heart valve leaflet tissue mechanics using high-order finite element method. *Medical Engineering and Physics*, *31*(9), 1110–1117. https://doi.org/10.1016/j.medengphy.2009.07.012
[19] Piero Tortoli, Francesco Guidi, ULA-OP: An advanced open platform for ultrasound research. *IEEE Transactions on Ultrasonics, Ferroelectrics, And Frequency Control 56 (10)*: 2207–2216.
[20] Ebnesajjad, S. (2014). Surface and material characterization techniques. *Surface Treatment of Materials for Adhesive Bonding*, 39–75. https://doi.org/10.1016/b978-0-323-26435-8.00004-6
[21] Chiu, H.-T., Liu, Y.-L., Lin, C.-W., Shong, Z.-J., & Tsai, P.-A. (2013). Thermal conductivity and electrical conductivity of silicone rubber filled with aluminum nitride and aluminum powder. *Journal of Polymer Engineering*, 33(6), 545–549. https://doi.org/doi:10.1515/polyeng-2013-0025
[22] Roney, C. H., Beach, M. L., Mehta, A. M., Sim, I., Corrado, C., Bendikas, R., Solis-Lemus, J. A., Razeghi, O., Whitaker, J., O'Neill, L., Plank, G., Vigmond, E., Williams, S. E., O'Neill, M. D., & Niederer, S. A. (2020). In silico comparison of left atrial ablation techniques that target the anatomical, structural, and electrical substrates of atrial fibrillation. *Frontiers in Physiology*, 11, 1145. https://doi.org/10.3389/fphys.2020.572874
[23]*Thermal Conductivity » IT'IS Foundation*. https://itis.swiss/virtual-population/tissue-properties/database/thermal-conductivity/
[24] Abraham, J., Sharika, T., Mishra, R. K., & Thomas, S. (2017). Rheological characteristics of nanomaterials and nanocomposites. *Micro and Nano Fibrillar Composites (MFCs and NFCs) from Polymer Blends*, 327–350. https://doi.org/10.1016/b978-0-08-101991-7.00014-5
[25] Nagaraju, L, D Menon, & Aziz, P. F. (2016). Use of 3D electroanatomical navigation (CARTO3) to minimize or eliminate fluoroscopy use in the ablation of pediatric supraventricular tachyarrhythmias. *Pacing Clin Electrophysiol*, 39(6), 574-580.
[26] Shahrubudin, N., Lee, T. C., & Ramlan, R. (2019). An overview on 3D printing technology: Technological, materials, and applications. Procedia Manufacturing, 35, 1286–1296. https://doi.org/10.1016/j.promfg.2019.06.089
[27]*Types of 3D printing technology explained*. (2018). Protolabs. https://www.protolabs.com/resources/blog/types-of-3d-printing/
[28] Jain, A., Bansal, K., Tiwari, A., Rosling, A., & Rosenholm, J. (2018). Role of polymers in 3D printing technology for drug delivery - an overview. *Current Pharmaceutical Design*, 25. https://doi.org/10.2174/1381612825666181226160040
[29] Dudek, P. (2013). FDM 3D printing technology in manufacturing composite elements. *Archives of Metallurgy and Materials*, 58(4), 1415–1418. https://doi.org/10.2478/amm-2013-0186
[30] Kumar, P., Ebbens, S., & Zhao, X. (2021). Inkjet printing of mammalian cells – Theory and applications. *Bioprinting*, *23*, e00157. https://doi.org/10.1016/j.bprint.2021.e00157
[31] *Apparatus for production of three-dimensional objects by stereolithography*. (1986). U.S. Patent 4,575,330.
[32] *Stereolithography (SLA) 3D Printing Guide*. (2018). Formlabs.

[33] M., P. (2020). Additive manufacturing of tungsten carbide hardmetal parts by selective laser melting (SLM), Selective Laser Sintering (SLS) and Binder Jet 3D printing (BJ3DP) techniques. *Lasers in Manufacturing and Materials Processing*, 7(3), 338–371. https://doi.org/10.1007/s40516-020-00124-0
[34] Hassan, P. A., Verma, G., & Ganguly, R. (2012). Soft materials — properties and applications. *Functional Materials*, 1–59. https://doi.org/10.1016/b978-0-12-385142-0.00001-5
[35] Gu Fu; Li Renwang; (2019). Preliminary study on soft material processing engineering. *Group Technology & Production Modernisation.* 36(4), 12-19.
[36] Trimmer, Barry, Jennifer A. Lewis, Robert F. Shepherd, and Hod Lipson. (2015). 3D printing soft materials: what is possible? *Soft Robotics* 2 (1), 3–6. doi:10.1089/soro.2015.1502.
[37] *TPU 3D Printing: A Guide to 3D Printing Flexible Parts*. AMFG. https://amfg.ai/2018/07/23/tpu-3d-printing-guide/
[38] *Tango: A Soft Flexible 3D Printing Material*. https://www.stratasys.com/en/materials/materials-catalog/polyjet-materials/tango
[39] Stratasys. https://www.stratasys.com/en/materials/materials-catalog/digital-anatomy
[40] Monocure 3D. *Flex Resins*. https://monocure3d.com.au/product-category/resins/flex-resins/
[41] Ge, Q., Sakhaei, A., Lee, H. et al. (2016). Multimaterial 4d printing with tailorable shape memory polymers. *Sci Rep*, 6, 31110. https://doi.org/10.1038/srep31110
[42] *Flexible Filament for 3D Printing: Materials Guide*. (2021, July 12). Jiga. https://jiga.io/resource-center/3d-printing/flexible-filament-for-3d-printing-materials-guide/
[43] Sheffield, S. *Types of Flexible Filament*. MakeShaper. https://www.makeshaper.com/types-of-flexible-filament/
[44] *Introducing Elastic Resin: A Soft, Resilient 3D Printing Material*. (2018). Formlabs. https://formlabs.com/blog/elastic-resin-soft-resilient-3d-printing/
[45] Zheng YX, Yu DF, Zhao JG, Wu YL, Zheng B. (2016). 3D printout models vs. 3D-rendered images: which is better for preoperative planning? *J Surg Educ.* 73:518–23. doi: 10.1016/j.jsurg.2016.01.003.
[46] Fiaschi P, Pavanello M, Imperato A, et al. (2016). Surgical results of cranioplasty with a polymethylmethacrylate customised cranial implant in pediatric patients: a single-center experience. *J Neurosurg Pediatr*. 17:705–10. doi: 10.3171/2015.10. PEDS15489.
[47] Jardini AL, Larosa MA, Maciel Filho R, et al. (2014). Cranial reconstruction: 3D biomodel and custom-built implant created using additive manufacturing. *J Craniomaxillofac Surg*. 42:1877–84. doi: 10.1016/j.jcms.2014.07.006.
[48] Berthiaume, F., & Yarmush, M. L. (2003). Tissue engineering. *Encyclopedia of Physical Science and Technology*, 817–842. https://doi.org/10.1016/b0-12-227410-5/00783-3
[49] Mandrycky, C., Wang, Z., Kim, K., and Kim, D. H. (2016). 3D bioprinting for engineering complex tissues. *Biotechnol. Adv.* 34, 422–434. doi: 10.1016/j.biotechadv.2015.12.011
[50] Xianliang Wu. (2014). Fast catheter segmentation and tracking based on X-ray fluoroscopic and echocardiographic modalities for catheter-based cardiac minimally invasive interventions. PhD Thesis.
[51] Mohen, L. *Ventricular Tachycardia Ablation in Structural Heart Disease*. Melbourne Heart Rhythm.https://www.melbourneheartrhythm.com.au/learn/procedures/49-ventricular-tachycardia-heart-disease?showall=1&limitstart=
[52] Saikus, C. E., & Lederman, R. J. (2009). Interventional cardiovascular magnetic resonance imaging: a new opportunity for image-guided interventions. *JACC. Cardiovascular Imaging*, *2(11*), 1321–1331. https://doi.org/10.1016/j.jcmg.2009.09.002

[53] Bluemke, D. A., & Liu, S. (2012). Chapter 41 - Imaging in clinical trials. *In J. I. Gallin & F. P. B. T.-P. and P. of C. R. (Third E. Ognibene (Eds.)* 597–617. Boston: Academic Press. https://doi.org/https://doi.org/10.1016/B978-0-12-382167-6.00041-2

[54] Silvestry, F. E., Kerber, R. E., Brook, M. M., Carroll, J. D., Eberman, K. M., Goldstein, S. A., Herrmann, H. C., Homma, S., Mehran, R., Packer, D. L., Parisi, A. F., Pulerwitz, T., Seward, J. B., Tsang, T. S., & Wood, M. A. (2009). Echocardiography-guided interventions. *Journal of the American Society of Echocardiography*, *22*(3), 213–231. https://doi.org/10.1016/j.echo.2008.12.013

[55] Schussler J.M. (2016) Cardiovascular CT: interventional cardiology applications. In: Budoff M., Shinbane J. (eds) *Cardiac CT Imaging. Springer, Cham.* https://doi.org/10.1007/978-3-319-28219-0_25

[56] Schoepf, U. J., Suranyi, P., Thilo, C., Costello, P., & Zwerner, P. L. (2007). Replacing diagnostic catheterisation with coronary CT angiography: the final frontier. *European Heart Journal, 28(19)*, 2305–2306. https://doi.org/10.1093/eurheartj/ehm348

[57] Rao, S. C. (2011). Coronary CT angiography as an alternative to invasive coronary angiography. *In R. C. T. E.-B. Baskot (Ed.)*. Rijeka: IntechOpen. https://doi.org/10.5772/21191

[58] Jongbloed, M. R. M. (2005). Clinical applications of intracardiac echocardiography in interventional procedures. *Heart*, *91*(7), 981–990. https://doi.org/10.1136/hrt.2004.050443

[59] McGarry, C. K., Grattan, L. J., Ivory, A. M., Leek, F., Liney, G. P., Liu, Y., Miloro, P., Rai, R., Robinson, A. P., Shih, A. J., Zeqiri, B., & Clark, C. H. (2020). Tissue mimicking materials for imaging and therapy phantoms: A review. *Physics in Medicine and Biology*, 65(23). https://doi.org/10.1088/1361-6560/abbd17

[60] Browne J, Ramnarine K, Watson A, et al. (2003). Assessment of the acoustic properties of common tissue-mimicking test phantoms. *Ultrasound Med. Biol. 29:* 1053–1060.

[61] Madsen E L, Zagzebski J A, Banjavie R. (1978). A 'tissue mimicking' materials for ultrasound phantoms. *Med. Phys.5*:391–394.

[62] Kondo T, Kitatuji M, Kanda H. (2005). New 'tissue mimicking' materials for ultrasound phantoms. *Ultrasonics Symp*: 1664–1667.

[63] Wagnières G. (1997). An optical phantom with tissue-like properties in the visible for use. *Med. Biol. 42*: 1415.

[64] Spirou G M, Oraevsky A, Vitkin I A, Whelan W M. (2005) Acoustic properties at 1064 nm of polyvinyl chloride-plastisol for use as a tissue phantom. *Phys. Med. Biol. 50*: 141.

[65] Cook, J. R., Bouchard, R. R., & Emelianov, S. Y. (2011). Tissue-mimicking phantoms for photoacoustic and ultrasonic imaging. *Biomedical Optics Express, 2(11)*, 3193–3206. https://doi.org/10.1364/BOE.2.003193

[66] Villa, E., Arteaga-Marrero, N., González-Fernández, J., & Ruiz-Alzola, J. (2020). Bimodal microwave and ultrasound phantoms for non-invasive clinical imaging. *Scientific Reports, 10(1)*, 20401. https://doi.org/10.1038/s41598-020-77368-5

[67] Efthymios Maneas, Wenfeng Xia, Daniil I Nikitichev, et al. (2018). Anatomically realistic ultrasound phantoms using gel wax with 3D printed moulds. *Phys. Med. Biol. 63*:1–10.

[68] Marija Vukicevic, Bobak Mosadegh, James K Min, et al. (2017). Cardiac 3D printing and its future directions. *Cardiovascular Imaging. 10*:171–184.

[69] Hill KD, Wang C, Einstein AJ, et al. (2017). Impact of imaging approach on radiation dose and associated cancer risk in children undergoing cardiac catheterisation. *Catheter Cardiovasc Interv. 89*: 888–897.

[70] Rizzo G, Capponi A, Pietrolucci ME,et al. (2010). Role of sonographic automatic volume calculation in measuring fetal cardiac ventricular volumes using 4-dimensional sonography: comparison with virtual organ computer-aided analysis. *J Ultrasound Med. 29*:261–270.
[71] Ramalli A., A. Dallai, E Boni, et al. (2016). Multi transmit beams for fast cardiac imaging towards clinical routine. *IEEE International Ultrasonics Symposium (IUS)*. 978–981.
[72] Laing, J., Moore, J., Vassallo, R., Bainbridge, D., Drangova, M., & Peters, T. (2018). Patient-specific cardiac phantom for clinical training and pre-procedure surgical planning. *Journal of medical imaging (Bellingham, Wash.), 5(2),* 021222. https://doi.org/10.1117/1.JMI.5.2.021222
[73] Earley, M. J. (2006). Catheter and surgical ablation of atrial fibrillation. *Heart*, 92(2), 266–274. https://doi.org/10.1136/hrt.2005.067389
[74] Liu, X., Shi, H., Zheng, J., Li, K., Zhao, X., Dang, S., Wu, Y., Cheng, Y., Li, X., Yu, Z., & Wang, R. (2018). The impact of left atrial size in catheter ablation of atrial fibrillation using remote magnetic navigation. *Cardiology Research and Practice*, 2018, 3096261. https://doi.org/10.1155/2018/3096261
[75] Caponi, D., Corleto, A., Scaglione, M., Blandino, A., Biasco, L., Cristoforetti, Y., Cerrato, N., Toso, E., Morello, M., & Gaita, F. (2010). Ablation of atrial fibrillation: does the addition of three-dimensional magnetic resonance imaging of the left atrium to electroanatomic mapping improve the clinical outcome? a randomised comparison of CARTO3-Merge Vs. CARTO3-XP three-dimensional mapping ablation in patients with paroxysmal and persistent atrial fibrillation. *EP Europace*, 12(8), 1098–1104. https://doi.org/10.1093/europace/euq107
[76] Roney, C. H., Beach, M. L., Mehta, A. M., Sim, I., Corrado, C., Bendikas, R., Solis-Lemus, J. A., Razeghi, O., Whitaker, J., O'Neill, L., Plank, G., Vigmond, E., Williams, S. E., O'Neill, M. D., & Niederer, S. A. (2020). In silico comparison of left atrial ablation techniques that target the anatomical, structural, and electrical substrates of atrial fibrillation. *Frontiers in Physiology*, 11, 1145. https://doi.org/10.3389/fphys.2020.572874
[77] Gong Y, Gao Y, Lu Z, Zheng D, Deng D, et al. (2015) Preliminary simulation study of atrial fibrillation treatment procedure based on a detailed human atrial model. *J Clin Trial Cardiol* 2(4): 1-9. DOI: http://dx.doi.org/10.15226/2374-6882/2/4/00130
[78] Haleem, A., Javaid, M., & Saxena, A. (2018). Additive manufacturing applications in cardiology: a review. *The Egyptian Heart Journal*, 70(4), 433–441. https://doi.org/https://doi.org/10.1016/j.ehj.2018.09.008
[79] Biglino, G. (2016). 3D printing cardiovascular anatomy: a single-centre experience (C. Capelli (ed.); p. Ch. 6). *IntechOpen.* https://doi.org/10.5772/63411
[80] Le Bras, A. (2018). 3D printing of personalised implants for left atrial appendage occlusion. *Nature Reviews Cardiology*, 15(3), 134. https://doi.org/10.1038/nrcardio.2018.1
[81] Baki, P., Sanabria, S. J., Kosa, G., Szekely, G., & Goksel, O. (2015). Thermal expansion imaging for monitoring lesion depth using M-mode ultrasound during cardiac RF ablation: in vitro study. *International Journal of Computer Assisted Radiology and Surgery*, 10(6), 681–693. https://doi.org/10.1007/s11548-015-1203-4
[82]Vaquerizo B, Escabias C, Dubois D, Gómez G, Barreiro-Pérez M, Cruz-González I. Patient-specific 3D-printed cardiac model for percutaneous left atrial appendage occlusion. *Rev Esp Cardiol (Engl Ed).* 2018 Sep;71(9):762-764. English, Spanish. doi: 10.1016/j.rec.2017.05.028.
[83] *3D Printed Model of the left Atrium to Plan Atrial Appendage Closure in Challenging Anatomy*. 3D4MED. https://www.3d4med.eu/3d-printed-model-of-the-left-atrium-to-plan-atrial-appendage-closure-in-challenging-anatomy/

[84] *Aortic Dissection: A Rare, Dangerous Condition That Can Mimic a Heart Attack.* (2017, October 26). The Society for Cardiovascular Angiography and Interventions. http://www.secondscount.org/heart-condition-centers/info-detail-2/aortic-dissectionbra-rare-dangerous-condition-that#.YpxTx-xBxPY

[85] University of Minnesota. (2020, September 2). *Researchers 3D print lifelike heart valve models*. https://twin-cities.umn.edu/news-events/researchers-3d-print-lifelike-heart-valve-models

[86] Fortini, L., Boll, C., Rodrigues, G. O., Rodrigues, C. G., Bertollo, F. L., Irigoyen, M. C., & Goldmeier, S. (2019). Using a 3D printer in cardiac valve surgery: a systematic review. 65(51), 818–824.

[87] Coulter, F. B., Schaffner, M., Faber, J. A., Rafsanjani, A., Smith, R., Appa, H., Zilla, P., Bezuidenhout, D., & Studart, A. R. (2019). Bioinspired heart valve prosthesis made by silicone *Additive Manufacturing*. *Matter*, 1(1), 266–279. https://doi.org/10.1016/j.matt.2019.05.013

[88]*How 3D Printing Helps Save Patients With Aortic Aneurysms.* Formlabs. https://formlabs.com/blog/3d-printing-saves-aortic-aneurysms-patients/

[89] Baumgartner Huang. (2017). Recommendations on the echocardiographic assessment of aortic valve stenosis: a focused update from the European association of cardiovascular imaging and the American society of echocardiography, *Eur Heart J Cardiovasc Imaging*, vol 18(3): 254-275. https://doi.org/10.1016/j.echo.2017.02.009

[90]*Virtual Transoesophageal Echocardiography*. http://pie.med.utoronto.ca/TEE/TEE_content/TEE_spectral_intro.html

[91] Tuncay, V., van Ooijen, P.M.A. (2019). 3D printing for heart valve disease: a systematic review. *Eur Radiol Exp* 3, 9. https://doi.org/10.1186/s41747-018-0083-0

[92] Gardin, C. , Ferroni, L. , Latremouille, C. , Chachques, J. C. , & Zavan, B. . (2020). Recent applications of three-dimensional printing in cardiovascular medicine. *Cells*, 9(3), 742. https://doi.org/10.3390/cells9030742

[93] G. Haghiashtiani, K. Qiu, J.D.Z. Sanchez, Z.J. Fuenning, P. Nair, S.E. Ahlberg, P. A. Iaizzo, M.C. Mcalpine. (2020). 3D printed patient-specific aortic root models with internal sensors for minimally invasive applications, *Sci. Adv.* 6. https://doi.org/10.1126/sciadv.abb4641

[94] Ilina, A., Lasso, A., Jolley, M. A., Wohler, B., Nguyen, A., Scanlan, A., Baum, Z., McGowan, F., & Fichtinger, G. (2017). Patient-specific pediatric silicone heart valve models based on 3D ultrasound. *Proceedings of SPIE--the International Society for Optical Engineering*, 10135, 10.1117/12.2255849. https://doi.org/10.1117/12.2255849

[95]Jastrzebski, D. (1959). Nature and Properties of Engineering Materials. *Wiley International ed.* John Wiley & Sons, Inc.

[96] Gao, F., Guo, Z., Sakamoto, M., & Matsuzawa, T. (2006). Fluid-structure interaction within a layered aortic arch model. *Journal of Biological Physics*, 32(5), 435–454. https://doi.org/10.1007/s10867-006-9027-7

[97] Zweben, C., W. S. Smith, and M. W. Wardle. (1979). Test methods for fibre tensile strength, composite flexural modulus, and properties of fabric-reinforced laminates, *Composite Materials: Testing and Design (Fifth Conference), ASTM International*. https://doi.org/10.1520/STP36912S

[98] Licari, J. J., & Swanson, D. W. (2011). Adhesive technology for electronic applications *William Andrew Publishing*. 1–34. https://doi.org/https://doi.org/10.1016/B978-1-4377-7889-2.10001-4

[99] Wu, C., Li, J., & Su, Y. (2018). Development, testing, and numerical simulation of ultra-high-performance concrete at material level. Woodhead publishing series in civil and structural engineering. *Woodhead Publishing*. 23-93. https://doi.org/https://doi.org/10.1016/B978-0-08-102495-9.00002-5

[100] Mikko A Hakulinen. Ultrasound transmission technique as a potential tool for physical evaluation of monolithic matrix tablets. *AAPS PharmSciTech 9(1):*267–73.

[101] Laugier, P., & Haïat, G. (2010). Introduction to the physics of ultrasound. *Bone Quantitative Ultrasound*, 29–45. https://doi.org/10.1007/978-94-007-0017-8_2

[102] Folds, D. L. (1974). Speed of sound and transmission loss in silicone rubbers at ultrasonic frequencies. The Journal of the Acoustical Society of America, 56(4), 1295–1296. https://doi.org/10.1121/1.1903422

[103]Fu, F., & Hu, L. (2017). Temperature sensitive colour-changed composites. *Advanced High Strength Natural Fibre Composites in Construction*, 405–423. https://doi.org/10.1016/b978-0-08-100411-1.00015-7

[104] Raghavan, K., Porterfield, J. E., Kottam, A. T. G., Feldman, M. D., Escobedo, D., Valvano, J. W., & Pearce, J. A. (2009). Electrical conductivity and permittivity of murine myocardium. I*EEE Transactions on Bio-Medical Engineering*, 56(8), 2044–2053. https://doi.org/10.1109/TBME.2009.2012401

[105] Barnes, H. A. (2000). Handbook of elementary rheology. *Institute of Non-Newtonian Fluid Mechanics*, University of Wales.

[106] Li, W., Belmont, B., Greve, J. M., Manders, A. B., Downey, B. C., Zhang, X., Xu, Z., Guo, D., & Shih, A. (2016). Polyvinyl chloride as a multimodal tissue-mimicking material with tuned mechanical and medical imaging properties. *Medical Physics*, 43(10), 5577–5592. https://doi.org/10.1118/1.4962649

[107] Tavakoli, V., Negahdar, M. J., Kendrick, M., Alshaher, M., Stoddard, M., & Amini, A. A. (2012). A Biventricular multimodal (mri/ultrasound) cardiac phantom. *In 2012 Annual International Conference of the IEEE Engineering in Medicine and Biology Society*. 3187–3190. https://doi.org/10.1109/EMBC.2012.6346642

[108] Peter Kellman, Michael S Hansen. (2014). T1-Mapping in the heart: accuracy and precision. *Journal of Cardiovascular Magnetic Resonance. 16 (2)*: 1–20.

[109] S.Giri, You-Cho Chung, et al. (2009). T2 quantification for improved detection of myocardial edema. *Journal of Cardiovascular Magnetic Resonance.11*: 1–13.

[110] Myer, W. (1977). Radiography review: radiographic density. *Veterinary Radiology*, 18(5), 138–140. https://doi.org/10.1111/j.1740-8261.1977.tb01339.x

[111] Berger A. (2002). Magnetic resonance imaging. *BMJ (Clinical research ed.)*, 324(7328), 35. https://doi.org/10.1136/bmj.324.7328.35

[112] Al Shihabi, A., Davarifar, A., Nguyen, H. T., Tavanaie, N., Nelson, S. D., Yanagawa, J., Federman, N., Bernthal, N., Hornicek, F., & Soragni, A. (2022). Personalized chordoma organoids for Drug Discovery Studies. *Science Advances*, 8(7). https://doi.org/10.1126/sciadv.abl3674

[113] Li, J., Wu, C., Chu, P. K., & Gelinsky, M. (2020). 3D printing of hydrogels: rational design strategies and emerging biomedical applications. *Materials Science and Engineering: R: Reports*, 140, 100543. https://doi.org/https://doi.org/10.1016/j.mser.2020.100543

[114]Wikipedia contributors. (2022, January 23). *Supine position*. Wikipedia. https://en.wikipedia.org/wiki/Supine_position

[115] Raut, M., & Maheshwari, A. (2015). Imaging coronary sinus in modified bicaval view. *Annals of Cardiac Anaesthesia*, 18(3), 430. https://doi.org/10.4103/0971-9784.159821

[116] Whitaker, J., Rajani, R., Chubb, H., Gabrawi, M., Varela, M., Wright, M., Niederer, S., & O'Neill, M. D. (2016). The role of myocardial wall thickness in atrial arrhythmogenesis. *Europace : European pacing, arrhythmias, and cardiac electrophysiology : journal of the working groups on cardiac pacing,*

arrhythmias, and cardiac cellular electrophysiology of the European Society of Cardiology, 18(12), 1758–1772. https://doi.org/10.1093/europace/euw014

[117] Liu, X., Shi, H., Zheng, J., Li, K., Zhao, X., Dang, S., Wu, Y., Cheng, Y., Li, X., Yu, Z., & Wang, R. (2018). The impact of left atrial size in catheter ablation of atrial fibrillation using remote magnetic navigation. *Cardiology Research and Practice*, 2018, 3096261. https://doi.org/10.1155/2018/3096261

[118] Qian Z, Wang K, Liu S, et al. (2017). Quantitative prediction of paravalvular leak in transcatheter aortic valve replacement based on tissue-mimicking 3D printing. JACC *Cardiovasc Imaging* ;10(7):719-731. https://doi.org/10.1016/j.j*cm*g.2017.04.005

[119] Yancheng Wang, Bruce l. Tai, Hongwei Yu, et al. (2014). Silicone-based tissue-mimicking phantom for needle insertion simulation, *Transaction of the ASME*, 8: 021001-1–021001-7. https://doi.org/10.1115/1.4026508

[120] Bompotis G. (2019). Transcatheter aortic valve implantation using 3d printing modelling assistance. a single-center experience, *Hellenic Journal of Cardiology*, https://doi.org/10.1016/j.hjc.2019.01.012

[121] Mohamad Alkhouli. (2017). 3D printed models for TAVR planning, *JACC: Cardiovascular Imaging*, vol 10(7): 732-734. https://doi.org/10.1016/j.jcmg.2017.05.002

[122] Urbina, J., Sotelo, J., Montalva, C., Tejos, C., & Uribe, S. (2015). Systolic pressure gradients derived from 4D flow in a physiological healthy and aortic coarctation phantom versus cardiac catheterisation. *Proc. Intl. Soc. Mag. Reson. Med*. 23.

[123] Carabello, B. A., Paulus, W. J., Blase, P., & Carabello, A. (2009). Aortic stenosis. *The Lancet*, 373, 956–966. https://doi.org/10.1016/S0140

[124] Daebritz, S. H., Sachweh, J. S., Hermanns, B., Fausten, B., Franke, A., Groetzner, J., Klosterhalfen, B., & Messmer, B. J. (2003). Introduction of a flexible polymeric heart valve prosthesis with special design for mitral position. *Circulation*, 108(10 SUPPL.). https://doi.org/10.1161/01.cir.0000087655.41288.dc

[125] Bech-Hanssen, O., Gjertsson, P., Houltz, E., Wranne, B., Ask, P., Loyd, D., & Caidahl, K. (2003). Net pressure gradients in aortic prosthetic valves can be estimated by Doppler. *Journal of the American Society of Echocardiography : official publication of the American Society of Echocardiography*, 16(8), 858–866. https://doi.org/10.1067/S0894-7317(03)00422-X

[126] Padsalgikar, D. (2017). Applications of plastics in cardiovascular devices. *Plastics in Medical Devices for Cardiovascular Applications*,133–176.https://doi.org/10.1016/b978-0-323-35885-9.00006

[127] Vahanian, A., & Otto, C. M. (2010). Risk stratification of patients with aortic stenosis. *European Heart Journal*, 31(4), 416–423. https://doi.org/10.1093/eurheartj/ehp575

[128] Nayak, A. K., Ahmad, S. A., Beg, S., Ara, T. J., & Hasnain, M. S. (2018). Drug delivery. *Applications of Nanocomposite Materials in Drug Delivery*, 255–282. https://doi.org/10.1016/b978-0-12-813741-3.00012-1

APPENDIX:

List of Publications During PhD Study:

Journal Paper:

Wang S, Saija C, Choo J, Ou Z, Birsoan M, Germanos S, Rothwell J, Vakili B, Kotadia I, Xu Z, Rolet A, Namour A, Yang WS, Williams SE, Rhode K. (2022, June). Cardiac radiofrequency ablation simulation using a 3D-printed bi-atrial thermochromic model. *Applied Sciences*. https://doi.org/10.3390/app12136553

Wang, S., Noh, Y., Brown, J., Roujol, S., Li, Y., Wang, S., Housden, R., Ester, M. C., Al-Hamadani, M., Rajani, R., & Rhode, K. (2020, December). Development and testing of an ultrasound-compatible cardiac phantom for interventional procedure simulation using direct three-dimensional printing. *3D Printing and Additive Manufacturing*, 269–278. https://doi.org/10.1089/3dp.2019.0097

Conference Proceeding:

Wang, S., Gill, H., Wan, W., Tricker, H., Fernandes, J. F., Noh, Y., ... & Rhode, K. (2019, October). Manufacturing of ultrasound-and MRI-compatible aortic valves using 3d printing for analysis and simulation. *In International Workshop on Statistical Atlases and Computational Models of the Heart* (pp. 12-21). Springer, Cham. https://doi.org/10.1007/978-3-030-39074-7_2

Conference Abstracts:

Carlo Saija*, Shu Wang*, Behrad Vakili*, Joshua Rothwell, Woo S. Yang, Adriana Namour, Maria Birsoan, Sarah Germanos, Zhanchong Ou, Irum Kotadia, Steven E

Williams, Kawal Rhode, “A high-fidelity physical simulator for cardiac ablation procedures based on 3D printing and thermochromic pigments”, MIC Industry Event, 2021

Shu Wang*, Harminder Gill*, Yohan Noh, Nio Amanda, Joao Filipe Fernandes, Ronak Rajani, Pablo Lamata, and Kawal Rhode, “Anthropomorphic cardiac valve fabrication based on two-part water soluble PVA mould”, The 14th International Symposium on Biomechanics in Vascular Biology and Cardiovascular Disease, (Travel Award Winner), 2019

Shu Wang, Yohan Noh, Sebastian Roujol, Jemma Brown, Ye Li, Shuangyi Wang, James Housden, Mar Casajuana Ester, Ronak Rajani, Antonia Pontiki, Yimin Luo, Kawal Rhode, “Development and testing of ultrasound cardiac phantom for interventional procedure simulation using direct 3D printing”, School of Biomedical Engineering & Imaging Sciences Symposium, Kings College London, (Poster Presentation), 2018

Shu Wang, “Development and testing of a multi-modality cardiac phantom”, Breakthroughs in Healthcare Technologies Conference (Oral Presentation), 2018

Shu Wang, “A direct ultrasound phantom fabrication for catheter intervention simulation”, Medical Imaging Summer School-Italy (Poster Presentation), 2018

Co-authored Publications:

Gill, H., Fernandes, J. F., Nio, A., Dockerill, C., Shah, N., Ahmed, N., Raymond, J., Wang, S., Sotelo, J., Urbina, J., Uribe, S., Rajani, R., Rhode, K., & Lamata, P. (2023). Aortic Stenosis: Haemodynamic Benchmark and Metric Reliability Study. *Journal of Cardiovascular Translational Research*. https://doi.org/10.1007/s12265-022-10350-w

Gill, H., Fernandes, J. F., Bissell, M., Wang, S., & Lamata, P. (2020). 3D printed valve models replicate in vivo bicuspid aortic valve peak pressure drops. *Journal of the American College of Cardiology*, 75(11), 1636.